STRUCTURAL PHASE TRANSITIONS AND ELECTRONIC PROPERTIES OF Li_2O_2 and Na_2O_2

UNDER HIGH PRESSURE FOR CO_2 CAPTURE APPLICATION

Mr. Pornmongkol Jimlim

จุฬาลงกรณ์มหาวิทยาลัย
CHULALONGKORN UNIVERSITY

A Dissertation Submitted in Partial Fulfillment of the Requirements

for the Degree of Doctor of Philosophy in Physics

Department of Physics

Faculty of Science

Chulalongkorn University

Academic Year 2019

การเปลี่ยนวัฏภาคเชิงโครงสร้างและสมบัติเชิงอิเล็กทรอนิกส์ของลิเทียมเปอร์ออกไซด์และโซเดียม
เปอร์ออกไซด์ภายใต้ภาวะความดันสูงเพื่อการประยุกต์ดักจับคาร์บอนไดออกไซด์

นายพรมงคล จิ้มลิ้ม

วิทยานิพนธ์นี้เป็นส่วนหนึ่งของการศึกษาตามหลักสูตรปริญญาวิทยาศาสตรดุษฎีบัณฑิต
สาขาวิชาฟิสิกส์ ภาควิชาฟิสิกส์
คณะวิทยาศาสตร์ จุฬาลงกรณ์มหาวิทยาลัย
ปีการศึกษา 2562

Thesis Title	STRUCTURAL PHASE TRANSITIONS AND ELECTRONIC PROPERTIES OF Li_2O_2 and Na_2O_2 UNDER HIGH PRESSURE FOR CO_2 CAPTURE APPLICATION
By	Mr. Pornmongkol Jimlim
Field of Study	Physics
Thesis Advisor	Associate Professor Thiti Bovornratanaraks, Ph.D.

Accepted by the Faculty of Science, Chulalongkorn University in Partial Fulfillment of the Requirement for the Doctor of Philosophy

.... Dean of the Faculty of Science

(Professor POLKIT SANGVANICH, Ph.D.)

DISSERTATION COMMITTEE

.... Chairman

(Associate Professor Somchai Kiatgamolchai, Ph.D.)

.... Thesis Advisor

(Associate Professor Thiti Bovornratanaraks, Ph.D.)

.... Examiner

(Assistant Professor Patcha Chatraphorn, Ph.D.)

.... Examiner

(NORAVEE KANCHANAVATEE, Ph.D.)

.... External Examiner

(Assistant Professor Anusit Thongnum, Ph.D.)

พรมงคล จิ้มลิ้ม : การเปลี่ยนวัฏภาคเชิงโครงสร้างและสมบัติเชิงอิเล็กทรอนิกส์ของลิเทียม
เปอร์ออกไซด์และโซเดียมเปอร์ออกไซด์ภายใต้ภาวะความดันสูงเพื่อการประยุกต์ดักจับ
คาร์บอนไดออกไซด์. (STRUCTURAL PHASE TRANSITIONS AND ELECTRONIC
PROPERTIES OF Li_2O_2 and Na_2O_2 UNDER HIGH PRESSURE FOR CO_2 CAPTURE
APPLICATION) อ.ที่ปรึกษาหลัก : รศ. ดร.ธิติ บวรรัตนารักษ์

เนื่องจากความดันชักนำสมบัติทางเคมีและทางกายภาพที่แปลกใหม่ของวัสดุต่าง ๆ ดังนั้นการศึกษา
ผลของความดันสูงต่อการเปลี่ยนวัฏภาคเชิงโครงสร้างและสมบัติที่เกี่ยวข้องจึงสำคัญยิ่ง งานวิจัยนี้มุ่งศึกษาการ
เปลี่ยนวัฏภาคเชิงโครงสร้างและสมบัติเชิงอิเล็กทรอนิกส์ของลิเทียมเปอร์ออกไซด์และโซเดียมเปอร์ออกไซด์
ภายใต้ภาวะความดันสูงโดยใช้การคำนวณเชิงทฤษฎีฟังก์ชันนอลความหนาแน่น ผลการศึกษาเชิงโครงสร้างของ
ลิเทียมเปอร์ออกไซด์ภายใต้ภาวะความดันสูงถึง 500 GPa ทำนายว่า ที่ความดัน 75 GPa โครงสร้างซึ่งมีสมมาตร
$P6_3/mmc$ เปลี่ยนวัฏภาคเชิงโครงสร้างไปยังโครงสร้างซึ่งมีสมมาตร $P2_1$ และที่ความดัน 136 GPa โครงสร้างซึ่ง
มีสมมาตร $P2_1$ เปลี่ยนวัฏภาคเชิงโครงสร้างไปยังโครงสร้างซึ่งมีสมมาตร $P2_1/c$ เมื่อเพิ่มความดันส่งผลให้ช่องว่าง
แถบพลังงานของโครงสร้างเหล่านี้เพิ่มขึ้น แต่ที่ความดัน 11 GPa และ 40 GPa ช่องว่างแถบพลังงานลดลงใน
ขณะที่ความยาวพันธะของ O-O และค่า electron localization function (ELF) เพิ่มขึ้น ส่งผลให้ความถี่การ
สั่นแบบยืดของ O-O ลดลง สำหรับผลการศึกษาเชิงโครงสร้างของโซเดียมเปอร์ออกไซด์ภายใต้ภาวะความดันสูง
ถึง 300 GPa และอุณหภูมิสูงถึง 600 K ด้วยการประมาณแบบเสมือนฮาร์มอนิก ได้ทำนาย 2 เฟสใหม่ซึ่งมี
เสถียรภาพที่อุณหภูมิต่ำ ได้แก่ โครงสร้างซึ่งมีสมมาตร $Amm2$ ในช่วงความดัน 0 ถึง 22 GPa และโครงสร้างซึ่งมี
สมมาตร $P2_1/c$ ในช่วงความดัน 22 GPa ถึง 28 GPa เมื่อเพิ่มอุณหภูมิส่งผลให้โครงสร้างซึ่งมีสมมาตร P-$62m$
มีเสถียรภาพมากกว่าโครงสร้างซึ่งมีสมมาตร $Amm2$ และโครงสร้างซึ่งมีสมมาตร $Pbam$ มีเสถียรภาพมากกว่า
โครงสร้างซึ่งมีสมมาตร $P2_1/c$ แต่ในช่วงความดัน 2 GPa ถึง 3 GPa และ 9 GPa ถึง 10 GPa ความถี่โฟนอนบาง
โหมดลดลง และ elastic stiffness บางค่าลดลง ส่งผลให้พลังงานโฟนอนลดลง และค่า ELF เพิ่มขึ้น ช่องว่าง
แถบพลังงานของโครงสร้างเหล่านี้เพิ่มขึ้นตามความดัน ผลการวัดรามานสเปกตรัมและผลการคำนวณเชิงรามา
นของโซเดียมเปอร์ออกไซด์ภายใต้ภาวะความดันสูง แสดงหลักฐานการมีอยู่ของโครงสร้างที่ไม่สามารถระบุได้
ในช่วงความดัน 8.6 GPa ถึง 21.5 GPa และโครงสร้างซึ่งมีสมมาตร $Pbam$ ที่ความดัน 24.8 GPa ผลการ
คำนวณการเปลี่ยนแปลงพลังงานเสรีกิบส์ในปฏิกิริยาการจับคาร์บอนไดออกไซด์ด้วยลิเทียมเปอร์ออกไซด์และ
โซเดียมเปอร์ออกไซด์ทำนายว่า ปฏิกิริยาดังกล่าวสามารถเกิดขึ้นได้เองภายใต้ภาวะความดันสูงและอุณหภูมิที่
ศึกษา

สาขาวิชา	ฟิสิกส์	ลายมือชื่อนิสิต ....
ปีการศึกษา	2562	ลายมือชื่อ อ.ที่ปรึกษาหลัก ....

5872869023 : MAJOR PHYSICS

Pornmongkol Jimlim : STRUCTURAL PHASE TRANSITIONS AND ELECTRONIC PROPERTIES OF Li_2O_2 and Na_2O_2 UNDER HIGH PRESSURE FOR CO_2 CAPTURE APPLICATION. Advisor: Assoc. Prof. Thiti Bovornratanaraks, Ph.D.

Since pressure induces exotic chemical and physical properties of materials, investigation of the high-pressure effect on structural phase transition and the related properties is paramount. Structural phase transitions and electronic properties of Li_2O_2 and Na_2O_2 under high pressure were investigated using first-principles calculations based on the density functional theory. Structural phase transitions of Li_2O_2 up to 500 GPa were predicted at ~75 GPa from the $P6_3/mmc$ to the $P2_1$ structures and at ~136 GPa from the $P2_1$ to the $P2_1/c$ structures. The calculated band gaps of all phases increase with elevated pressure. At 11 and 40 GPa, the band gaps decrease, while the O-O bond lengths and the electron localization function (ELF) values increase, resulting in the O-O stretching mode softening. Structural phase transitions of Na_2O_2 up to 300 GPa were investigated with elevated temperature up to 600 K based on the quasi-harmonic approximation. Two new phases were predicted consisting of the $Amm2$ and the $P2_1/c$ structures, which are stable at low temperatures in the 0-22 and 22-28 GPa pressure ranges, respectively. At the elevated temperature, the $P\text{-}62m$ and the $Pbam$ structures more favor temperature than the $Amm2$ and the $P2_1/c$ structures, respectively. In the 2-3 and 9-10 GPa pressure ranges, some phonon modes softening and some elastic stiffnesses decreasing result in the phonon free energies decreasing and the ELF values increasing. Their band gaps also increase with increasing pressure. High-pressure Raman measurements and Raman calculations for Na_2O_2 provide the evidence for the presence of an unidentified structure at 8.6-21.5 GPa and the $Pbam$ structure at 24.8 GPa. The calculated Gibbs free energy changes of the CO_2 capture reactions by Li_2O_2 and Na_2O_2 suggest that the reactions are spontaneous under high pressure and temperature studied.

Field of Study: Physics   Student's Signature ....

Academic Year: 2019   Advisor's Signature ....

ACKNOWLEDGEMENTS

TABLE OF CONTENTS

LIST OF TABLES

LIST OF FIGURES

Chapter 1
Introduction

Pressure can induce structural phase transitions of materials and compounds, leading to changes in their physical and chemical properties. Many properties such as electronic, vibrational, elastic, and optical properties can be determined if their crystal structures are known. Therefore, the determination of crystal structure for materials and compounds is paramount, which obtains from X-ray diffraction measurements and structure searching techniques. Interestingly, many previous studies on structural phase transitions of elements and compounds under high pressure have discovered the exotic properties. For example, the simple metal sodium was found that it becomes insulating at ~200 GPa [1], while hydrogen was found that it becomes metallic at 495 GPa [2]. $NaCl_3$ was synthesized at 55-60 GPa using a laser-heated diamond anvil cell [3]. Moreover, the high-pressure study is also important for earth and planetary science because it leads to an understanding of matter in the interiors of planets that has very high pressure. Thus, investigation of structural phase transition at high pressures is of great interest, and it plays a key role in discovering exotic physical and chemical properties of materials.

Lithium peroxide (Li_2O_2) and sodium peroxide (Na_2O_2) are metal peroxide compounds that have broad applications such as bleaching agents, oxidizing agents, and breathing apparatus. They are also utilized as oxygen sources at ambient conditions by capturing carbon dioxide (CO_2) to produce oxygen (O_2) and carbonates as the following reactions [4, 5],

$$Li_2O_2 \ + \ CO_2 \ \longrightarrow \ Li_2CO_3 \ + \ (1/2) \, O_2 \, , \qquad\qquad (1.1)$$

$$Na_2O_2 \ + \ CO_2 \ \longrightarrow \ Na_2CO_3 \ + \ (1/2) \, O_2 \, . \qquad\qquad (1.2)$$
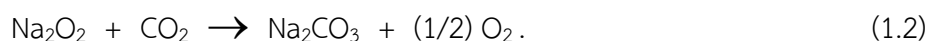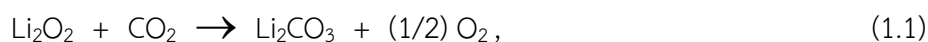
The CO_2 capture reaction by Li_2O_2 slowly occurred at ambient conditions, yet the reaction rapidly occurred at elevated temperatures above 200 °C [6, 7]. Unlike the CO_2 capture reaction by Li_2O_2, the CO_2 capture reaction by Na_2O_2 rapidly occurred at ambient conditions [8]. This implies that the activation energy for the CO_2 capture

reaction by Li_2O_2 is higher than that of Na_2O_2. Evidently, pressure can be used to overcome reaction energy barriers [9], and the Gibbs free energy change of reaction can predict spontaneity of the reaction. The Gibbs free energy increases with increasing pressure, but it decreases with increasing temperature. Thus, the CO_2 capture reaction by Li_2O_2 may occur at high pressure and at an appropriate temperature. Since pressure can induce the structural phase transitions of compounds in both reactions, pressure may affect the thermodynamic stabilities of both CO_2 capture reactions, which has not yet been studied. Consequently, the investigation of the structural phase transitions of Li_2O_2 and Na_2O_2 at high pressures provides fundamental information, which may be useful for their CO_2 capture applications.

Furthermore, Li_2O_2 and Na_2O_2 are the main discharge products that form at the cathode of the Li-O_2 and Na-O_2 batteries, respectively. The formation of Li_2O_2 and Na_2O_2 on its cathode lead to poor reversibility and high overpotential during recharge, which results in decreasing of the lifetime and cyclability [10]. The previous studies suggested that the understanding of the crystal structure and thermodynamic stability for Li_2O_2 and Na_2O_2 are important for investigating the origin of high overpotentials [11, 12]. Thus, the crystal structure and thermodynamic stability obtained from the investigations of high-pressure structural phase transitions of Li_2O_2 and Na_2O_2 may be useful for improving the related properties, the CO_2 capture, and the performance of the Li-O_2 and Na-O_2 batteries.

Regarding the crystal structure of Li_2O_2 at ambient conditions, Féher *et al.* [13] and Föppl [8] originally proposed the hexagonal structures of Li_2O_2 with the *P*-6 space group, yet their lattice parameters and atomic positions were significantly different. Later, Cota *et al.* [14] have optimized those structures to find the most stable structure using the density functional theory calculations. They reported that the fully optimized structure closely corresponds to the Föppl structure with a different space group of *P*6₃/*mmc*, and it has the lattice constants: a = 3.1830 Å and c = 7.7258 Å. Furthermore, Chan *et al.* [15] have also characterized those structures using a combination of the X-ray diffraction and first-principles techniques. They proposed that the appropriate structure of L_2O_2 should be the *P*6₃/*mmc* structure, which corresponds to the Föppl structure. In term of previous high-pressure studies, Deng *et al.* [16] predicted the

crystal structures of Li_2O_2 in the 0-100 GPa pressure range using the particle swarm optimization algorithm (CALYPSO) and the Perdew-Burke-Ernzerhof (PBE) functional that implemented in the Vienna Ab initio simulation package (VASP) to find the most stable crystal structures of Li_2O_2 at high pressures and to calculate their electronic properties. They predicted that the $P6_3/mmc$ structure transforms to a monoclinic structure with the $P2_1/c$ space group at a pressure around 84 GPa, and the calculated band gap of both phases ($P6_3/mmc$ and $P2_1/c$) increase with elevated pressure. Furthermore, Dunuwille et al. [17] experimentally investigated the structures of Li_2O_2 under high pressure up to 63 GPa using Raman spectroscopy and synchrotron X-ray diffraction. They reported that there is no structural phase transition in the pressure range studied. However, they found that the 'z' atomic position of the oxygen (1/3, 2/3, z) has an unusual change at around 35 GPa, which was supposed as the isostructural phase transition. This probably suggests the local lattice distortion in the $P6_3/mmc$ structure. In addition, Yang et al. [12] also employed synchrotron X-ray diffraction measurements to characterize the structure of Li_2O_2 at high pressures. They summarized that the $P6_3/mmc$ structure is stable up to 57 GPa. Although the high-pressure structural phase transition of Li_2O_2 has been determined, some interesting issues require more investigation such as pressure-induced local lattice distortion on the chemical bonding and electronic properties. Furthermore, the phase transformation pathway of Li_2O_2 at high pressures over 100 GPa is not determined. Therefore, these should be investigated extensively.

With regard to the previous studies for Na_2O_2, Tallman et al. [18] and Föppl [8] independently determined the crystal structure of Na_2O_2 at ambient conditions using single-crystal/powder X-ray diffraction measurements. They proposed that the Na_2O_2 structure is hexagonal with the $P-62m$ space group. The lattice constants of Tallman's structure are of a = 6.22 Å and c = 4.47 Å, while that of Föppl's structure are of a = 6.208 Å and c = 4.469 Å. However, their atomic positions of Na1 and Na2 are significantly different with atomic displacements of 0.118 Å and 0.012 Å although their lattice constants are not different within the maximal error of ± 0.01 Å. As a result, the favored structure at room temperature would be identified theoretically. Furthermore, Dunst et al. [19] analyzed the X-ray powder diffraction patterns of the microcrystalline

and nanocrystalline Na_2O_2 at ambient conditions using the Rietveld refinement methods. They found that the structures correspond to the Foppl's structure. Moreover, Tallman et al. [20] observed the X-ray powder diffraction patterns of Na_2O_2 in the 25-550°C temperature range using a Geiger-counter diffractometer. They found evidence for Na_2O_2-II and Na_2O_2-Q phases, but the crystal structure of both phases have not been indexed. The Na_2O_2-II was found at 512°C, whereas the Na_2O_2-Q was found at room temperature by quenching liquid Na_2O_2 into liquid air. They also proposed that the quenched Na_2O_2 might be stable in the temperature ranging from 596°C to 675°C or as a metastable phase at low temperature. Thus, determinations of the crystal structures for both phases of Na_2O_2 are very interesting, which will be performed with ab-initio random structure searching.

As for the previous high-pressure investigations of structural phase transition for Na_2O_2 at room temperature, Dunuwille [21] employed the Raman measurements in order to observe the phase transitions of Na_2O_2 at high pressures up to ~53 GPa. It was proposed that the transition pressure is ~14 GPa, and the chemical decomposition occurs above 26 GPa. However, the observed Raman spectra appeared the characteristic frequencies of some contaminants such as Na_2CO_3, $Na_2O_2 \cdot 2H_2O$, and NaO_2. Furthermore, the findings are not consistent with the theoretical prediction proposed by Deng et al. [16]. It was predicted that the P-62m structure transforms into an orthorhombic structure with the Pbam space group at around 28 GPa, and the Pbam structure is stable up to 100 GPa. These indicate that the previous studies on high-pressure structural phase transition of Na_2O_2 are not clarified, so more experimental and theoretical investigations need to be conducted.

Consequently, the major objective of this thesis was to investigate structural phase transitions and electronic properties of Li_2O_2 and Na_2O_2 under high pressure up to 500 GPa for Li_2O_2 and 300 GPa for Na_2O_2 using first-principles calculations. The Universal Structure Predictor: Evolutionary Xtallography (USPEX) and ab initio random structure searching (AIRSS) methods were employed to search the crystal structures at high pressures for Li_2O_2 and Na_2O_2, respectively. Raman spectroscopy was also used to determine the structural phase transition of Na_2O_2. Furthermore, the elastic and vibrational properties of Na_2O_2 were also calculated. The dynamical and

thermodynamic stabilities for the predicted phases of Li_2O_2 were verified at high pressures and 0 K, while the stabilities of the Na_2O_2 phases were verified at high pressures and in the temperature range of 0-600 K using the quasi-harmonic approximation (QHA). The minor purpose was to investigate the Gibbs free energy change in the CO_2 capture reactions of Li_2O_2 and Na_2O_2 at high pressures and temperatures using QHA. Remarkably, the findings revealed the prediction of a new high-pressure phase of Li_2O_2 and the candidates of low-temperature phases for the Na_2O_2-II and the Na_2O_2-Q, which are useful for experimental verifications. Moreover, they also provided an intensive understanding of peroxide group behaviors in Li_2O_2 and Na_2O_2 at high pressures. In addition, this study provided the thermodynamic quantities for the CO_2 capture reactions of Li_2O_2 and Na_2O_2 at high pressures and temperatures, which may be useful for CO_2 capture applications.

After this introductory chapter, the theoretical background in the dissertation will be described in Chapter 2, and then the computational and experimental methods, the results and discussions, and conclusions will be presented in Chapter 3, Chapter 4, and Chapter 5, respectively. Finally, the Phonon dispersion curves and their phonon density of states of the crystal structures used in the calculation of the Gibbs free energy change in the CO_2 capture reactions by Li_2O_2 and Na_2O_2, the Raman spectrum of Na_2O_2 at ambient conditions, and the pictures of the experimental apparatus will be shown in the Appendix.

Chapter 2

Theoretical Background

Regarding this chapter, the first-principles calculations based on density functional theory and the principles of Raman scattering that were employed in the present dissertation will be described in detail.

2.1 Density functional theory

Density functional theory (DFT) is one of the most successful approaches for calculating the ground-state total energy and electronic structure of matter. DFT employs an astute way to solve the Schrödinger equation for a many-body system. The formulation for the real system described by an effective one-body system is given by Kohn, Hohenberg, and Sham. The complex many-body wavefunction of the Schrödinger equation is reformulated in terms of the density that only depends on the three spatial coordinates. As a result, the ground-state total energy is just a function of density, the so-called density functional [22]. However, to achieve that goal, it needs principles and some approximations, which will be discussed in detail as follows.

2.1.1 Schrödinger equation for a many-body system

Based on non-relativistic quantum mechanics, the time-independent Schrödinger equation (in atomic units) for a system that consists of m nuclei and n electrons can be written as the following equation:

$$\hat{H}\,\Psi(\vec{r}_1, \vec{r}_2, \ldots, \vec{r}_n, \vec{R}_1, \vec{R}_2, \ldots, \vec{R}_m) = E\,\Psi(\vec{r}_1, \vec{r}_2, \ldots, \vec{r}_n, \vec{R}_1, \vec{R}_2, \ldots, \vec{R}_m)\,, \tag{2.1}$$

$$\hat{H} = -\frac{1}{2}\sum_{i=1}^{n}\nabla_i^2 - \frac{1}{2}\sum_{I=1}^{m}\frac{1}{M_I}\nabla_I^2 - \sum_{i,I}\frac{Z_I}{\left|\vec{r}_i - \vec{R}_I\right|} + \frac{1}{2}\sum_{i \neq j}\frac{1}{\left|\vec{r}_i - \vec{r}_j\right|} + \frac{1}{2}\sum_{I \neq J}\frac{Z_I Z_J}{\left|\vec{R}_I - \vec{R}_J\right|}\,, \tag{2.2}$$

where $\hat{H}$ is the Hamiltonian of the system. On the right-hand side of Eq. (2.2), the first two terms represent the kinetic energies of the electrons and the nuclei. The other three terms stand for Coulomb interactions due to nucleus-electron, electron-electron, and nucleus-nucleus, respectively. The position vector of $\vec{r}_i$ and $\vec{R}_I$ are of the electron at the site i and the nucleus at the site I. M_I and Z_I denote the mass of the nucleus and the charge at the site I, respectively [23].

2.1.2 Born-Oppenheimer approximation

Because the mass of the nuclei moves much slower than the electrons, the kinetic energy of nuclei is approximately zero, and the potential energy due to the nucleus-nucleus interaction becomes constant. Thus, the kinetic and potential of the nuclei can be considered separately. The Schrödinger equation for the electrons can be written as:

$$\hat{H}_e \Psi_e(\vec{r}, \vec{R}) = E_e \Psi_e(\vec{r}, \vec{R}), \tag{2.3}$$

$$\hat{H}_e = -\frac{1}{2}\sum_{i=1}^{n}\nabla_i^2 - \sum_{i,I}\frac{Z_I}{\left|\vec{r}_i - \vec{R}_I\right|} + \frac{1}{2}\sum_{i\neq j}\frac{1}{\left|\vec{r}_i - \vec{r}_j\right|}, \tag{2.4}$$

where $\Psi_e(\vec{r}, \vec{R})$ and E_e are the electron wavefunction and its energy eigenvalue, respectively [23].

2.1.3 Hohenburg-Kohn theorems

Hohenburg-Kohn theorems are the core principle in DFT, which states the relationship between the ground-state energy and its electron density. There are two theorems as follows:

The first Hohenberg-Kohn theorem states that, "*the ground-state energy from Schrödinger's equation is a unique functional of the electron density, $n_0(\vec{r})$*" [23, 24]. In other words, the ground-state wave function is a unique functional of the ground-state electron density, i.e. $\Psi_0 = \Psi[n_0]$. This implies that the ground-state energy, E, is a functional of the ground-state density, which can be written as:

$$E[n_0] = \left\langle \Psi[n_0] \middle| \hat{H} \middle| \Psi[n_0] \right\rangle. \tag{2.5}$$

The second Hohenberg-Kohn theorem states that, "*the electron density that minimizes the energy of the overall functional is the true electron density corresponding to the full solutions of the Schrödinger equation*" [23, 24]. This can be expressed as:

$$\left.\frac{\delta E[n(\vec{r})]}{\delta n}\right|_{n=n_0} = 0. \tag{2.6}$$

The exact ground-state energy, E_0, that corresponds to the ground-state density, $n_0(\vec{r})$ is given by

$$E[n_0(\vec{r})] \;\leq\; E[n(\vec{r})]. \tag{2.7}$$

Therefore, if the exact energy functional is known, then the true ground-state electron density can be obtained from the energy minimization by varying the electron density, which can be used to calculate the related properties.

2.1.4 Self-consistent Kohn-Sham equation

Since the system has many electrons, solving the Schrödinger equation [Eq. (2.3)] is almost impossible. However, Kohn and Sham proposed a new form of the Schrödinger equation for a many-electron system, namely the Kohn-Sham equation, which is written in terms of an effective one-body system as follows [23, 25]:

$$\left[-\frac{1}{2}\nabla^2 + V_{eff}(\vec{r}) \right]\Psi_i^{KS}(\vec{r}) = E_i \Psi_i^{KS}(\vec{r}) = \left[T_0 + E_H + E_{ext} + E_{xc} \right]\Psi_i^{KS}(\vec{r}), \tag{2.8}$$

where the effective potential, $V_{eff}(\vec{r})$, is given by

$$V_{eff}(\vec{r}) = V_H(\vec{r}) + V_{ext}(\vec{r}) + V_{xc}(\vec{r}). \tag{2.9}$$

$V_H(\vec{r})$, $V_{ext}(\vec{r})$, and $V_{xc}(\vec{r})$ are the potentials due to the electron-electron repulsion, the nucleus-electron attraction, and the exchange-correlation functional, respectively.

Based on the Hohenberg-Kohn theorems, the total energy, E, in Eq. (2.8) can be rewritten as the function of the electron density. Thus, the energy functional is given as

$$E[n(\vec{r})] = T_0[n(\vec{r})] + \frac{1}{2}\iint \frac{n(\vec{r})\,n(\vec{r}')}{|\vec{r} - \vec{r}'|} d\vec{r}\, d\vec{r}' + \int V_{ext}(\vec{r})\, n(\vec{r})\, d\vec{r} + E_{xc}[n(\vec{r})]. \tag{2.10}$$

On the right-hand side of Eq. (2.10), the first term is non-interacting kinetic energy for all electrons in the system. The second term represents the potential energy due to the electron-electron repulsion (Hartree energy). The third term stands for the external potential energy due to the nuclear-electron attraction, and the last term is the exchange-correlation energy functional.

Here, the electron density, $n(\vec{r})$, of the system can be obtained from

$$n(\vec{r}) = \sum_{i=1}^{N}\left|\Psi_i^{KS}(\vec{r})\right|^2 = \sum_{i=1}^{N}\Psi_i^{*\,KS}(\vec{r})\Psi_i^{KS}(\vec{r}) \,. \tag{2.11}$$

Note that, the electron density is not the wavefunction of the system, whereas it is the true electron density of the system. Furthermore, $V_H(\vec{r})$ and $V_{ext}(\vec{r})$ in Eq. (2.9) can be exactly evaluated, while $V_{xc}(\vec{r})$ is unknown, which needs the appropriate approximation.

Concerning the exchange-correlation functional, there are three types of methods: (i) Local Density Approximation, (ii) Generalized Gradient Approximation, and (iii) hybrid functionals.

(i) Local Density Approximation (LDA): LDA functional is simply approximated that the exchange-correlation energy, $E_{xc}^{LDA}[n(\vec{r})]$, is uniform at any $\vec{r}$ position. This means that the electron density is a homogeneous electron gas, $\varepsilon_{xc}^{\mathrm{hom}}[n(\vec{r})]$ [26]. This approximation is given by

$$E_{xc}^{LDA}[n(\vec{r})] = \int n(\vec{r})\,\varepsilon_{xc}^{\mathrm{hom}}[n(\vec{r})]\,d\vec{r} \,. \tag{2.12}$$

$\varepsilon_{xc}^{\mathrm{hom}}[n(\vec{r})]$ can be separated into exchange and correlation contributions as follows:

$$\varepsilon_{xc}^{\mathrm{hom}}[n(\vec{r})] = \varepsilon_x[n(\vec{r})] + \varepsilon_c[n(\vec{r})] \,, \tag{2.13}$$

where ε_x is the exchange energy density, which is given by

$$\varepsilon_x[n(\vec{r})] = -C\big[n(\vec{r})\big]^{1/3} \,, \tag{2.14}$$

where C is a free constant. In the case of the correlation energy density (ε_c), it is unknown. However, the correlation energy has been simulated using numerical quantum Monte Carlo calculations to obtain essentially exact results [27].

(ii) Generalized Gradient Approximation (GGA): Unlike LDA, GGA functional is considered that the electron density is inhomogeneous. As a result, the exchange-correlation energy, $E_{xc}^{GGA}[n(\vec{r})]$, depends on both the density, $n(\vec{r})$, and the gradient of the density, $\vec{\nabla}n(\vec{r})$ as follows:

$$E_{xc}^{GGA}[n(\vec{r})] = \int n(\vec{r})\, \varepsilon_{xc}[n(\vec{r}), \vec{\nabla} n(\vec{r})]\, d\vec{r} \,. \tag{2.15}$$

Usually, GGA functional is widely used to calculate various properties because it provides better agreement with experimental data than the LDA functional. One of the most used GGA is PBE functional proposed by Perdew, Burke, and Ernzerhof [28], which was also used in this dissertation.

(iii) Hybrid functional: The hybrid functional originated from the improving calculations of the properties of matter (e.g., band gaps, bond lengths), which were poorly consistent with experimental results when described with the LDA and GGA functionals. Generally, the hybrid functionals have been constructed from the linear combination sets of the Hartree-Fock exchange functional, E_x^{HF}, and the exchange-correlation functionals, that were weighted by individual parameters [29].

$$E_x^{HF} = -\frac{1}{2} \sum_{i,j} \iint \psi_i^*(\vec{r}_1)\psi_j^*(\vec{r}_2) \frac{1}{r_{12}} \psi_j(\vec{r}_1)\psi_i(\vec{r}_2)\, d\vec{r}_1\, d\vec{r}_2 \,. \tag{2.16}$$

Previously, many hybrid functionals have been proposed such as B3LYP, PBE0, and HSE functionals. One of the most popular functionals is a screened Coulomb potential hybrid density functional, the so-called the HSE (Heyd-Scuseria-Ernzerhof) functional, which is expressed as

$$E_{xc}^{\omega PBEh} = a\, E_x^{HF,SR}(\omega) + (1-a) E_x^{PBE,SR}(\omega) + E_x^{PBE,LR}(\omega) + E_c^{PBE} \,, \tag{2.17}$$

where ω denotes an adjustable parameter which dominates the boundary of short-range interactions. The ω_{PBEh} is equivalent to PBE0 for $\omega = 0$ and approach to PBE for $\omega \rightarrow 0$. The abbreviation of 'SR' and 'LR' mean the various short- and long-range terms in Eq. (2.17). When the HSE functional is fixed the values of $a = 0.25$ and $\omega = 0.2$, is usually called HSE06 [30].

The self-consistent field (SCF) method [25] is employed to solve for the Kohn-Sham orbitals and the total energies, as shown in Figure 1. Initially, the electron density is guessed to determine the effective potential functional, and then the Kohn-Sham equation is solved to obtain the electron density. This process is subsequently performed until the densities are consistent within the convergence setting. Finally,

the converged density is used to calculate the desired properties such as the electronic band structure and density of states.
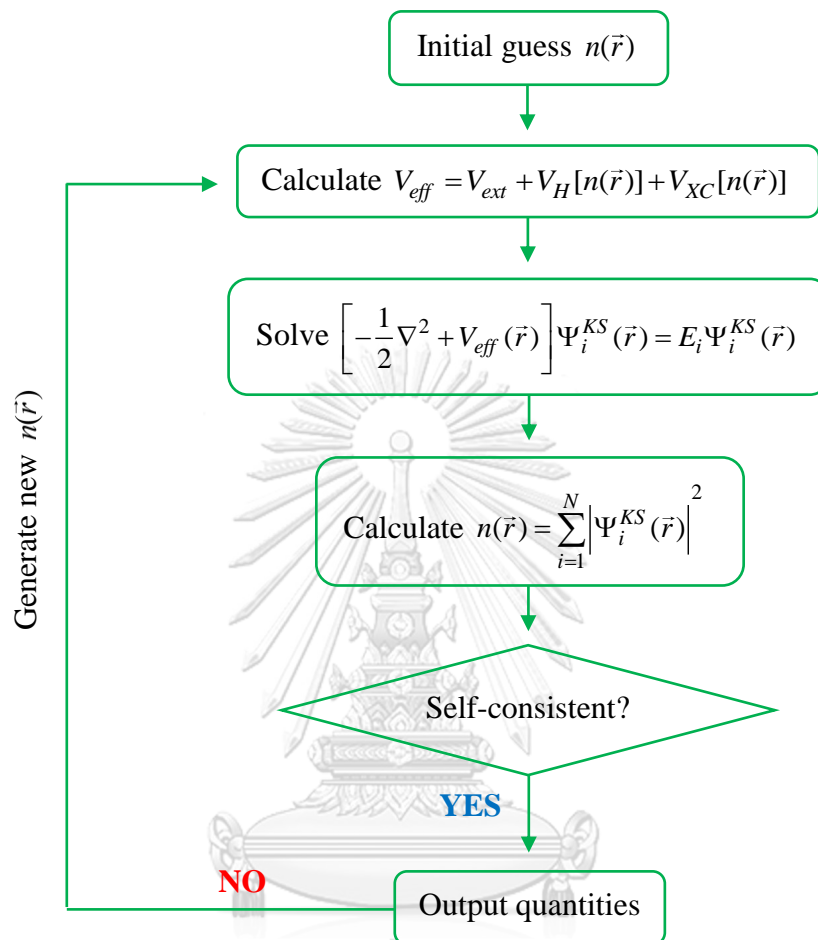
Figure 1: Schematic flowchart for the self-consistent Kohn-Sham equation method

2.1.5 The secular equation

To obtain the solution of the Kohn-Sham equation, the Kohn-Sham orbitals are expanded in terms of a linear combination of arbitrary basis function,

$$\Psi_n(\vec{r}) = \sum_{i=1}^{N} C_i^n \varphi_i(\vec{r}), \tag{2.18}$$

where C_i^n is a coefficient of the basis function, $\varphi_i(\vec{r})$, in the Kohn-Sham orbitals, $\Psi_n(\vec{r})$. In principle, N is approach to infinity; however, practically, N should be large enough for accuracy of the Kohn-Sham orbitals.

By substituting the Kohn-Sham orbitals, Eq. (2.18), into the Kohn-Sham equation, Eq. (2.8), the equation becomes

$$\sum_{i=1}^{N} C_i^n \left[-\frac{\nabla_i^2}{2} + V_{eff}(\vec{r}) \right] \varphi_i(\vec{r}) = \sum_{i=1}^{N} C_i^n E_i \varphi_i(\vec{r}). \qquad (2.19)$$

By multiplying the complex conjugate of the basis function, $\varphi_j^*(\vec{r})$, to Eq. (2.19) and taking integration over all space, the equation becomes

$$\sum_{i=1}^{N} C_i^n \int \varphi_j^*(\vec{r}) \left[-\frac{\nabla_i^2}{2} + V_{eff}(\vec{r}) \right] \varphi_i(\vec{r}) d\vec{r} = \sum_{i=1}^{N} C_i^n E_i \int \varphi_j^*(r) \varphi_i(\vec{r}) d\vec{r} \qquad (2.20)$$

Here, Eq. (2.20) can be written in the matrix form as shown below:

$$H\mathbb{C} = E\mathbb{Q}\mathbb{C}, \qquad (2.21)$$

where H, $\mathbb{Q}$, $\mathbb{C}$, and E are the Hamiltonian matrix, the overlap matrix, the eigenvector, and the eigenvalue, respectively. H and $\mathbb{Q}$ have the $N \times N$ dimensional matrices, so there are the N eigenvalues and the N eigenvectors. This equation is called as the secular equation [22].

2.1.6 Calculation techniques in DFT

2.1.6.1 Plane-wave basis set, cutoff energy, and k-point mesh

In the case of solids, the arrangement of atoms in crystal structure is periodically conditioned by the symmetry, so that solving the Kohn-Sham equation can be simplified by employing Bloch's theorem. The theorem states that the electronic wavefunctions at each k-point can be expanded in terms of a discrete plane-wave basis set [31]. This can be expressed as

$$\Psi_k^n(\vec{r}) = u_k^n(\vec{r}) e^{i\vec{k}\cdot\vec{r}}, \qquad (2.22)$$

where $u_k^n(\vec{r})$, $\vec{k}$, and n are periodic function, wavevector and band index, respectively. Here, the electron wavefunction, $\Psi_k^n(\vec{r})$, and the energy eigenvalue, E, must satisfy the two conditions as follows:

$$E(\vec{k}) = E(\vec{k}+\vec{G}), \qquad (2.23)$$

$$\Psi_k^n(\vec{r}) \quad = \quad \Psi_{k+G}^n(\vec{r}), \tag{2.24}$$

where $\vec{G}$ is called as the reciprocal lattice vector. Regarding the periodic function, $u_k^n(\vec{r})$, can be written in terms of a summation over plane wave sets as:

$$u_k^n(\vec{r}) \quad = \quad \sum_j C_j^n(\vec{k})\, e^{i\vec{G}_j \cdot \vec{r}}. \tag{2.25}$$

By substituting Eq. (2.25) into Eq. (2.22), the volumetric normalized wavefunction can be obtained from the expression:

$$\Psi_k^n(\vec{r}) \quad = \quad \frac{1}{\sqrt{V}} \sum_j C_j^n(\vec{k})\, e^{i(\vec{k}+\vec{G}_j)\cdot \vec{r}}. \tag{2.26}$$

Therefore, the exact solution of the Kohn-Sham equation can be solved using the infinite number of the plane-wave basis sets in Eq. (2.26). The problem is now transformed from the real space to the reciprocal space, $\vec{k}$-space, which represents the Fourier transform of the periodic lattice in the real space. Practically, it is, nevertheless, impossible to use the infinite number of the plane-wave basis sets because of the limited computational resources. The maximum value of the reciprocal lattice vector, $\vec{G}_{\max}$, however, is directly related to the kinetic cutoff energy, E_{cut}, via the expression:

$$E_{cut} \quad \leq \quad \frac{\hbar^2}{2m} \left| \vec{k} + \vec{G}_{\max} \right|^2. \tag{2.27}$$

Thus, this implies that the accuracy of the obtained ground-state energy can be increased using the larger kinetic cutoff energy and the $\vec{k}$-points, which needs more computational resources.

2.1.6.2 Norm-conserving and ultrasoft pseudopotentials

In a solid system, ion cores consist of nuclei and tightly bound core electrons. The wavefunctions of valence-electron and core-electron are orthogonal. The ion cores are treated as frozen in the pseudopotential approach. Thus, the ion cores are not considered in chemical bonding and consequence of structural modifications [31].

Generally, a pseudopotential form is expressed as:

$$V_{NL} \quad = \quad \sum |lm\rangle V_l \langle lm|, \qquad\qquad (2.28)$$

where $|lm\rangle$ stands for the spherical harmonics, and V_l denotes the pseudopotential for the angular momentum l.

In order to generate pseudopotentials, all-electron calculations performed for an isolated atom in a selected electronic configuration. Then, the valence-electron eigenvalues and valence-electron wavefunctions for the atom are obtained, as shown in Figure 2. Next, the parameters for the ionic pseudopotential are initialized and then adjusted, so that a pseudo atom calculation provides pseudo wavefunctions, Ψ_{PS}, and pseudo eigenvalues. The pseudo wavefunctions correspond to the valence-electron wavefunctions outside some cutoff radius, R_c, where the pseudo eigenvalues are equal to the valence-electron eigenvalues. If the pseudo and all-electron wavefunctions are normalized to one, then the constraint of norm-conservation is satisfied, resulting in the corresponding of the wavefunctions outside the R_c. The pseudopotential is called the norm-conserving pseudopotential [31].

However, since there are intrinsic limits on optimizing the convergence of norm-conserving pseudopotentials, the other pseudopotential approach has been created. One is the ultrasoft pseudopotentials proposed by Vanderbilt [32]. They allow performing calculations with the lowest possible cutoff energy, resulting in decreasing the plane-wave basis set. To reduce the basis set, the norm-conservation condition is broken by removing the charge from the core region. Therefore, the pseudo wavefunctions are softened as possible within the core, providing a considerable decreasing of the cutoff energy [31].
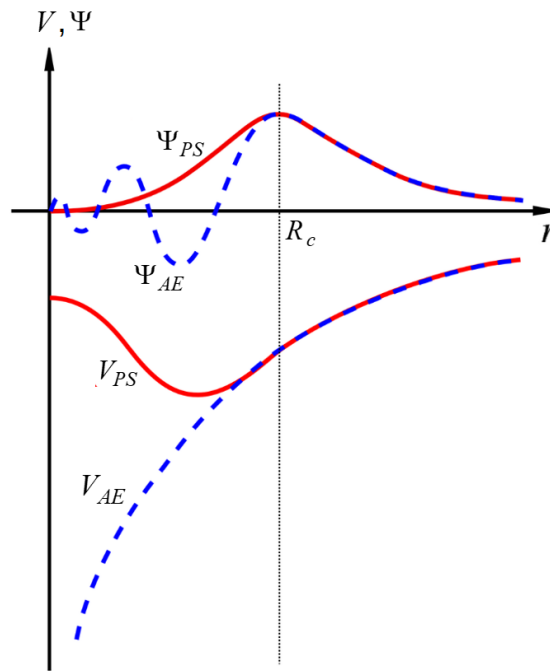
Figure 2: Comparison of the all-electron (AE) and pseudo (PS) wavefunctions (Ψ) and their potentials (V) [33].

The ultrasoft pseudopotentials form is the same as other pseudopotentials plane-wave methods with the nonlocal potential, V_{NL},

$$V_{NL} \quad = \quad \sum_{m,I} D_{nm}^{(0)} \left| \beta_n^I \right\rangle \left\langle \beta_m^I \right|, \tag{2.29}$$

where the pseudopotential is identified by the projectors, β, and coefficients, $D^{(0)}$, and it differs for different atomic species. The index, I, represents an atomic site. Thus, the electron density can be expressed as:

$$n(\vec{r}) \quad = \quad \sum_i \left[\left| \phi_i(\vec{r}) \right|^2 + \sum_{nm,I} Q_{nm}^I(\vec{r}) \left\langle \phi_i \left| \beta_n^I \right\rangle \left\langle \beta_m^I \right| \phi_i \right\rangle \right], \tag{2.30}$$

where ϕ are the wavefunctions, while $Q(\vec{r})$ are the augmentation functions localized in the core regions. Consequently, the ultrasoft potentials can be obtained from the local part, $V_{loc}^{ion}(\vec{r})$, and from the coefficients $D^{(0)}$, Q, and β [31].

2.1.7 Geometry optimization

Based on DFT, the geometry optimization is performed at given pressure and absolute zero temperature to obtain the minimum enthalpy structure. The crystal structure is relaxed until the atomic force acting on each atom is close to zero or the maximum force setting. The force vector, F, is given by

$$F = -\frac{\partial H}{\partial X}\Big|_{P}, \tag{2.31}$$

where H is the enthalpy, and X is the coordinates of atoms. The enthalpy variation about the minimum, $X_{\min}$, is defined by

$$\delta H = \frac{1}{2}(X - X_{\min}) \cdot A(X - X_{\min}), \tag{2.32}$$

where A stands for the Hessian matrix. The quasi-Newton method [34] is used to optimize lattice parameters and atomic coordinates of crystal structure at a given pressure, P, in order to find the $X_{\min}$ via the force in one-step optimization. Then, the X_i is varied to obtain the $X_{\min}$, using the equation:

$$\Delta X_i = H_i F_i = (B)^{-1} F_i. \tag{2.33}$$

Here, H_0 can be estimated and refined by the BFGS algorithm [35]. At the $X_{\min}$, the crystal structure is exactly at the pressure, P, which has the minimum enthalpy.

2.1.8 Electronic band structure and Density of states

The electronic properties of the system are obtained from the expectation values of the ground-state energy, corresponding to any wavevector, $\vec{k}$, which is expressed by

$$\left\langle \Psi_n^{\vec{k}'} \middle| \hat{H} \middle| \Psi_n^{\vec{k}} \right\rangle = E_n^{\vec{k}} \delta_{\vec{k}\vec{k}'}. \tag{2.34}$$

Here, the ground-state wavefunction, $\Psi_n^{\vec{k}}$, is the solution of the Kohn-Sham equation of the system that has the Hamiltonian, $\hat{H}$, and the energy eigenvalue, $E_n^{\vec{k}}$.

By plotting the set of the energy eigenvalues along with high symmetry directions in the Brillouin zone, the electronic band structure is obtained both the valence and conduction bands.

The density of states (DOSs) is employed to describe the state numbers occupied by the system at each energy level. The DOSs for a given band n, $N_n(E)$, is defined by

$$N_n(E) \;=\; \frac{1}{4\pi^3}\int d\vec{k}\ \delta\big(E-E_n(\vec{k})\big),$$ (2.35)

where $E_n(\vec{k})$ is the energy eigenvalue for the given band, which describes the dispersion, and the integral is calculated over the Brillouin zone of the primitive cell [31].

2.2 *Ab initio* lattice dynamics

2.2.1 Phonons

Lattice vibrations in crystals or phonons play a key role in the prediction of the dynamical stability for crystal structures, and their vibrational properties such as phonon dispersion, infrared and Raman spectra can be described using a harmonic approximation. Based on a Taylor expansion of the total energy, E, around the equilibrium coordinates, it is expressed as:

$$E \;=\; E_0 + \sum_{\kappa,\alpha}\frac{\partial E}{\partial \vec{u}_{\kappa,\alpha}}\cdot\vec{u}_{\kappa,\alpha} + \frac{1}{2}\sum_{\kappa,\alpha,\kappa',\alpha'}\vec{u}_{\kappa,\alpha}\cdot\Phi^{\kappa,\kappa'}_{\alpha,\alpha'}\cdot\vec{u}_{\kappa',\alpha'} + \dots,$$ (2.36)

where $\vec{u}_{\kappa,\alpha}$ denotes the atomic displacements vector from their equilibrium positions. All atoms are labelled by κ, and the Cartesian coordinates in x, y, and z directions are represented by $\alpha=1,2,3$, respectively. $\Phi^{\kappa,\kappa'}_{\alpha,\alpha'}$ represents the force constants matrix (or Hessian matrix), which is given by

$$\Phi^{\kappa,\kappa'}_{\alpha,\alpha'} \;=\; \frac{\partial^2 E}{\partial\vec{u}_{\kappa,\alpha}\,\partial\vec{u}_{\kappa',\alpha'}}\;.$$ (2.37)

Here, the force acting on atoms, κ, in direction, α, can be calculated using the expression:

$$F_{\kappa,\alpha} \;=\; -\frac{\partial E}{\partial\vec{u}_{\kappa,\alpha}}\;.$$ (2.38)

At the equilibrium, the forces are all zero, and the 3rd and higher-order terms of Eq. (2.36) are approximate to zero within the harmonic approximation.

By assuming the periodic boundary conditions and substituting the plane-wave,

$$\vec{u}_{\kappa,\alpha} \;=\; \varepsilon_{m\kappa,\alpha q} \exp\!\left[i(\vec{q}\cdot\vec{R}_{\kappa,\alpha} - \omega t) \right], \tag{2.39}$$

it leads to the eigenvalue equation as:

$$D_{\alpha,\alpha'}^{\kappa,\kappa'}(\vec{q})\, \varepsilon_{m\kappa,\alpha q} \;=\; \omega_{m,q}^2(\vec{q})\, \varepsilon_{m\kappa,\alpha q} \;, \tag{2.40}$$

where $\omega_{m,q}$ denote the frequencies eigenvalues for each m-mode in the directions q, while $\varepsilon_{m\kappa,\alpha q}$ stand for the mode eigenvectors, and $D_{\alpha,\alpha'}^{\kappa,\kappa'}(\vec{q})$ represents the dynamical matrix which is the Fourier transform of the force constant matrix,

$$D_{\alpha,\alpha'}^{\kappa,\kappa'}(\vec{q}) \;=\; \frac{1}{\sqrt{M_\kappa M_{\kappa'}}} \sum_a \Phi_{\alpha,\alpha'}^{\kappa,\kappa'}(a)\, e^{-i\vec{q}\cdot\vec{R}_a} \tag{2.41}$$

The dependence of the frequencies eigenvalues, $\omega_{m,q}$, on the wavevectors, $\vec{q}$, is called the phonon dispersion [36].

In the case of the phonon density of states (DOSs) is defined in the same way as the electronic density of states. The partial phonon density of states is determined as a contribution from the given atom to the total phonon DOS. The contribution to the partial density of states on atom i from each phonon band, is evaluated using:

$$N_i(E) \;=\; \frac{1}{4\pi^3} \int d\vec{k}\, \left| e_j(i) \right|^2 \delta(E - E_n(\vec{k})), \tag{2.42}$$

where e_j is the eigenvector responding to the energy mode, E_j. The partial phonon DOS is then obtained by summation of these contributions over all phonon bands [31].

2.2.2 Density functional perturbation theory

Density functional perturbation theory (DFPT) is one of the efficient methods for *ab initio* lattice dynamics calculations. Here, the dynamical matrix and phonons are obtained using the perturbing ionic positions. The force constants matrix can be calculated using differentiating the Hellmann-Feynman forces on atoms with respect to their ionic coordinates, depending on the ground-state electron density and its linear response to atomic positions due to distortion. Based on DFPT formalism similar to DFT formalism, the 2nd order energy change depends on the 1st order electron density

change. The problem of DFPT can be solved by minimizing the 2nd order perturbation of the total energy, providing the 1st order changes in density, $n(\vec{r})$, wavefunctions, $\psi_{k,n}$, and potential, V. The 2nd order electronic energy, $E^{(2)}$, is given by

$$
\begin{aligned}
E^{(2)} \;=\; & \sum_{k,n}\left[\left\langle\psi_{k,n}^{(1)}\left|H^{(0)}-\varepsilon_{k,n}^{(0)}\right|\psi_{k,n}^{(1)}\right\rangle+\left\langle\psi_{k,n}^{(1)}\left|V^{(1)}\right|\psi_{k,n}^{(0)}\right\rangle+\left\langle\psi_{k,n}^{(0)}\left|V^{(1)}\right|\psi_{k,n}^{(1)}\right\rangle\right]+ \\
& \sum_{k,n}\left\langle\psi_{k,n}^{(0)}\left|V^{(2)}\right|\psi_{k,n}^{(0)}\right\rangle+\frac{1}{2}\int\frac{\delta^2 E_{xc}}{\delta n(\vec{r})\delta n(\vec{r}')}n^{(1)}(\vec{r})n^{(1)}(\vec{r}') \quad,
\end{aligned}
\tag{2.43}
$$

where the superscripts of (0), (1), and (2) correspond to the ground state, 1st, and 2nd order changes, respectively [31].

However, DFPT implemented in the CASTEP code (version 6.1) is based on the norm-conserving pseudopotentials only. In this work, the DFPT was employed to calculate the Raman spectrum of Na$_2$O$_2$ for the *Pbam* structure at 30 GPa to compare with the measured Raman spectrum.

2.3 Elastic constants

Elastic constants are crucial for describing the elastic behaviors of crystals; especially, the elastic stability of crystal lattices. Moreover, the elastic constants are also employed to calculate the elastic properties such as bulk modulus, Young modulus, and Poisson ratios. The elastic behaviors are described by the elastic matrix (or the stiffness matrix), C_{ij}, which is defined by

$$
C_{ij} \;=\; \frac{1}{V_0}\left(\frac{\partial^2 E}{\partial \varepsilon_i\,\partial \varepsilon_j}\right),
\tag{2.44}
$$

where E and ε are the crystal energy and the strain, and V_0 denotes the volume at the equilibrium. Here, the stress is given by $\sigma_i = C_{ij}\varepsilon_j$. The indices, i and j, represent the standard Voigt notation in which a pair of Cartesian indices is contracted into a single integer $1 \le i \le 6$: xx $\rightarrow$ 1, yy $\rightarrow$ 2, zz $\rightarrow$ 3, yz $\rightarrow$ 4, xz $\rightarrow$ 5, xy $\rightarrow$ 6 [37].

Generally, the stiffness matrix has 6 × 6 sizes. However, because it is symmetric, it remains of 21 independent components. Moreover, there are symmetry constraints based on the crystal classes, this leads to a reduction of the number of independent elastic constants and difference of the independent components for each crystal class.

Based on an infinitesimal strain within a homogeneous deformation, the energy, E, is given by the following quadratic form:

$$E = E_0 + \frac{1}{2}V_0 \sum_{i,j=1}^{6} C_{ij}\, \varepsilon_i\, \varepsilon_j + O(\varepsilon^3),\qquad(2.45)$$

where E_0 is the energy at the equilibrium. As a result, a symmetric strain or stress matrix of 3 × 3 becomes a vector of length 6, while the stiffness tensor of rank four becomes the 6 × 6 matrices.

As for the elastic stability criterion, the elastic energy in Eq. (2.45) is always positive ($E > 0, \forall \varepsilon \neq 0$), which is equivalent to the following conditions: (i) The matrix C is positive, (ii) all eigenvalues of C are positive, (iii) all the leading principal minors of C are positive, and (iv) an arbitrary set of minors of C are all positive. These are called the generic Born elastic stability conditions for an unstressed crystal [37].

In this work, the elastic stability conditions at high pressures were considered for the P-$62m$ and $Amm2$ structures of Na_2O_2 to verify the differences between both structures. As the P-$62m$ and $Amm2$ structures are hexagonal and orthorhombic, respectively, the Born stability criteria for both crystal systems will be described as follows:

The stiffness matrix for a hexagonal crystal system, C_hexa, is given by

$$C_\text{hexa} = \begin{pmatrix} C_{11} & C_{12} & C_{13} & & & \\ . & C_{11} & C_{13} & & & \\ . & . & C_{33} & & & \\ & & & C_{44} & & \\ & & & & C_{44} & \\ & & & & & C_{66} \end{pmatrix}.\qquad(2.46)$$

There are five independent elastic constants, where C_{66} is equal to $(C_{11} - C_{12})/2$. By calculating the eigenvalues of the stiffness matrix, then obtains the conditions for the elastic stability in the hexagonal case as:

$$C_{11} > |C_{12}|,\quad 2C_{13}^2 < C_{33}(C_{11} + C_{12}),\quad C_{44} > 0,\quad C_{66} > 0.\qquad(2.47)$$

Regarding the stiffness matrix for an orthorhombic crystal system, C_{ortho}, it is expressed by

$$C_{ortho} = \begin{pmatrix} C_{11} & C_{12} & C_{13} & & & \\ . & C_{22} & C_{23} & & & \\ . & . & C_{33} & & & \\ & & & C_{44} & & \\ & & & & C_{55} & \\ & & & & & C_{66} \end{pmatrix}. \tag{2.48}$$

There are nine independent elastic constants. By solving the eigenvalues of the stiffness matrix, and then finds the solutions that satisfy the Born criteria. Finally, the conditions for the elastic stability in the orthorhombic case are obtained as:

$$C_{11} > 0, \quad C_{44} > 0, \quad C_{55} > 0, \quad C_{66} > 0, \quad C_{11}C_{22} > C_{12}^2,$$
$$C_{11}C_{22}C_{33} + 2C_{12}C_{13}C_{23} - C_{11}C_{23}^2 - C_{22}C_{13}^2 - C_{33}C_{12}^2 > 0. \tag{2.49}$$

Note that all conditions of elastic stability as described before for an unloading system, but it can be applied arbitrary external stress, σ, by introducing the elastic stiffness tensor, B, under loading system, which is defined (in tensorial notation) as:

$$B_{ijkl} = C_{ijkl} + \frac{1}{2}\left(\delta_{ik}\sigma_{jl} + \delta_{jk}\sigma_{il} + \delta_{il}\sigma_{jk} + \delta_{jl}\sigma_{ik} - 2\delta_{kl}\sigma_{ij}\right), \tag{2.50}$$

where δ is the Kronecker delta [37].

2.4 *Ab initio* random structure searching

Ab initio random structure searching (AIRSS) is one of the most powerful methods for searching crystal structure at high pressures. The thermodynamic relation is employed to estimate enthalpy of the crystal structure at a given pressure, P_s,

$$H(P) \simeq H(P_s) + (P - P_s)\frac{dH}{dP}\Big|_{P_s} + \frac{1}{2}(P - P_s)^2 \frac{d^2H}{dP^2}\Big|_{P_s}$$

$$= H(P_s) + (P - P_s)V_s - \frac{1}{2}(P - P_s)^2 \frac{V_s}{B_s}, \tag{2.51}$$

where $H(P_s)$ stands for the lowest enthalpy of the structure at pressure P_s with volume V_s, whereas $H(P)$ denotes the enthalpy of different structures, which may become more

stable at another pressure P. V_s and B_s are the volume and the bulk modulus. Using the simple linear approximation, Eq. (2.51) is rewritten as:

$$H(P) \quad \simeq \quad H(P_s) + (P - P_s)V_s \; . \qquad (2.52)$$

The concept of the AIRSS method is illustrated in Figure 3. By building many initial structures that implemented reasonable unit cell volumes and interatomic distances, these structures (yellow dots) are locally optimized (with no constraint) to the nearly local minimum of the potential energy surface at a considered pressure using the random atomic displacements and the random unit cell deformations, namely shaking. Then, these structures are relaxed again by imposing the possible symmetries to find the lowest energy structure at a given pressure. The geometry optimization that implemented in the AIRSS is based on the DFT calculations [38].
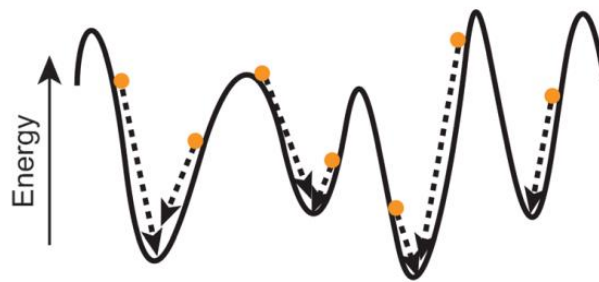
Figure 3: A schematic representation of the AIRSS method in a one-dimension of the potential energy surface. The dots refer to the generated structures, and the dashed arrows represent the local optimizations [39].

2.5 Universal Structure Predictor: Evolutionary Xtallography

Universal Structure Predictor: Evolutionary Xtallography (USPEX) is one of the most successful algorithms in structure searching at high pressures. USPEX attempts to find the global minimum enthalpy structure by using evolutionary principles such as breeding, mutation, and permutation. The evolutionary principles are shown in Figure 4. The randomly generated structures (both lattice parameter and atomic positions) are conducted after assigning the chemical composition of materials/compounds. These structures are locally optimized to the local minimum energy at a considered pressure [Figure 4(a)]. Moreover, to create different structures with respect to the

parent structures, the locally optimized structures are operated by the evolutionary operators consisting of the heredity, mutation, and permutation operators. The heredity operator uses the breeding of two-parents to generate the child structure, as shown in Figure 4(b). The mutation employs the mapping of two parent structures, and the parents' lattice vector is transformed to generate the child's lattice by applying a strain matrix. Conversely, the permutation operator uses the interchanging of the atomic positions of different types, acting on a single parent, as illustrated in Figure 4(b) [39, 40].

As for the structure optimization, USPEX is designed to perform with various *ab initio* codes for calculating the thermodynamic quantities (e.g., pressure, enthalpy) based on the DFT calculations.
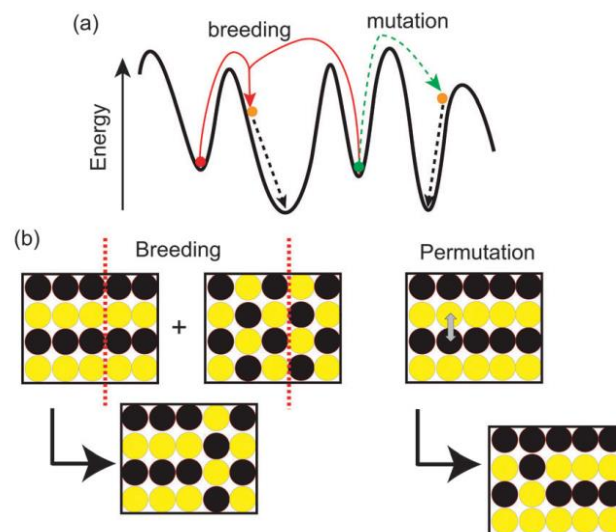
Figure 4: (a) Same as Fig. 3, but for evolutionary algorithms. (b) Schematic illustration of the heredity and the permutation operators [39].

2.6 Thermodynamic quantities within the quasi-harmonic approximation

The thermodynamic quantities of solids (e.g., Helmholtz free energy, Gibbs free energy, entropy) can be calculated using *ab initio* lattice dynamics based on the quasi-harmonic approximation (QHA). Usually, phonons are estimated to be the harmonic model by omitting the 3rd order and higher-order terms of the total energy expansion as shown in Eq. (2.53). This implies that all interatomic forces are purely harmonic. In

the perfect harmonic crystal, it is considered that there is no volume expansion with temperature. However, if the temperature of the system is far from the melting point, the Helmholtz free energy, F, can be calculated within the QHA using the expression:

$$F(V,T) = E_{tot}(V) + F_{ph}(V,T) = E_{tot}(V) + k_B T \int_0^\infty g(\omega) \ln\left[2\sinh\left(\frac{\hbar\omega}{2k_B T} \right) \right] d\omega, \qquad (2.53)$$

where $E_{tot}(V)$ stands for the ground-state total energy, and $F_{ph}(V,T)$ denotes the phonon free energy at a given volume V as a function of temperature T, which includes the zero-point vibrational energy. $\omega = \omega(V)$ represents the volume-dependent phonon frequencies, and $g(\omega)$ is the phonon density of states. $\hbar$ and k_B are the reduced Planck's and Boltzmann's constants, respectively.

Thus, the vibrational entropy, S_{ph}, can be obtained from [31]

$$S_{ph}(T) = -\left(\frac{\partial F}{\partial T} \right)_V = k_B \left\{ \int \frac{\frac{\hbar\omega}{k_B T}}{\exp\left(\frac{\hbar\omega}{k_B T} \right) - 1} g(\omega) d\omega - \int g(\omega)\left[1 - \exp\left(-\frac{\hbar\omega}{k_B T} \right) \right] d\omega \right\}. \qquad (2.54)$$

Based on the phonon free energy, $F_{ph}(V,T)$, in Eq. (2.53), the Gibbs free energy of the structure at the pressure P and the temperature T can be calculated using the thermodynamic relations as follows:

$$G(P,T) = E_{tot}(V) + F_{ph}(V,T) + P(V,T)V, \qquad (2.55)$$

$$P(V,T) = -\frac{\partial F(V,T)}{\partial V} = P(V) - \frac{\partial F_{ph}(V,T)}{\partial V}, \qquad (2.56)$$

$$\therefore\ G(P,T) = E_{tot}(V) + F_{ph}(V,T) + P(V)V - V \frac{\partial F_{ph}(V,T)}{\partial V}. \qquad (2.57)$$

Furthermore, the Gibbs free energy can be rewritten in terms of the phonon free energy and the entropy as:

$$G(P,T) = H(P) - T S(T) = E_{tot}(V) + F_{ph}(V,T) + P(V)\,V - T\,S_{ph}(T). \qquad (2.58)$$

Practically, $E_{tot}(V)$ and $P(V)V$ are obtained using the DFT calculations, while $F_{ph}(V,T)$ and $S_{ph}(T)$ are obtained using the phonon calculations.

As the Gibbs free energy depends on both pressure and temperature, the pressure dependence of the Gibbs free energy and the temperature dependence of the Gibbs free energy should be discussed. The pressure dependence of G is given by

$$\left(\frac{\partial G}{\partial P}\right)_T = V \quad \Rightarrow \quad \Delta G = G(P_2) - G(P_1) = \int_{P_1}^{P_2} V\, dP. \tag{2.59}$$

By plotting the G versus P, as shown in Figure 5(a), V represents the gradient line, which is positive. This implies that G increases with elevated pressure P at constant temperature T. Moreover, the plots show that the gradient for gas is sensitive changes with pressure, but the gradient for liquid and solid are constant approximately. In the same way, the temperature dependence of G is given by

$$\left(\frac{\partial G}{\partial T}\right)_V = -S = \frac{G - H}{T}. \tag{2.60}$$

Because S is positive, G decreases with increasing temperature at fixed pressure P, as shown in Figure 5(b). The gradient of the plot of G and T is used to determine the entropy of the system. The gradient for gas is greatest, then liquid and solid, respectively [40].
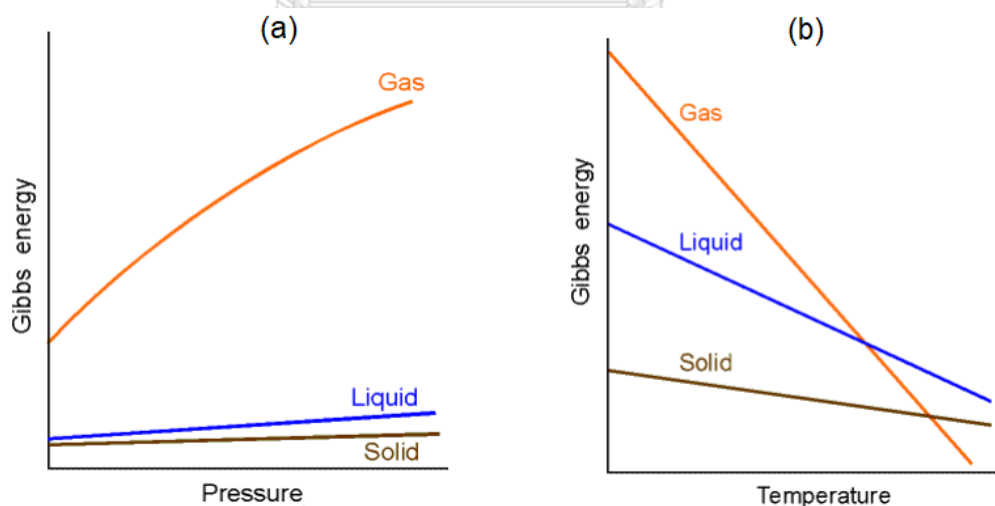
Figure 5: (a) the pressure dependence of the Gibbs free energy, (b) the temperature dependence of the Gibbs free energy [41].

Besides, the relationship between Gibbs free energy (G), enthalpy (H), and entropy (S) for solid can be graphically presented, as shown in Figure 6.
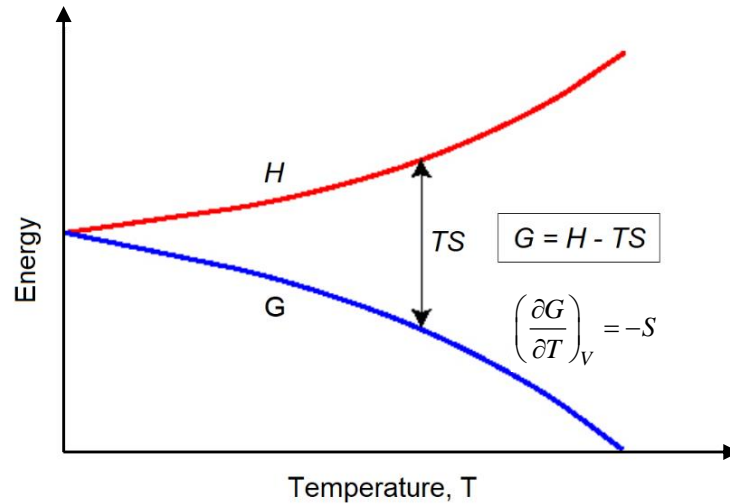
Figure 6: The relationship between Gibbs free energy (G), enthalpy (H), and entropy (S) for solid, is defined by G = H – TS [41].

Usually, the Gibbs free energy is used to verify the thermodynamic stability of the system or the phase stability at the considered pressure and temperature. The most stable structure is the lowest free energy structure. Here, the change in Gibbs free energy of the chemical reaction is also employed to predict the spontaneity and the direction of the reaction, which will be discussed below.

2.7 Gibbs free energy change of chemical reaction

In this work, the CO_2 capture reactions by Li_2O_2 and Na_2O_2 at the considered pressures and temperatures will be estimated using the change in Gibbs free energies of both reactions. Here, the Gibbs free energy of the chemical reaction will be described.

In general, the change in Gibbs free energy of the system or a chemical reaction is given by

$$\Delta G \;=\; G_{final} - G_{initial} \;=\; G_{products} - G_{reactants}, \qquad (2.61)$$

where the subscript of initial and final refer to the initial and final states of the system. If reactants and products are all solid phases, their Gibbs free energies can be calculated using Eq. (2.57) or Eq. (2.58) at the given pressure and temperature.

For example, the CO_2 capture reactions by Li_2O_2 and Na_2O_2 is given by

$$Li_2O_2 + CO_2 \rightarrow Li_2CO_3 + (1/2)O_2, \qquad (2.62)$$

$$Na_2O_2 + CO_2 \rightarrow Na_2CO_3 + (1/2)O_2. \qquad (2.63)$$
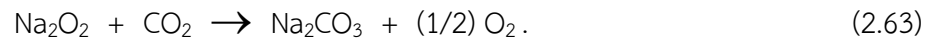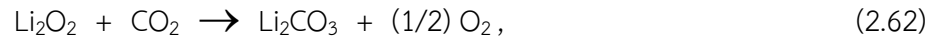
Therefore, the change in Gibbs free energy of the CO_2 capture reactions by Li_2O_2 and Na_2O_2 can be calculated using the expressions as follows:

$$\Delta G = G_{Li_2CO_3} + (1/2)G_{O_2} - G_{Li_2O_2} - G_{CO_2}, \qquad (2.64)$$

$$\Delta G = G_{Na_2CO_3} + (1/2)G_{O_2} - G_{Na_2O_2} - G_{CO_2}. \qquad (2.65)$$

Regarding the interpretation, the signs of ΔG (positive or negative) are employed to predict whether the reactions will occur spontaneously. If ΔG is negative, then it means that the summation of free energies for the products is lower than that of the reactants. This implies that the formation of the products is favored, occurring the forward reaction. In other words, the reaction will occur without added energy, but the rate of reaction is unknown. The reaction rate depends on the activation energy, E_a, on the reaction path, as shown in Figure 7. It increases with decreasing of E_a. On the contrary, if ΔG is positive, then it is likely to be the reverse reaction and unspontaneity. However, if ΔG is equal to zero, then it means that the reaction is in equilibrium [42].
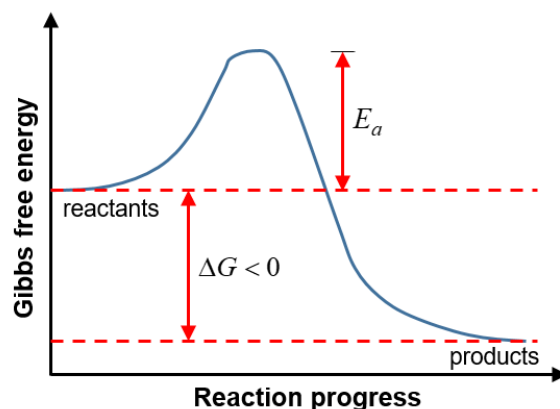
Figure 7: Gibbs free energy of the forward reaction is along the reaction path. The rate of reaction is conditioned by the activation energy (E_a) [42].

2.8 Raman scattering

Raman scattering or Raman effect is the inelastic scattering of light when interacts in the matter. The interaction of light with molecular vibrations or the vibrational optical modes of crystalline and amorphous materials lead to frequency shifts compared to the incident light. The decreased frequency and the increased frequency of the scattered light are called "Stokes" and "anti-Stokes" scattering, respectively. Raman effect is described by the quanta of vibrations, as shown in Figure 8. When photons interact with molecular vibrations, three events occur with different possibilities. First, the molecules are simulated to the 1st virtual excited state, and most of them release to the ground state together with emitting photons the same frequency as the incident photons. This process is known as Rayleigh scattering. Second, a smaller fraction of the scattered photons loses energy in the process because of the molecule's absorption. Thus, the frequency of them decreases from the incident photons. This is the process of the Stokes scattering. Finally, a very small fraction of molecules are initially in the 1st vibrational state due to the infrared absorption, and it is simulated to the 2nd virtual excited state by the incident photons. Therefore, they emit the scattered phonons with higher frequency than the incident phonon, when they return to the ground state.
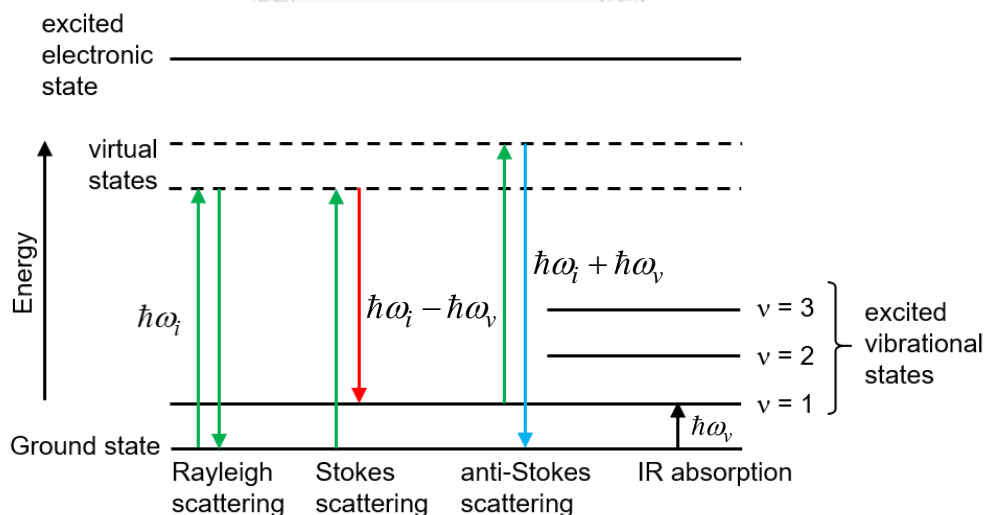
Figure 8: Three scattering processes of light: Rayleigh, Stoke, and anti-Stokes scatterings [43].

Based on the conservations of energy and momentum, the energy ($\hbar\omega_s$) and the momentum ($\hbar\vec{k}_s$) of the scattered photons are given by

$$\hbar\omega_i = \hbar\omega_s \pm \hbar\omega_v \quad \Rightarrow \quad \pm\hbar\omega_v = \hbar\omega_s - \hbar\omega_i , \tag{2.66}$$

$$\vec{k}_i = \vec{k}_s \pm \vec{q} \quad \Rightarrow \quad 0 \le |\vec{q}| \le 2|\vec{k}_i| \quad \Rightarrow \quad 0 \le |\vec{q}| \le \frac{4\pi n}{\lambda_i} , \tag{2.67}$$

where the subscript of 'i' and 's' represent that of the incident photons and the scattered photons. $\vec{k}$ is the photon's wavevector, while $\vec{q}$ is the difference in the wavevector between the incident and scattered photons [43].

From Eq. (2.66), Raman shift (in wavenumber) is given by

$$\Delta\omega(cm^{-1}) = \frac{1}{\lambda_s(nm)} - \frac{1}{\lambda_i(nm)} . \tag{2.68}$$

By considering the direction of the wavevectors between $\vec{k}_i$ and $\vec{k}_s$ as illustrated in Figure 9, the magnitude of $\vec{q}$ corresponds to 0, 0 - 2k, and 2k, respectively. Based on Eq. (2.67), if the photons wavelength of 5,000 Å is employed, then $|\vec{q}|$ is in the ranging from 0 to 0.002512 Å^{-1}. This implies that the optical phonons can interact with light at the Γ-point ($|\vec{q}|=0$) of the Brillouin zone. Therefore, the Raman activity can be calculated at the Γ-point.

(a) θ = 0⁰   (b) θ = 30⁰   (b) θ = 180⁰
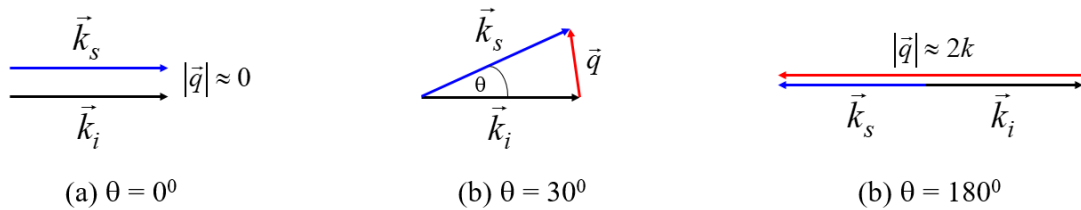
Figure 9: The magnitude of $\vec{q}$ at the different angle of θ: (a) 0⁰, (b) 30⁰, and (c) 180⁰ [43].

Chapter 3
Methodology

In this chapter, the computational details for Li_2O_2 and Na_2O_2 based on the DFT calculations will be described such as the structure searching, the structural phase transitions, and the change in Gibbs free energy of both CO_2 capture reactions. Besides, the high-pressure Raman measurements for Na_2O_2 will be also presented in detail.

3.1 Computational methods

3.1.1 Calculation details for investigating the structural phase transitions and the electronic properties of Li_2O_2 under high pressure

With regard to the structure searching of Li_2O_2, the USPEX code [40, 44] was employed to search the global structure of Li_2O_2 at high pressures up to 500 GPa. The searches were performed at the pressures of 0, 50, 100, 200, 300, and 500 GPa, respectively. USPEX was interfaced with the Vienna Ab initio simulation package (VASP) code with the projector augmented wave method [45, 46] to calculate the enthalpy structures at the considered pressures. The searches were performed with generating the different cells that contained Li and O atoms of 1-4 formula units (f.u.) per cell (1 f.u. consisting of 2 Li and 2 O atoms). In the searching process, the 30 randomized structures were conducted in the first generation. For the next generation, the two lowest enthalpy structures were selected by 60% and 20% of the previous generation for the heredity and the mutation processes, respectively. Then, the remaining 20% of the subjects were obtained by randomization. If the lowest enthalpy structure continuously maintained within 25 generations, the searches would be finished. Then, the predicted lowest-enthalpy structures at each pressure would be optimized using a more accurate criterion.

The structure searching results for Li_2O_2 were optimized and then calculated the considered properties, as shown in Figure 10(a). In order to optimize the structures in the pressure range of 0-500 GPa, an *ab initio* total-energy calculations program as implemented in the Cambridge Serial Total Energy Package (CASTEP) code [47], was employed with the BFGS algorithm [34], the PBE functional [28], and the ultrasoft

pseudopotentials [32] for Li: $1s^2 2s^1$ and O: $2s^2 2p^4$. A plane-wave basis set with a kinetic energy cutoff of 700 eV and a k-point grid spacing of $2\pi \times 0.04$ Å^{-1} were used. The ultrafine quality of calculation was employed as following the convergence tolerances: energy change less than 1.0×10^{-6} eV/atom, maximum force less than 1.0×10^{-4} eV/Å, maximum displacement within 5.0×10^{-4} Å, and maximum stress below 0.02 GPa.

(a)

Structure searching results for Li_2O_2

Optimizing structures using the CASTEP code, the PBE functional, and the ultrasoft pseudopotentials.

Optimized structures

Using the PBE functional within the supercell and finite displacement methods.

Using the PBE and HSE06 hybrid functionals.

Fitting the E-V curves using the third-order Birch-Murnaghan equations of states.

The band structures and density of states

The enthalpy-pressure curves

The Phonon dispersions and phonon density of states

(b)

Structure searching results for Na_2O_2

Optimizing structures using the CASTEP code, the PBE functional, and the ultrasoft pseudopotentials.

Optimized structures

Using the PBE functional within the supercell and finite displacement methods.

Using the PBE functional.

Using the PBE and HSE06 hybrid functionals.

Fitting the E-V curves using the third-order Birch-Murnaghan equations of states.

The Phonon dispersions and phonon density of states

The band structures and density of states

The enthalpy-pressure curves

Using the quasi-harmonic approximation

The elastic constants and universal elastic anisotropy index

The Gibbs free energy

Figure 10: Flowcharts of the computational details for: (a) Li_2O_2 and (b) Na_2O_2.

In order to obtain the pressure dependence of enthalpy for the predicted structures of Li_2O_2, the third-order Birch-Murnaghan equations of states [48] were employed to fit the relationship between the total energy (*E*) and the volume (*V*), and then the enthalpy (*H*) of each structure at the considered pressure (*P*) was calculated using the expression, *H* = *E* + *PV*. The enthalpies of the structures were compared using the plotting the enthalpy differences. Then, the lowest enthalpy structure at high pressures was considered as the most stable structure.

To investigate the dynamic stability and phonon behavior of the predicted structures at high pressures, the phonon dispersion curves and their phonon density of states were performed using the supercell and finite displacement methods [49]. Besides, the visualization of the crystal structures was illustrated using the VESTA program [50].

As for the electronic properties of Li_2O_2, the electronic band structure and partial density of states were determined using the PBE functional [28] at high pressures up to 500 GPa. Moreover, the predicted band gaps of structures were also calculated using the PBE and the HSE06 hybrid functionals [30] to compare the difference in band gaps between the considered structures. Besides, the electron density and the electron localization function [51] were determined to analyze the chemical bonding in Li_2O_2 at high pressures.

3.1.2 Calculation details for investigating the structural phase transitions and the electronic properties of Na_2O_2 under high pressure

Regarding the structure searching of Na_2O_2, the AIRSS method [38] was employed to find the lowest enthalpy structure in the pressure ranging from 0 GPa to 300 GPa. The searches were performed at 0, 10, 20, 30, 100, 200, and 300 GPa by constructing the unit cells that contained Na_2O_2 with 1, 2, 3, 4, and 6 f.u./cell, respectively. By generating many structures with the different lattice parameters, the different number of f.u., and reasonable volumes at each pressure, then the structures were fully relaxed to their local minima enthalpies. Here, the enthalpies (H) were estimated using the simple linear approximation at given pressures using Eq. (2.52). Then, the lowest enthalpy structure at each pressure was selected to optimize again with the more accurate convergence tolerances. Furthermore, the random unit cell deformations and random atomic displacements (or shaking) were also performed to create the mutated structures of the Tallman's and the Föppl's structures at ambient pressure.

The structure searching results for Na_2O_2 were optimized and then calculated the considered properties, as shown in Figure 10(b). Similar to Li_2O_2, all geometry optimizations of Na_2O_2 were conducted using the CASTEP code [47] combined with the BFGS algorithm [34], the PBE functional [28], and the ultrasoft pseudopotentials [32] for Na: $2s^2 2p^6 3s^1$ and O: $2s^2 2p^4$. A plane-wave basis set energy cutoff of 760 eV

and a k-point grid spacing of $2\pi \times 0.04$ Å^{-1} were employed. The criterion of the convergence tolerance was set as follows: energy tolerance less than 1.0×10^{-6} eV/atom, maximum force less than 0.01 eV/Å, maximum atomic displacement within 5.0×10^{-4} Å, and maximum stress below 0.02 GPa. Besides, to determine the vibrational and electronic properties, the structures were optimized again with the more accurate convergence tolerances for the grid spacing of $2\pi \times 0.02$ Å^{-1} and the maximum force less than 0.001 eV.

To predict the most stable structure of Na_2O_2 at high pressures up to 300 GPa, the third-order Birch-Murnaghan equations of states [48] were employed to fit the plot of the total energy (E) and the volume (V). Then, the enthalpies (H) for the considered structures at the pressure (P) were obtained from the formula: $H = E + PV$. Thus, the lowest enthalpy structure was found using the plotting of the enthalpies differences for the various structures *versus* pressure.

To investigate the dynamical stabilities and the vibrational properties of the predicted structures, phonon dispersions and their phonon density of states were calculated using the finite-displacement supercell method [52]. Furthermore, the thermodynamic stabilities of the predicted structures in the pressure range of 0-300 GPa and the temperature range of 0-600 K were also verified using the comparison of the Gibbs free energies differences (ΔG) between those structures. The Gibbs free energies, $G(P,T)$, based on the quasi-harmonic approximation were calculated using Eq. (2.53) and Eq. (2.57), as shown in chapter 2. The parameters in Eq. (2.57), $E(V)$ and $P(V)$ were obtained from the DFT calculations, which was fitted by the third-order Birch-Murnaghan equations of states. $F_{ph}(V,T)$ was calculated using Eq. (2.53). The volume dependence of $F_{ph}(V,T)$ at the fixed temperature was obtained from using the third-order polynomial fitting, and then the last term of $\partial F_{ph}(V,T)/\partial V$ was calculated at the different temperatures T. Finally, the pressure dependence of $G(P,T)$ at the same temperatures for the predicted structures were also obtained using the third-order polynomial fitting. By plotting the differences in $G(P,T)$ between the structures at the fixed pressures and varying temperatures, the lowest free energy structure at pressure P and temperature T was evaluated. These data were used to construct the P-T phase diagram of Na_2O_2.

To investigate the elastic properties and identify the difference between the predicted structure and the *P-62m* structure of Na$_2$O$_2$, elastic constants and elastic anisotropy for both structures under high pressure were calculated. The method for calculating elastic constants was conducted using applying a given homogeneous strain and calculating the resulting stress when the unit cell is fixed. The stress-strain relationship for each component of the stress was obtained by the linear fitting, and then its gradient yields the value of the elastic constant [31]. Moreover, to quantify the elastic anisotropy, the universal elastic anisotropy index (A^U) was calculated using the formula:

$$A^U = \frac{K^V}{K^R} + 5\frac{G^V}{G^R} - 6 \; , \tag{3.1}$$

where the superscripts R and V denote the lower (Reuss) and upper (Voigt) bounds for the bulk (K) and shear moduli (G) [53]. Here, the bulk (K_R, K_V) and shear moduli (G_R, G_V) were obtained from the elastic constants using the Voigt-Reuss-Hill approximations [54].

To determine the electronic properties and the evolution of chemical bonds in the predicted phases of Na$_2$O$_2$ at high pressures, the band structures and their partial density of states (PDOSs) were calculated using the PBE functional [28]. Moreover, the HSE06 hybrid functional [30] was also employed to calculate the band gaps of those structures to compare the difference in their band gaps. In addition, the electron localization function [51] at different pressures were calculated to discuss the pressure effect on the chemical bonding in the predicted phase (*Amm2*) of Na$_2$O$_2$.

3.1.3 Calculation details for determining the Gibbs free energy change of the CO$_2$ capture reactions by Li$_2$O$_2$ and Na$_2$O$_2$

To determine the thermodynamic stability of the CO$_2$ capture reactions by Li$_2$O$_2$ and Na$_2$O$_2$ at elevated pressures and temperatures, the Gibbs free energy change (ΔG) of both reactions were calculated using the expression, Eq. (2.64) and Eq. (2.65):

$$\Delta G = G_{Li_2CO_3} + (1/2)G_{O_2} - G_{Li_2O_2} - G_{CO_2} \; , \tag{2.64}$$

$$\Delta G = G_{Na_2CO_3} + (1/2)G_{O_2} - G_{Na_2O_2} - G_{CO_2} \; . \tag{2.65}$$

Here, the CO_2 capture reaction by Li_2O_2 (ΔG) at different pressures (8, 16, and 25 GPa) were calculated. In the same way, the CO_2 capture reaction by Na_2O_2 (ΔG) at different pressures (8, 15, and 30 GPa) were calculated. At these pressures, all reactants and products in both reactions are solid phases. Thus, their Gibbs free energies (G) obtained from Eq. (2.58):

$$G(P,T) \quad = \quad E_{tot}(V) + F_{ph}(V,T) + P(V)\, V - T\, S_{ph}(T)\,. \tag{2.58}$$

The predicted crystal structures of Li_2O_2 and Na_2O_2 at the considered pressures were used to calculate their Gibbs free energies. However, the crystal structures of Li_2CO_3, Na_2CO_3, CO_2, and O_2 proposed by the previous works were also used to calculate their Gibbs free energies are shown in Table 1.

Table 1: Details of structural data for Li_2CO_3, Na_2CO_3, CO_2, and O_2.

Compound	Pressure (GPa)	Temperature (K)	Crystal system	Space group	Reference
Li_2CO_3	8	~ 0 - 700	monoclinic	$C2/c$	Idemoto *et al.* [55]
Li_2CO_3	16, 25	~ 0 - 700	hexagonal	$P6_3/mcm$	Grzechnik *et al.* [56]
Na_2CO_3	8	~ 0 - 800	monoclinic	$C2/m$	Gavryushkin *et al.* [57]
Na_2CO_3	15	~ 0 - 800	hexagonal	$P6_3/mcm$	Gavryushkin *et al.* [57]
Na_2CO_3	30	~ 0 - 800	monoclinic	$P2_1/m$	Gavryushkin *et al.* [57]
CO_2	8	~ 0 - 700	cubic	$Pa\text{-}3$	Han *et al.* [58]
CO_2	15, 16	~ 0 - 500	orthorhombic	$Cmca$	Han *et al.* [58]
	25, 30	~ 0 - 550	tetragonal	$I\text{-}42d$	Lu *et al.* [59]
O_2	8	~ 250 - 370	hexagonal	$R\text{-}3m$	Schiferl *et al.* [60]
O_2	15, 16	~ 0 - 600	monoclinic	$C2/m$	Fujihisa *et al.* [61]
	25, 30	~ 0 - 1250			

3.2 Experimental methods

3.2.1 High-pressure technique

3.2.1.1 Diamond anvil cell

A diamond anvil cell (DAC) is a high-pressure device that has been widely used in scientific experiments. DAC can generate ultra-high pressure above 100 GPa. It is composed of a pair of diamond anvils, a pair of beryllium discs, a pair of stainless steel plates, a metal gasket, and three screws, as shown in Figure 11(a). The tables of

diamond anvils are stuck to the beryllium discs by the epoxy resin, and the faces of both anvil culets are aligned in parallel. The metal gasket is located between the anvil culets. A hole at the center of the pre-indented gasket was drilled using an electric discharge machine for serving as the sample chamber. The powder sample, a tiny ruby crystal, and the pressure-transmitting medium are loaded into the sample chamber, as shown in Figure 11(b). The pressure in the sample chamber can be increased or decreased by tightening or softening the screws.
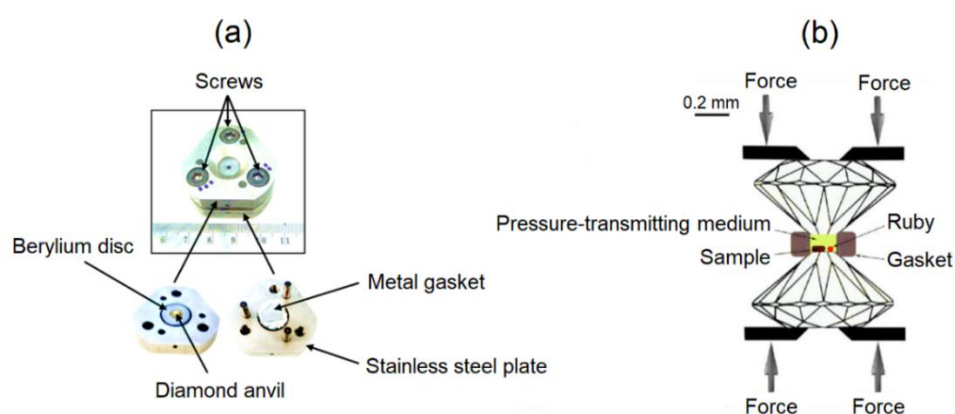
Figure 11: (a) Basic component of a Merrill-Bassett diamond anvil cell and (b) Schematic diagram of a diamond anvil cell [62].

Here, a Merrill-Bassett diamond anvil cell (DAC) was employed to generate pressure. To create a sample chamber with a diameter of around 120 μm, the tungsten gasket was drilled at the center of the pre-indented gasket with a thickness of 40-50 μm. In the process of sample loading, granular Na_2O_2 (Sigma-Aldrich, 97%) was transferred into a glove box in the atmosphere of argon gas (99.999%, purity), which was built by the author (see Appendix C). To avoid contact H_2O and CO_2, the granular Na_2O_2 was immersed in silicone oil (Sigma-Aldrich, 5 cSt), because silicone oil is almost chemically inert and available for the high-pressure x-ray diffraction and Raman scattering studies [63]. Then, it was milled to be powder using a mortar. Thus, the powdered Na_2O_2 was coated by silicone oil, and it was contained in a sample bottle filled with silicone oil. Next, the Na_2O_2 powder and a tiny ruby ship were loaded into the sample chamber in the DAC using silicone oil as a pressure-transmitting medium.

3.2.1.2 Ruby fluorescence technique

The ruby gauge is commonly used for pressure determination. Ruby (Al_2O_3: Cr^{3+}) has a strong luminescence with a doublet of peaks R_1 and R_2 at 694.2 and 692.8 nm under ambient conditions. With increasing pressure, the R-lines shift to higher wavelengths at approximately constant rates. Mao *et al.* [64] studied the pressure dependence of the R_1 line, and they proposed the calibration relation:

$$P = \frac{1904}{B}\left[\left(1+\frac{\Delta\lambda}{\lambda_0}\right)^B -1\right], \tag{3.2}$$

where P is in GPa, and $\Delta\lambda$ is the ruby R_1 line wavelength shift from its wavelength at ambient conditions (λ_0) in nanometers. The parameter B is equal to 5.000 and 7.665 for non-hydrostatic and quasi-hydrostatic conditions, respectively [65].
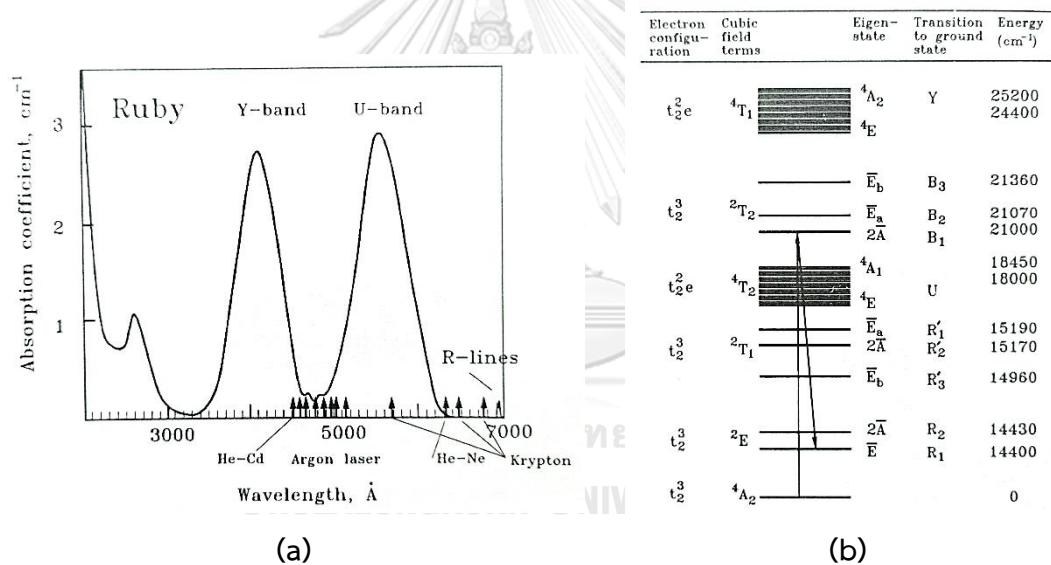
Figure 12: (a) Absorption spectrum of ruby crystal, (b) Electron energy levels of ruby. The cubic-field terms are split by both trigonal-field and spin-field coupling perturbations [65].

Figure 12(a) shows the absorption spectrum of ruby crystal. It revealed that electrons in ruby can absorb photons in a wide range of wavelengths and different absorption coefficients. If an electron is excited by the photon wavelength in the Y-band to the metastable state of $^2T_2$, then it is relaxed to the ^2E state with no radiation. The electron

in the ^{2}E metastable state will return to the ground state together with emitting the radiation of the R lines, as shown in Figure 12(b).

3.2.2 Raman spectroscopy

Raman spectroscopy is a very powerful technique for investigating the structural phase transition in the solid phase of the material. It provides a Raman spectrum, which is a distinct chemical fingerprint for the material. By measuring Raman shift or the frequency differences between the scattered phonons (ω_s) and the laser excitation line (ω_i), it relates to the optical phonons frequencies in the center of the Brillouin zone. When the structural phase transition is occurred by pressure or temperature or both, the vibrational modes of the original structure will be transformed, resulting in the change of Raman spectrum. Therefore, if the new Raman peak appears or the old Raman peak disappears, then it suggests the structural phase transition.

The components of the Raman spectroscopy system consists of a laser source, light sources, spectrograph, CCD detector, camera, notch filters, bandpass filters, spatial filters, and beam splitters, as shown in Figure 13. The incident light from the laser (green line) hits on the sample in the DAC, and then the scattered light (yellow line) moves to the CCD detector along with the optical arrangement. The different wavelengths of the scattered light will be separated and measured by the spectrograph and the CCD detector. The notch and bandpass filters are used to block the undesirable Rayleigh scattered light, while the spatial filters are used to reduce the spurious background.

In this work, Raman spectra of Na_2O_2 at high pressures up to 25 GPa and at room temperature were measured using a Raman microscope system operating with a laser wavelength of 532 nm at an intensity less than 100 mW. All Raman measurements were performed at the laboratory room on the 19th floor of the Department of Physics, Faculty of Science, Chulalongkorn University. In addition, the Raman spectrum of Na_2O_2 at ambient conditions was also measured at Thailand's National Electronics and Computer Technology Center (NECTEC) for comparing.
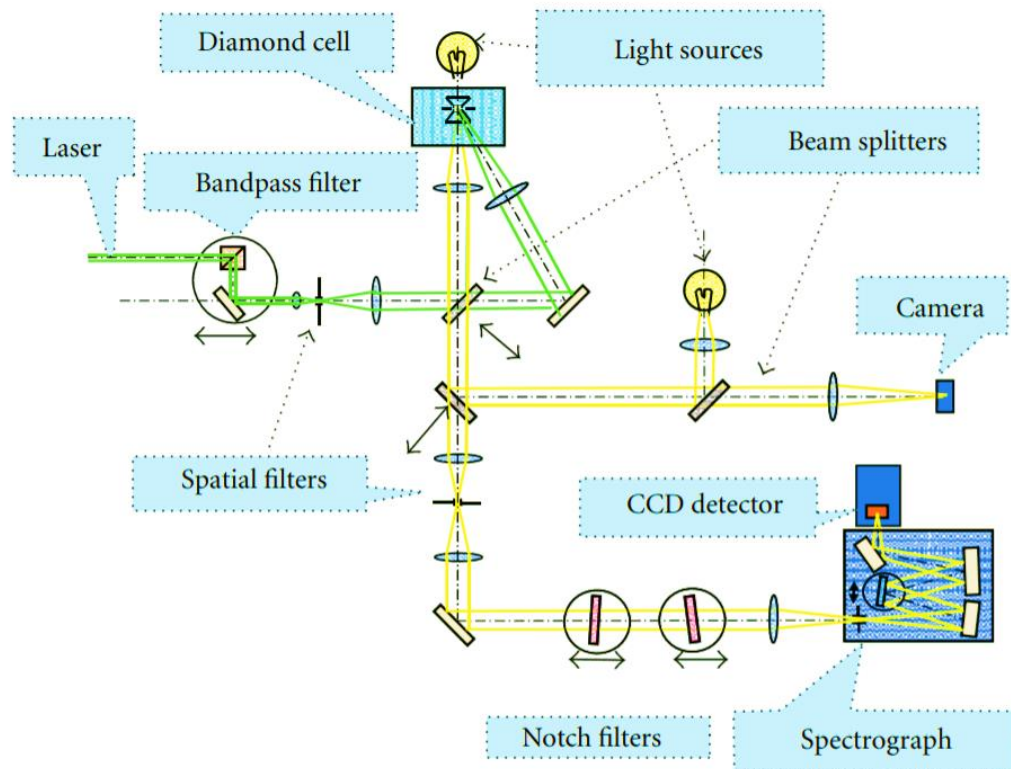
Figure 13: Schematic diagram of the Raman microscopy system for diamond anvil cells. Double-side arrows designate moving parts. The green and yellow lines represent the incident light and the scattered light, respectively [66].

Chapter 4
Results and discussions

This chapter will discuss the results consisting of the structural phase transitions of Li_2O_2 and Na_2O_2 and their related properties, the Gibbs free energy change of the CO_2 reactions by Li_2O_2 and Na_2O_2 at the considered pressures and temperatures, and the Raman spectra of Na_2O_2 at high pressures.

4.1 The structural phase transitions, the phonon behavior, and the electronic properties of Li_2O_2 under high pressure

4.1.1 The structure searching results for Li_2O_2

By using the structure searching for Li_2O_2 at high pressures up to 500 GPa, the lowest enthalpy structures at different pressures were found. The hexagonal $P6_3/mmc$ structures with 2 and 4 f.u./cell have the same enthalpy, and the enthalpy structure is lower than the $P1$ structure with 1 and 3 f.u./cell at 0 and 50 GPa. This result corresponds to the previous experimental results, which confirmed that the $P6_3/mmc$ structure is maintained up to 63 GPa [12, 17].

Interestingly, the monoclinic $P2_1$ structures with 2 and 4 f.u./cell at 100 GPa had a lower enthalpy than the monoclinic $P2_1/c$ with 2 and 4 f.u./cell and the monoclinic $C2/m$ structure with 1 f.u./cell at the same pressure. Nonetheless, the $P2_1$ structure was not found at 200 GPa, whereas the $P2_1/c$ structure with 2 f.u./cell was found up to 500 GPa. This implied that the $P2_1$ structure is likely to transform into the $P2_1/c$ structure in the pressure range of 100-200 GPa.

4.1.2 The structural phase transitions of Li_2O_2 at high pressures

From the structural searching results, the $P6_3/mmc$ structure with 2 f.u./cell at ambient pressure had the lowest enthalpy. Its relaxed lattice constants were of a = 3.1858 Å and c = 7.7182 Å, which are consistent to the experimental values of 3.1692 and 7.7140 Å [15] and the previously predicted values of 3.1830 and 7.7258 Å [14].

To investigate the structural phase transitions of Li_2O_2 in the 0-500 GPa pressure range, the difference in enthalpy of the predicted structures compared to the $P2_1/c^{\dagger}$ structure predicted by Deng *et al.* [16] *versus* pressure were plotted in Figure 14(a). The $C2/m$

structure was found at 100 GPa and not found at a higher pressure. At ambient pressure, the $C2/m$ structure was lower in enthalpy than the $P2_1/c$ structure by ~20 meV/f.u., and its enthalpy became higher than that of the $P2_1/c$ structure by ~58 meV/f.u. at 100 GPa. As for the structural phase transition, Figure 14(a) suggested that the $P6_3/mmc$ structure at 75 GPa is transformed into another structure, which is justified by their thermodynamic stability. Here, the candidate structures consist of the $P2_1$ and the $P2_1/c$ structures, which have a small energy difference. Moreover, the $P2_1$ structure is not found at 200 GPa, and it is dynamical instability at 150 GPa because the imaginary phonon frequencies appear around the Γ-point [see Figure 20(b)]. Thus, to verify the most stable structure of them, the enthalpy difference between the $P2_1$ and the $P2_1/c$ structures versus pressure in the 50-150 GPa range was fitted again and plotted, as shown in Figure 14(b). Here, the enthalpies at around 75 and 135 GPa are indistinguishable, but the $P2_1$ structure at 100 GPa becomes more stable than the $P2_1/c$ structure with a small enthalpy difference of 2 meV/f.u., which corresponds to the structure searching result. Furthermore, the $P2_1$ structure is higher in enthalpy than the $P2_1/c$ structure at ~136 GPa, and its enthalpy becomes 2 meV/f.u. at 150 GPa. Therefore, these suggest that the $P2_1$ structure may be stable in the 75-135 pressure, and it transforms into the $P2_1/c$ structure at a pressure above 136 GPa.
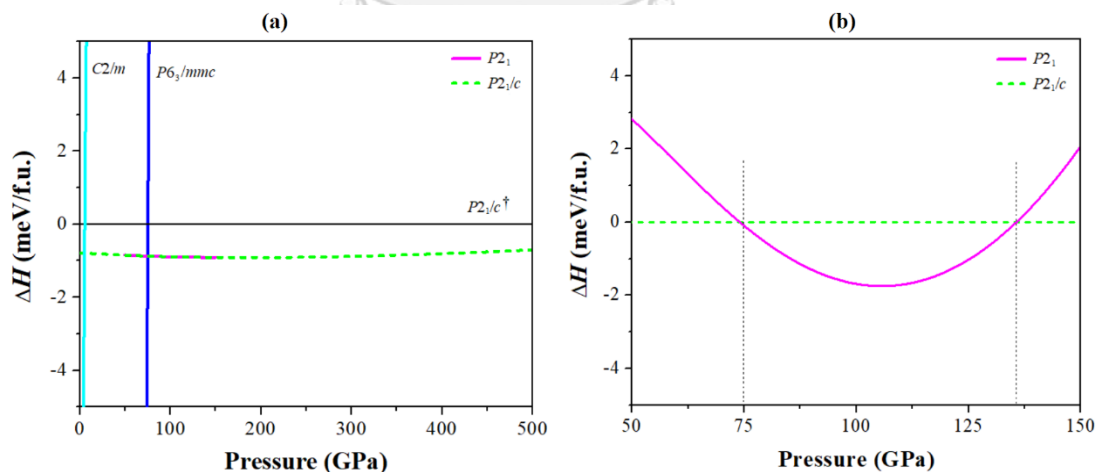
Figure 14: (a) Plot of the enthalpy differences of the various structures compared to the $P2_1/c$ structure predicted by Deng et al. [16] (denoted as $P2_1/c^\dagger$ hereafter) versus pressure at 0-500 GPa, (b) Plot of the enthalpy difference of the $P2_1$ structure compared to the $P2_1/c$ structure in the pressure range of 50-150 GPa [67].

With increasing pressure, the $P6_3/mmc$ structure, the z-coordinate of the O atom (O_z) displaced, and the bond length of the peroxide group (O-O) decreased, as shown in Figure 15(a) and 15(b), respectively. However, the O_z and the O-O bond length unusually changed at around 11 and 40 GPa. The O_z displacement from 10 GPa to 11 GPa was 0.0057 Å, which was twice of the displacement from 10 GPa to 11 GPa on the trend line. Similarly, the O_z displacement from 39 GPa to 40 GPa was 0.0031 Å, which was twice of the displacement from 39 GPa to 40 GPa on the trend line, leading to the O-O bond length increasing of 0.0024 Å at 11 GPa and 0.0017 Å at 40 GPa compared to the bonds at 10 and 39 GPa, respectively. This corresponds to the O_z measured by Dunuwille et al. [17] The O_z unusually increased at ~11 and ~40 GPa. Besides, by considering the ratio of lattice constants (c/a), it is unusually decreased by pressure at around 11 and 40 GPa because the 'c' has a higher reduction rate than that of the 'a', as shown in Figure 15(b). Likewise, the 'c' at 11 GPa differs from its constant on the trend line by 0.018 Å and that of 0.009 Å at 40 GPa, and the decreasing of the 'c' from 10 GPa to 11 GPa is double that from 39 GPa to 40 GPa similar to the decreasing of the 'a'.
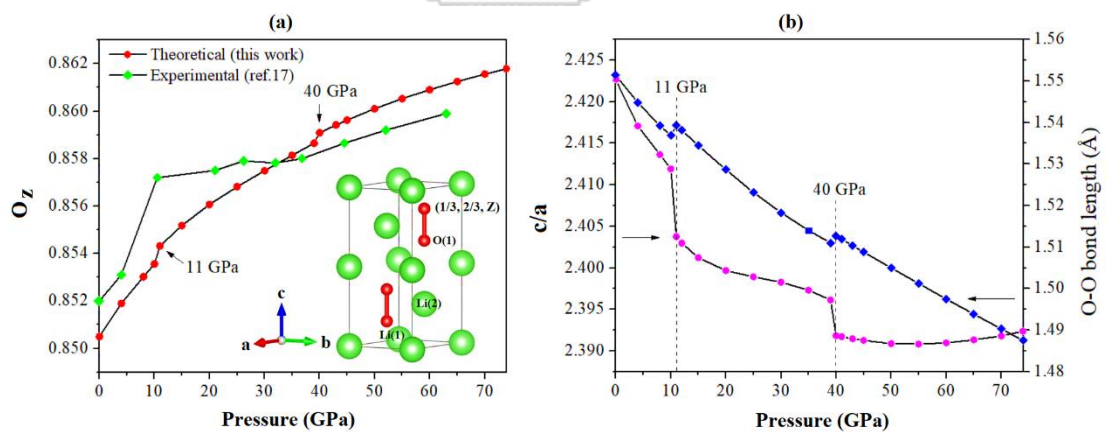
Figure 15: (a) Plots of the z-coordinate of the O atom (O_z) versus pressure in the 0-74 GPa pressure range compared to the experimental results proposed by Dunuwille et al. [17], (b) Plots of the c/a ratio and the O-O bond length in the $P6_3/mmc$ structure versus pressure in the same range [67].

According to Wu *et al.* [68], they also predicted that the bulk modulus at ambient pressure along the c-axis (B_c) is more than that of along the a-axis (B_a); $B_a/B_c = 0.589$.

They described that because the O-O bonds along the c-axis is stronger than the Li-Li and Li-O bonds. Nonetheless, the present work predicted that the bulk modulus along the c-axis is less than that of along the a-axis in the 10-11 GPa and 39-40 GPa pressure ranges. In addition, Dunuwille *et al.* [17] also reported a wide variation of the c/a ratio in the same pressure ranges. Therefore, these results suggest that the O_z displacement results in the significant decreasing of the c/a ratio at 11 and 40 GPa.

To analyze the unusual decreasing of the 'c' and the increasing of the O-O bond length of the $P6_3/mmc$ structure at 11 and 40 GPa, the electron localization function (ELF) [51] which indicates the shared electron in the O-O bonds was calculated in the 0-70 GPa pressure range. The findings revealed that the ELF value of the O-O bonds increase in the 8-11 and 39-40 GPa pressure ranges (Figure 16), leading to the softening of the O-O bonds along the c-axis and the softening of the 'c'. These suggest the presence of the O_z displacement in the $P6_3/mmc$ structure.
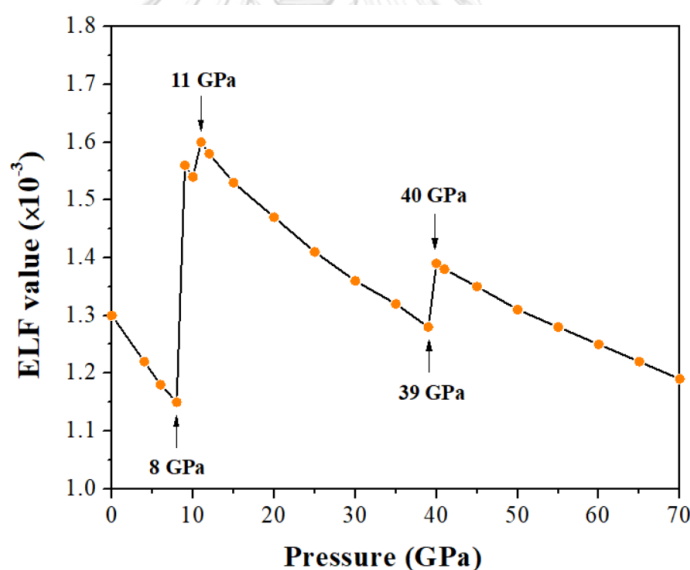
Figure 16: Plot of the ELF value for the P6₃/mmc structure versus pressure in the range of 0-70 GPa [67].

At the transition pressure of 75 GPa, Li and O atoms in the $P6_3/mmc$ structure translate to the new atomic positions in the $P2_1$ structure, as shown in Figure 17(b). The O-O bond length and the volume of the $P2_1$ structure are reduced by 1.85 and 2.87% compared to that of the $P6_3/mmc$ structure, respectively. For the $P2_1$ structure, the average of the nearest-neighbor interatomic distances of Li-O (1.8335 Å) is longer than

the average distance (1.8080 Å) in the $P6_3/mmc$ structure. This suggests that the phase transition at 75 GPa results in decreasing of the electrostatic interaction between the Li and O atoms. Besides, the alignment of the peroxide anions (O-O) in the $P2_1$ structure is tilted from the c-axis about 20 degrees in the $P6_3/mmc$ structure.
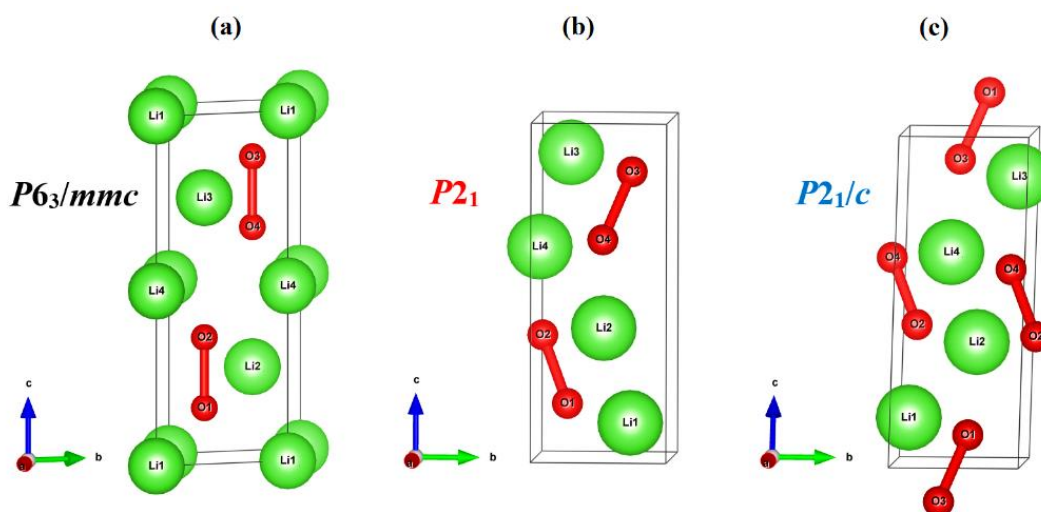
Figure 17: The three crystal structures of Li_2O_2: (a) $P6_3/mmc$ at 0 GPa, (b) $P2_1$ at 75 GPa, and (c) $P2_1/c$ at 136 GPa [67].

However, the structural phase transition at 75 GPa is significantly different from the previous work, which was proposed that the $P6_3/mmc$ structure transforms into the monoclinic $P2_1/c^\dagger$ structure at ~84 GPa. Here, the $P2_1$ structure at 75 GPa is lower in enthalpy than the $P2_1/c^\dagger$ structure about 1 meV/f.u. [see Figure 14(a)], which may be significant at extremely low temperatures. Therefore, it is likely that the high-pressure phase of Li_2O_2 at 75 GPa favors the $P2_1$ structure rather than the $P2_1/c^\dagger$ structure. The structural data for the $P6_3/mmc$, the $P2_1$, the $P2_1/c$, and the $P2_1/c^\dagger$ structures are shown in Table 2.

At the transition pressure of 136 GPa, Li and O atoms in the $P2_1$ structure translate to the new atomic positions in the $P2_1/c$ structure, as shown in Figure 17(c). The O-O bond lengths and the volumes of the $P2_1/c$ and the $P2_1$ structures are not different. Likewise, the average of the nearest-neighbor interatomic distances of Li-O distances (1.7513 Å) in the $P2_1/c$ structure is insignificantly different from that of the distance (1.7512 Å) in the $P2_1$ structure. Nevertheless, the peroxide anions (O-O) are aligned on

the (100) plane of the $P2_1/c$ structure, which deviated from the alignment in the $P2_1$ structure about 22 degrees. Furthermore, the $P2_1/c$ structure was lower enthalpy than that of the $P2_1/c^\dagger$ structure about 1 meV/f.u.. To compare the difference between both structures, the $P2_1/c$ structure was transformed into the most similar configuration of the $P2_1/c^\dagger$ structure using the COMPSTRU program proposed by Flor *et al.* [69]. The results revealed that the $P2_1/c$ and the $P2_1/c^\dagger$ structures at 150 GPa are significantly different by the similarity measurement value (Δ) of 0.445.

To determine the driving force that leads to the structural phase transitions, the normalized lattice constants, the β cell angle (angle between the a- and c-axes), and the interatomic distances *versus* pressure for the $P6_3/mmc$, the $P2_1$, and the $P2_1/c$ structures were plotted, as shown in Figure 18. At the transition pressure of 75 GPa, the lattice constants 'a' and 'b' are collapsed larger than the 'c' since the interactions of Li-Li on the ab-plane are weaker than the interactions of the O-O bonds along the c-axis [Figure 18(a)], resulting in change of the β angle [Figure 18(b)]. This result is in agreement with the collapses of the Li(1)-Li(2) and Li(2)-Li(2) distances during the $P6_3/mmc$ to $P2_1$ phase transition [Figure 18(c)], which relates to the alignment of the Li atoms in the $P2_1$ structure with respect to the sequence stacking of the Li atoms in the $P6_3/mmc$ structure.

Table 2: The predicted structural data of Li_2O_2 for the $P6_3/mmc$, the $P2_1$, the $P2_1/c$, and the $P2_1/c^\dagger$ structures at different pressures [67].

Pressure (GPa)	Space group	Lattice parameters				Atom	Site	Atomic coordinates		
		a (Å)	b (Å)	c (Å)	β (degree)			x	y	z
0	$P6_3/mmc$	3.1858	3.1858	7.7182	90.0000	Li(1)	2a	0.00000	0.00000	0.00000
						Li(2)	2c	0.33333	0.66667	0.25000
						O(1)	4f	0.33333	0.66667	0.64950
10	$P6_3/mmc$	3.0767	3.0767	7.4208	90.0000	Li(1)	2a	0.00000	0.00000	0.00000
						Li(2)	2c	0.33333	0.66667	0.25000
						O(1)	4f	0.33333	0.66667	0.64645
11	$P6_3/mmc$	3.0694	3.0694	7.3780	90.0000	Li(1)	2a	0.00000	0.00000	0.00000
						Li(2)	2c	0.33333	0.66667	0.25000
						O(1)	4f	0.33333	0.66667	0.64568

Pressure (GPa)	Space group	Lattice parameters				Atom	Site	Atomic coordinates		
		a (Å)	b (Å)	c (Å)	β (degree)			x	y	z
39	$P6_3/mmc$	2.9020	2.9020	6.9536	90.0000	Li(1)	2a	0.00000	0.00000	0.00000
						Li(2)	2c	0.33333	0.66667	0.25000
						O(1)	4f	0.33333	0.66667	0.64135
40	$P6_3/mmc$	2.8987	2.8987	6.9332	90.0000	Li(1)	2a	0.00000	0.00000	0.00000
						Li(2)	2c	0.33333	0.66667	0.25000
						O(1)	4f	0.33333	0.66667	0.64091
75	$P2_1$	2.5695	2.5942	6.4767	91.8505	Li(1)	2a	0.84403	0.72368	0.11400
						Li(2)	2a	0.65603	0.51017	0.38600
						O(1)	2a	0.34300	0.21666	0.15252
						O(2)	2a	0.15705	0.01719	0.34747
75	$P2_1/c$	2.5695	2.5941	7.0454	113.2454	Li	4e	0.45790	0.89333	-0.13599
						O	4e	-0.00463	0.40036	-0.09748
136	$P2_1$	2.4424	2.4876	6.1569	89.7118	Li(1)	2a	0.85698	0.72372	0.11396
						Li(2)	2a	0.64303	0.51011	0.38604
						O(1)	2a	0.35399	0.22011	0.14973
						O(2)	2a	0.14603	0.01376	0.35026
136	$P2_1/c$	2.4423	2.4877	6.6119	111.3833	Li	4e	0.47094	0.89325	-0.13607
						O	4e	0.00379	0.39687	-0.10025
150	$P2_1/c$	2.4194	2.4703	6.5333	110.9788	Li	4e	0.47361	0.89276	-0.13616
						O	4e	0.00547	0.39595	-0.10074
150	$P2_1/c$ (similar)[¶]	6.1008	2.4703	6.5333	158.2667	Li	4e	0.52639	0.60724	0.89023
						O	4e	0.99453	0.10405	0.39379
150	$P2_1/c$[†]	6.1009	2.4703	6.5926	158.4716	Li	4e	0.74587	0.60726	0.10975
						O	4e	0.20690	1.10404	-0.39386
300	$P2_1/c$	2.2464	2.3473	5.9562	107.5213	Li	4e	0.49472	0.88747	-0.13824
						O	4e	0.01976	0.38790	-0.10386
500	$P2_1/c$	2.1174	2.2416	5.5723	105.4396	Li	4e	0.49349	0.61747	1.14122
						O	4e	0.96991	0.11908	1.10491

[†] Reference [16]

[¶] Structural data obtained using the COMPSTRU program proposed by Flor et al. [69].
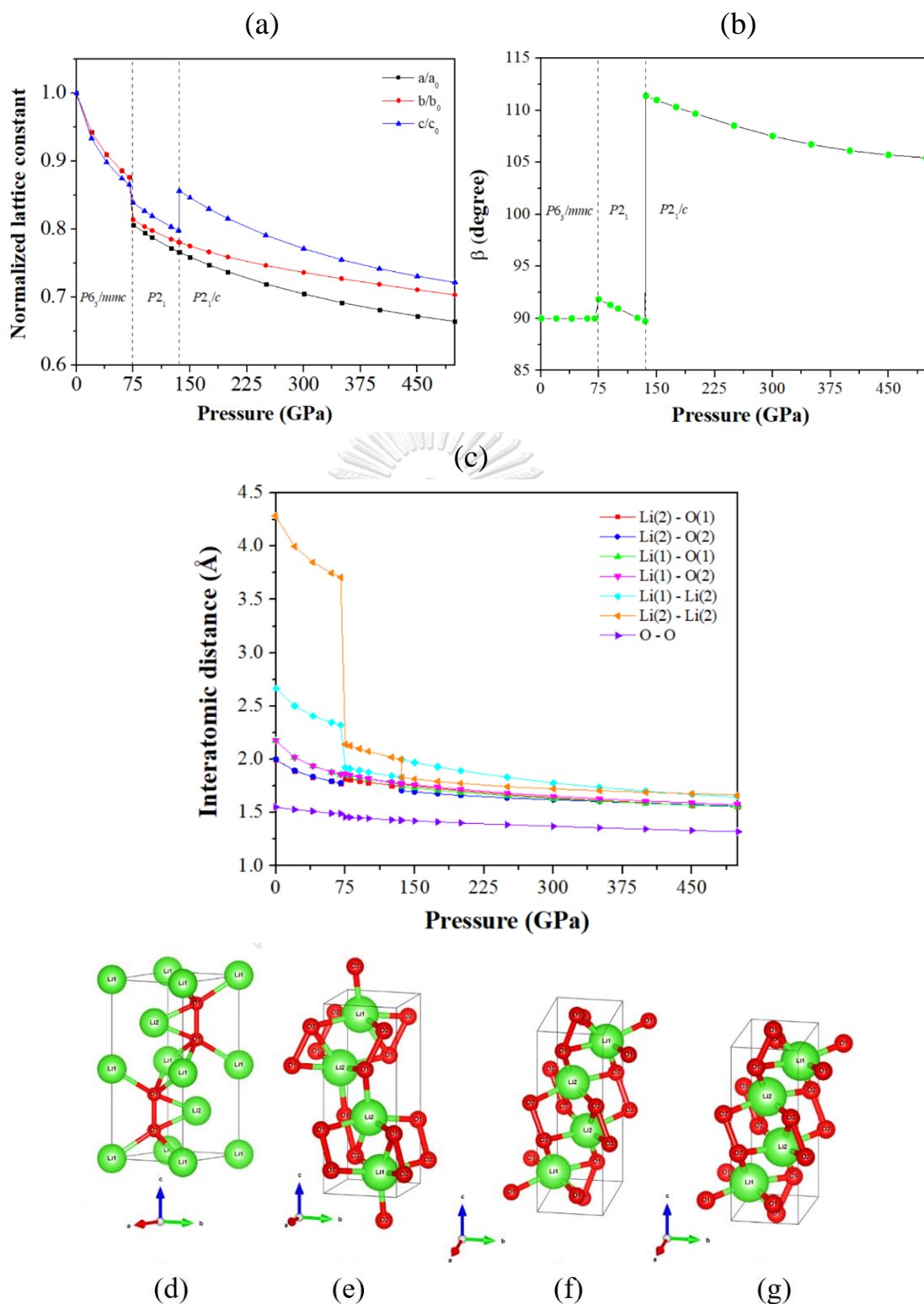
Figure 18: (a) Plot of the normalized lattice constants versus pressure, (b) Plot of the β versus pressure, (c) Plot of the interatomic distance versus pressure, (d) the P6₃/mmc structure at 0 GPa, (e) the P2₁ structure at 75 GPa, (f) the P2₁/c structure at 150 GPa, and (g) the P2₁/c structure at 500 GPa [67].

By considering the arrangement of atoms in the $P6_3/mmc$ structure, it was described as AcBcAbCbA, where the capital and small letters stand for the Li and O atoms [14]. The driving force at the phase transition of 75 GPa is assigned by the alignment of the Li atoms in the $P6_3/mmc$ structure, leading to the changes of the lattice parameters. As for the structural phase transition at 136 GPa, the 'a' and 'b' usually decrease [Figure 18(a)], but the 'c' and the 'β' increase [Figure 18(b)]. In addition, the unusual changes in the Li(1)-Li(2) and Li(2)-Li(2) distances also appear at 136 GPa [Figure 18(c)]. These imply that the driving force for the $P2_1$ to the $P2_1/c$ phase transition is also assigned by the alignment of the Li atoms in the $P2_1$ structure.

Moreover, the atomic displacements in the coordinates of Li and O atoms (see Table 2) result in the local distortion of peroxide anions in the pressure range of 75-500 GPa and the peroxide anions tilting from the c-axis by angles of ~20, ~22, ~23, and ~25 degrees at around 75, 150, 300, and 500 GPa, respectively. In terms of the Li-O coordination at ambient pressure, the Li atom is coordinated to the six neighboring of O atoms with the same distance of 1.9962 Å, while the O atoms in the peroxide anion are coordinated to the six neighboring of Li atoms with the distances of 2.1713 Å for O-Li(1) and 1.9962 Å for O-Li(2) and are changed to 1.8503 Å and 1.7695 Å at 74 GPa. This exhibits that the distances are decreased by 14.78% for O-Li(1) and 11.36% for O-Li(2). Furthermore, the coordination numbers of the six Li and O atoms in the pressure range of 75-500 GPa are the same, but there are differences in the Li-O distances. That is 1.7769, 1.8481, 1.8224, 1.8629, 1.8374, 1.8533 Å at 75 GPa, they become 1.5609, 1.5487, 1.5539, 1.5541, 1.5593, 1.5735 Å at 500 GPa, respectively. These distances are decreased by 12.16, 16.20, 14.73, 16.58, 15.13, and 15.10%, respectively. It suggests that the Li-O distances are largely distorted within the same polyhedron, and it is likely to have anisotropic distortions in the $P2_1$ and the $P2_1/c$ structures of Li_2O_2.

4.1.3 The phonon behavior of Li_2O_2 at high pressures

To determine the consequence of the unusual increase of the O-O bond lengths in the $P6_3/mmc$ structure at 11 and 40 GPa as discussed before, the partial phonon density of states (PDOSs) of O at 10, 11, 12, 39, 40, and 41 GPa were calculated, as shown in Figure 19. The highest phonon frequency corresponding to the O-O stretching mode is 24.13, 24.00, 24.10, 26.63, 26.56, and 26.65 Hz at 10, 11, 12, 39, 40, and 41

GPa, respectively. Interestingly, the frequency at 11 and 40 GPa significantly decrease and then increase with elevated pressure. This result is in agreement with the unusual increase of the O-O bond lengths in the $P6_3/mmc$ structure. Consequently, it is possible to note that the O-O bonds are softened by pressures at 11 and 40 GPa.
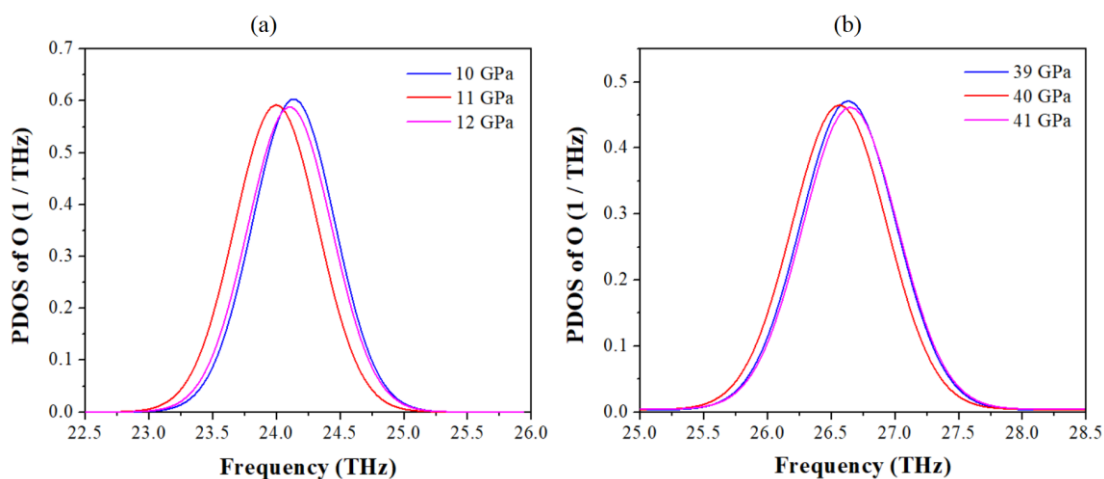
Figure 19: The phonon density of states (PDOSs) of O corresponding to the O-O stretching mode in the P6₃/mmc structure at: (a) 10-12 GPa and (b) 39-41 GPa [67].

To verify the dynamic stability of the $P2_1$ and the $P2_1/c$ structures, their phonon dispersions and PDOSs were calculated. The results showed that there is no imaginary phonon frequency in the phonon dispersion curve of the $P2_1$ structure at 75 GPa [Figure 20(a)], but there are a few negative frequencies around the Γ-point at 150 GPa [Figure 20(b)]. This implied that the $P2_1$ structure is dynamically stable at 75 GPa but unstable at 150 GPa, while the $P2_1/c$ structure is dynamically stable at 75, 150, 300, and 500 GPa [Figure 21(a)-(d)]. The highest phonon frequency of the O-O stretching mode increases from ~32 THz at 75 GPa to ~49 THz at 500 GPa. Furthermore, a gap that divided the low- and high-frequency regimes which represent the decoupling of the peroxide anions from the rest of lattice [70] in the $P2_1$ and $P2_1/c$ structures was decreased by increasing pressure. This suggested that the Li-O electrostatic interaction increases with elevated pressure leading to the Li-O phonon coupling, which contributes to a broader frequency band.
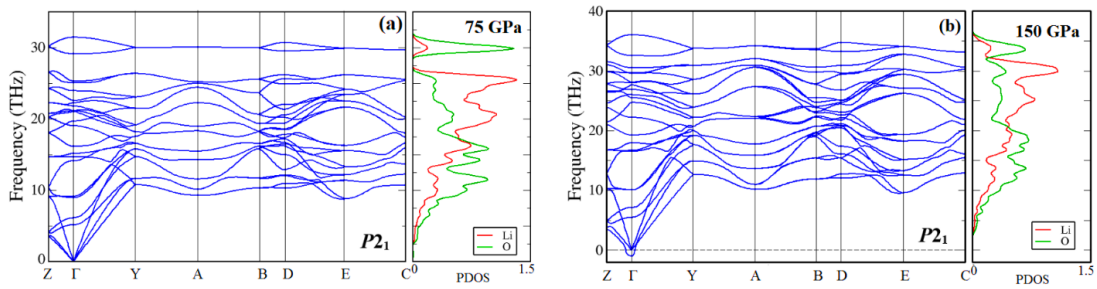
Figure 20: Phonon dispersion curves and PDOSs for the $P2_1$ structure at: (a) 75 GPa and (b) 150 GPa [67].
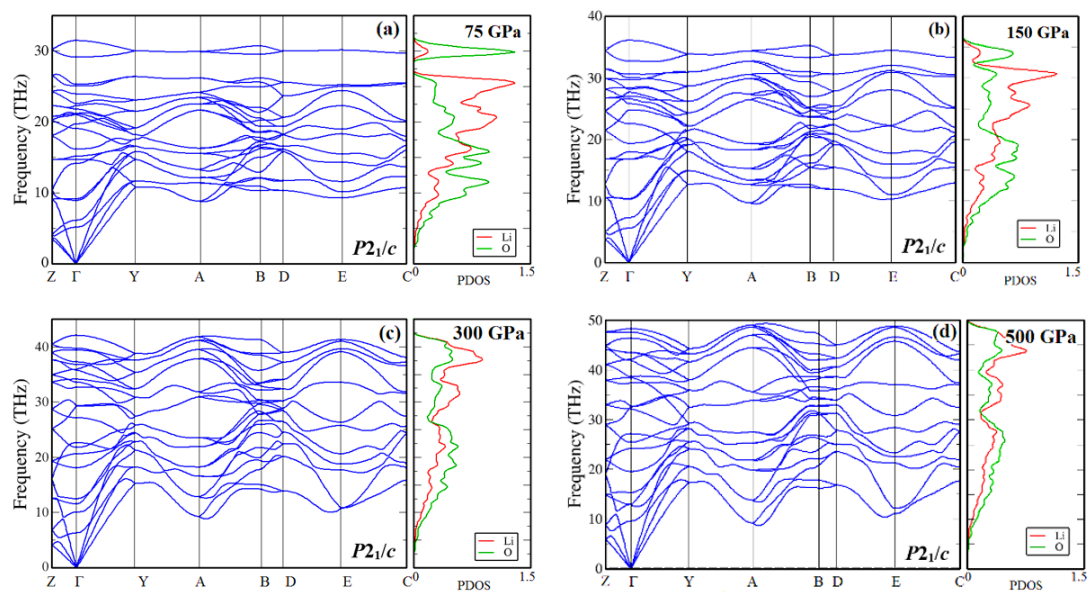
Figure 21: Phonon dispersion curves and PDOSs for the $P2_1/c$ structure at different pressures: 75, 150, 300, and 500 GPa for (a)-(d), respectively [67].

To identify the difference between the $P2_1/c$ and the $P2_1/c^{\dagger}$ structures, the $P2_1/c$ structure was transformed into the most similar configuration of the $P2_1/c^{\dagger}$ structure using the COMPSTRU program proposed by Flor et al. [69] Then, the phonon dispersions of both structures at 150 GPa were calculated using the same Brillouin zone paths. The result revealed that the differences in both phonon dispersion curves appear in the Y-A and E-C paths, as marked by the yellow and black rectangular dashed lines in Figure 22. Furthermore, the PDOS of the O-O stretching mode in the $P2_1/c$ structure is slightly higher than that of the $P2_1/c^{\dagger}$ structure. Thus, it is possible to note that the $P2_1/c$ and the $P2_1/c^{\dagger}$ structures are slightly different.
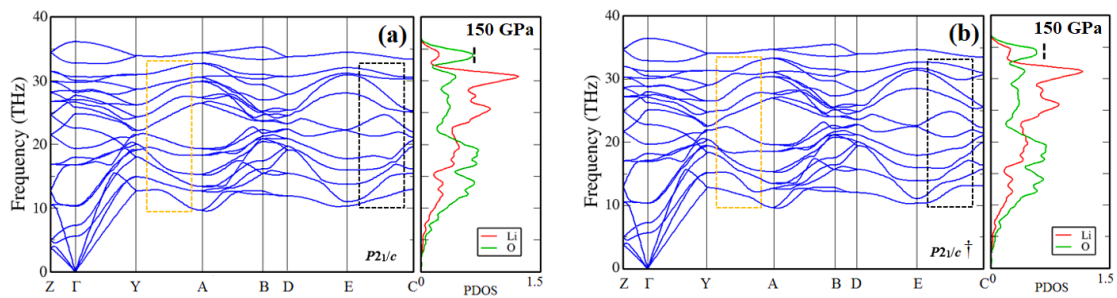
Figure 22: Phonon dispersion curves and PDOSs for the $P2_1/c$ and the $P2_1/c^{\dagger}$ structures at 150 GPa. The yellow and black rectangular dashed lines mark the differences regimes between the $P2_1/c$ and the $P2_1/c^{\dagger}$ structures along the Y-A and E-C paths. The vertical dashed lines mark the PDOS of the O-O stretching mode for the $P2_1/c$ structure [67].

4.1.4 The electronic properties of Li_2O_2 at high pressures

To determine the electronic properties of Li_2O_2 under high pressure, the band structures and partial density of states (PDOSs) for the predicted structures were calculated using the PBE functional [28]. Moreover, the HSE06 hybrid functional [30], which provides a more reliable band gap than the PBE and LDA functionals were also employed to calculate their band gaps for comparing to the PBE band gaps.

The PBE and HSE06 band gaps of the predicted structures in the 0-500 GPa pressure range are shown in Figure 23(a). The PBE band gap of 2.05 eV at ambient pressure is lower than the HSE06 band gap of 4.18 eV. According to Radin *et al.* [71], they also reported that the PBE and the HSE06 band gaps are of 1.99 and 4.19 eV, respectively. With elevated pressure, the PBE and the HSE06 band gaps of the $P6_3/mmc$, the $P2_1$, and the $P2_1/c$ structures increase with the same trends.

At the transition pressure of 75 GPa, the PBE band gap of the $P2_1$ structure (3.43 eV) is higher than that of the $P6_3/mmc$ structure (2.60 eV) by ~0.8 eV. Likewise, the HSE06 band gap of the $P2_1$ structure (5.70 eV) is higher than that of the $P6_3/mmc$ structure (4.98 eV) by ~0.7 eV. Moreover, the maximum difference of the PBE band gap between the $P2_1$ and the $P2_1/c$ structures in the 75-125 GPa pressure range is approximate to 5 meV. Even though it is slightly different, the trend line of the HSE06 band gap [dashed line in Figure 23(a)] suggests the significant difference between the band gaps of the

$P2_1$ and the $P2_1/c$ structures. Because the trends of the PBE and the HSE06 band gaps are consistent, the PBE band gaps are acceptable. Consequently, the electronic band structures calculated using the PBE functional were mainly employed to discuss the structural evolution of Li_2O_2 under high pressure.
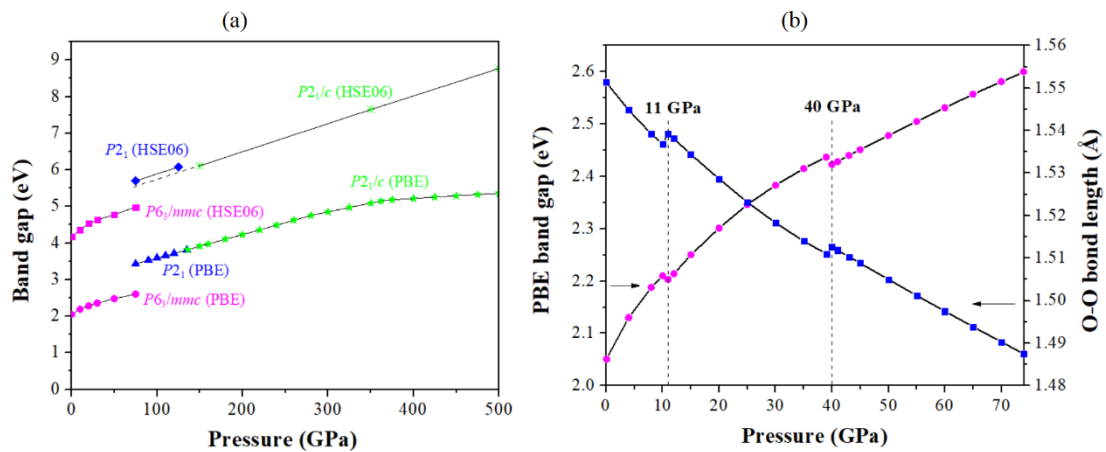
Figure 23: (a) Plots of the PBE and HSE06 band gaps of the $P6_3/mmc$, the $P2_1$, and the $P2_1/c$ structures versus pressure (b) Plots of the PBE band gap of the $P6_3/mmc$ structure and the O-O bond length versus pressure [67].

In addition, by comparing the HSE06 band gap between the $P2_1/c$ and the $P2_1/c^\dagger$ structures at 150 GPa, the HSE06 band gap of the $P2_1/c$ structure is less than that of the $P2_1/c^\dagger$ structure by 0.18 eV. Interestingly, the PBE band gap of the $P6_3/mmc$ structure decreases at around 11 and 40 GPa, as shown in Figure 23(b). The band gaps decrease ~0.01 eV at 11 GPa and ~0.02 eV at 40 GPa with respect to the band gaps at 10 and 39 GPa, respectively. Moreover, the trend of the band gap in the pressure range of 0-75 GPa increases, when the O-O bond length decreases. The band gap depends on the energy difference between the bottom conduction band and the top valence band. Here, the O-O bond relates to the p-state of O, which mainly contributes to the valence and conduction bands. When the O-O bond length is decreased by increasing pressure, the electrons are more tightly bound to the atom, thus it requires more energy to remove. That is, the shorter O-O bond length yields the wider band gap. This suggests that the band gap of the $P6_3/mmc$ structure closely relates to the O-O bond length. However, the band gap immediately decreases, while the O-O bond length increases at 11 GPa and 40 GPa, which occur at the same pressures with the unusual

decrease in the c/a ratio as discussed before. Consequently, these imply that the unusual decrease in the band gap of the *P6₃/mmc* structure at 11 and 40 GPa results in the atomic displacement of O in the z-coordinate (O_z).

Regarding the electronic band structures and partial density of states (PDOSs) for the *P6₃/mmc*, the *P2₁*, and the *P2₁/c* structures at different pressures (Figure 24), their valence and conduction bands are mainly contributed from the p-states of O and partially contributed from the s-state of Li. The band structure of the *P6₃/mmc* structure at ambient pressure revealed that the valence band maximum (VBM) is not exactly at the Γ-point, but it is at a point within the Γ-M path beyond the Γ-point [inset Figure 24(a)]. Thus, the *P6₃/mmc* structure is the indirect bandgap of 2.05 eV. With increasing pressure, the valence band shifts to lower energy, while the conduction band shifts to higher energy, resulting in the increasing of band gaps. The VBM of the *P2₁* structure is exactly at the Γ-point of the Brillouin zone, whereas the VBM of the *P2₁/c* structure is at the B-point in the 150-280 GPa pressure range and moves to the C-point in the 280-500 GPa.
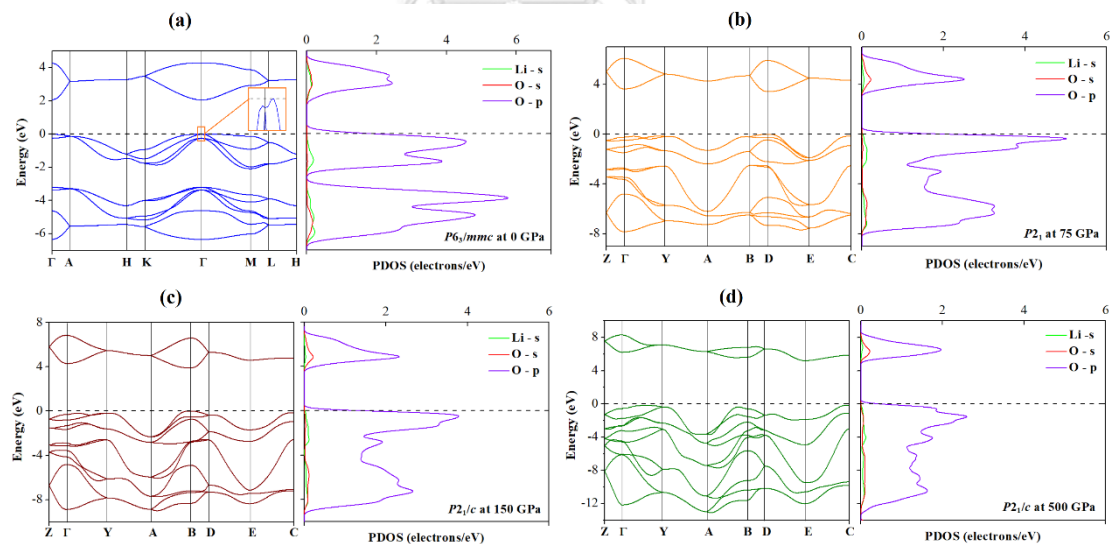
Figure 24: Electronic band structures and partial density of states (PDOSs) for three crystal structures of Li₂O₂: (a) the P6₃/mmc structure at 0 GPa, (b) the P2₁ structure at 75 GPa, and (c and d) the P2₁/c structure at 150 and 500 GPa, respectively. The dashed lines denote the Fermi level, which is set to zero [67].

To investigate the consequence of the unusual increases in the O-O bond length and the ELF value of the $P6_3/mmc$ structure at 11 and 40 GPa, the PDOSs at 5, 8, 11, 14, 38, 39, 40, and 41 GPa were calculated. The results revealed that the valence band energies of Li and O decrease with elevated pressure, while their conduction band energies increase (see Figure 25). However, there are unusual changes in some energies of Li and O as follows. The valence band energies in the s-states of Li at around -4.88 eV shift up by ~0.02 eV from 39 GPa to 40 GPa [Figure 25(d)], and the valence band energies at around -5.89 eV shift up by ~0.01 eV from 39 GPa to 40 GPa [Figure 25(e)]. Similarly, the valence band energies in the s-states of O at around -4.88 eV shift up by ~0.03 eV from 39 GPa to 40 GPa [Figure 25(i)]. Conversely, the conduction band energies in the p-states of O at around 3.16 eV shift down by ~0.002 eV from 8 GPa to 11 GPa, and the energies at around 3.66 eV shift down by ~0.01 eV from 8 GPa to 11 GPa [Figure 25(l)]. Likewise, the energies at around 3.38 eV shift down by ~0.01 eV from 39 GPa to 40 GPa, and the energies at around 3.94 eV shift down by ~0.026 eV from 39 GPa to 40 GPa [Figure 25(r)]. These result in a decrease in the band gap at 11 and 40 GPa.

By considering the change of DOSs in the valence bands of Li and O at 5, 8, 11, 14, 38, 39, 40, and 41 GPa, the results showed the unusual changes in their DOSs as follows. The DOSs in the energies from -3 eV to 0 eV decrease for the s-states of Li and the p-states of O but increase for the s-states of O [Figure 25(a),(c),(f),(h),(k),(m)]. As for the DOSs in the energies from -8 eV to -3 eV, in general, their DOSs for the s-states of Li increase [Figure 25(a),(c)], but their DOSs for the s- and p-states of O decrease [Figure 25(f),(h),(k),(m)]. However, the DOSs for the s-states of Li in the energies at around -5.9 eV decrease in the pressure range of 38-41 GPa [Figure 25(e)], and the DOSs for the s-states of O in the energies at around -4.2 eV increase in the pressure range of 5-14 GPa [Figure 25(g)]. Unusually, the DOSs for the s-states of Li in the energies at around -4.2 eV slightly increase between 8 and 11 GPa [Figure 25(b)]. Regarding the change of DOSs in the conduction bands of Li and O at 5, 8, 11, 14, 38, 39, 40, and 41 GPa, the DOSs for the s-states of Li decrease at around 3 eV but increase at around 4 eV [Figure 25(a),(c)], which are opposite with the changes in their DOSs for the p-states of O [Figure 25(k),(m)]. These suggest that the electrons transfer between the states of Li and O in

the 8-11 GPa and 39-40 GPa pressure range because the increases and decreases in the DOSs between Li and O at the same energy levels are consistent.
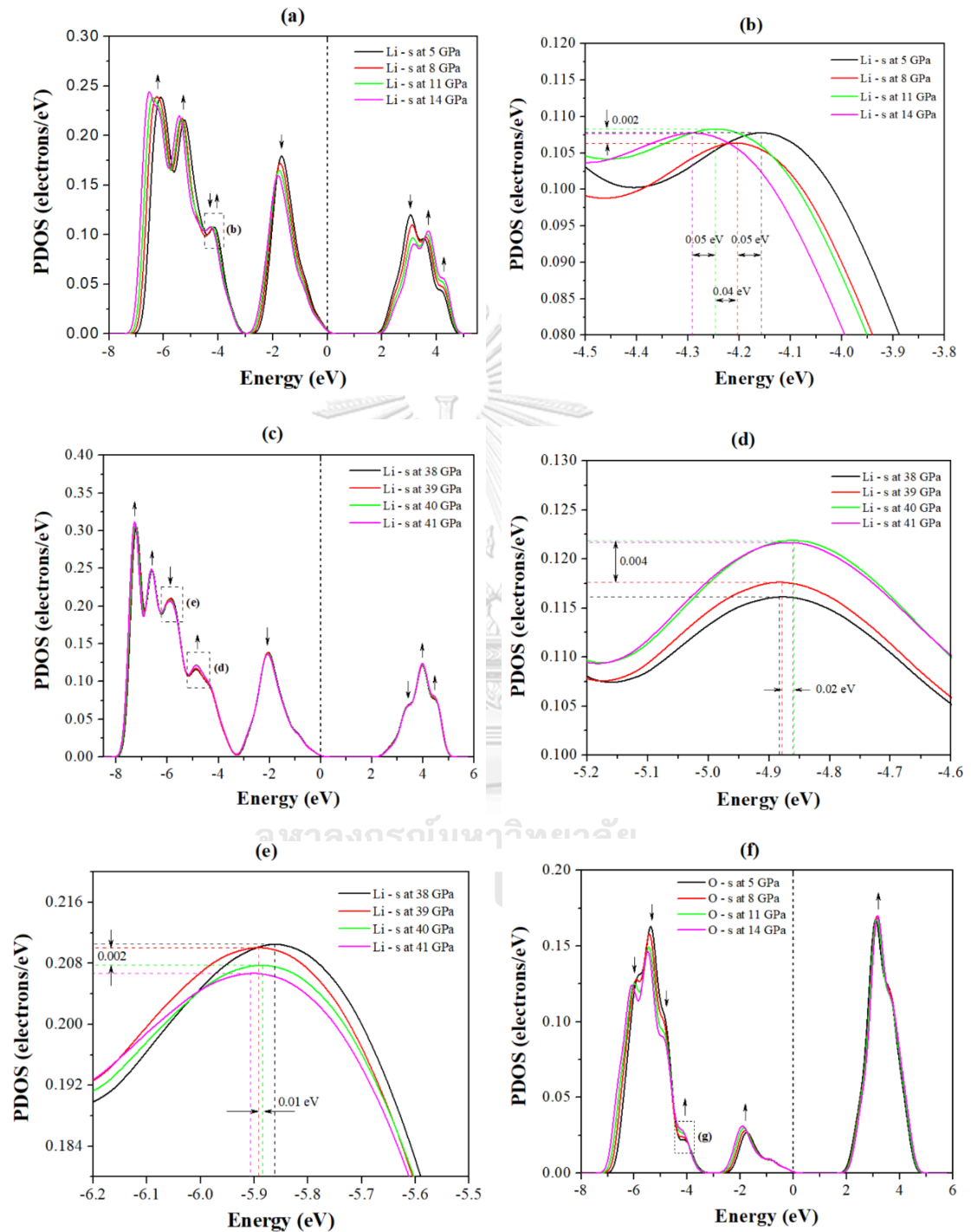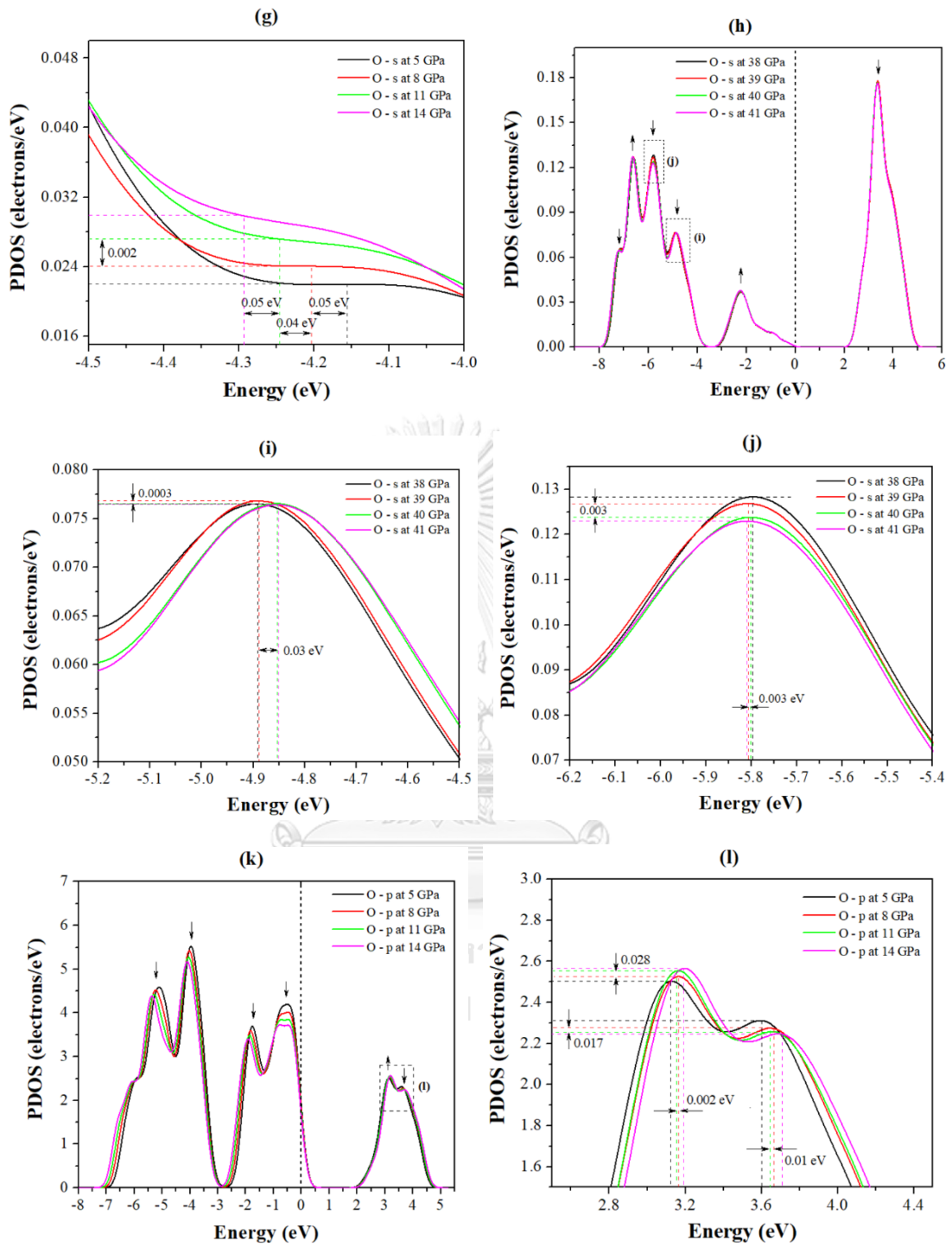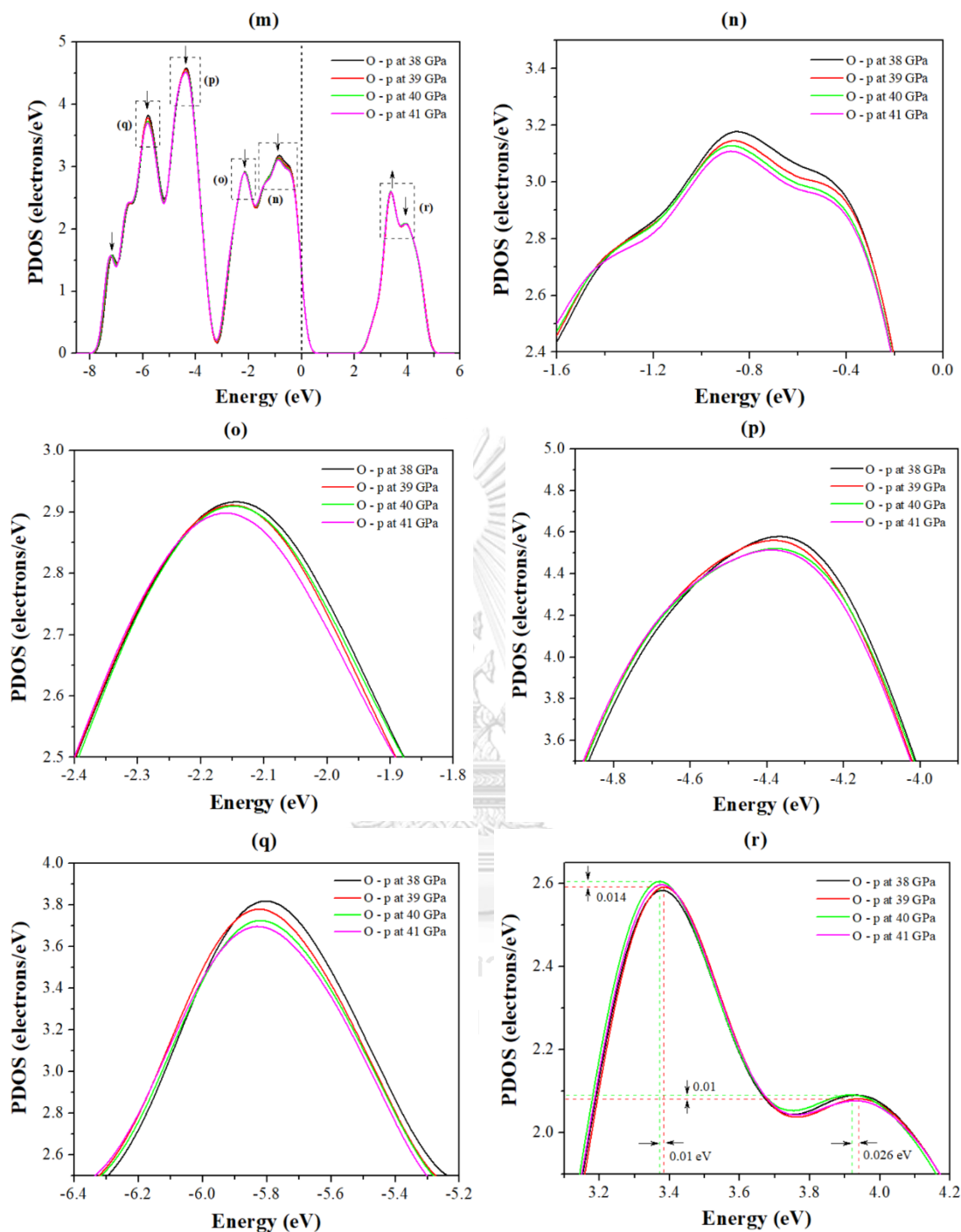
Figure 25: Partial density of states (PDOSs) of Li and O for the P6₃/mmc structure at 5, 8, 11, 14, 38, 39, 40, and 41 GPa: (a)-(e) the s-states of Li, (f)-(j) the s-states of O, and (k)-(r) the p-states of O. The arrows denote the trends of changes with elevated pressure. The vertical dashed lines mark the Fermi level [67].

The σ_p^* antibonding and the π_p^* antibonding states of the O-O bonds in Li_2O_2 are represented by the conduction band and the valence band states with almost no contribution from the Li states [72, 73]. Garcia-Lastra *et al.* [72] found that if an electronic hole is created near the top valence band (π_p^*), then an excess electron is formed in the conduction band (σ_p^*), which leads to large local distortions of the lattice. Furthermore, Kang *et al.* [73] proposed that the presence of an excess electron in the conduction band (σ_p^*) leads to extension and/or breakage of one of the O-O bonds. Based on the present results, the DOSs in the conduction band (σ_p^*) increase at 8-11 and 39-40 GPa. This suggests the softening of the O-O bonds at 11 and 40 GPa.

To analyze the atomic charge in Li_2O_2 under high pressure, the Mulliken population analysis [74, 75] in the 0-500 GPa pressure range was calculated. At ambient pressure, the Mulliken charges of Li(1)-Li(2) were 0.99|e|, 0.77|e| for Li(3)-Li(4) and -0.88|e| for O(1)-O(4), as shown in Table 3. These values are consistent to that reported by Deng *et al.* [16]. Owing to anisotropic structure, the O atom in the O-O bonds is coordinated to six neighboring Li atoms with the distances of 2.1713 Å for O-Li(1)/Li(2) and 1.9962 Å for O-Li(3)/Li(4). Thus, the electrostatic interactions between the O and Li for the O-Li(1)/Li(2) are different from that of the O-Li(3)/Li(4). These imply that the atomic charges on the Li(1) and Li(2) are equivalent, which differs from that of Li(3) and Li(4). Since the oxidation states of Li and O in Li_2O_2 are +1 and -1, the formation of Li_2O_2 likely has anisotropic charge transfers from O to Li as follows: -0.48|e| to Li(1)-Li(4); -0.02|e| to Li(1)-Li(2) and -0.46|e| for Li(3)-Li(4).

With elevated pressure from 0 GPa to 70 GPa, the Mulliken charges of the O(1)-O(4) and Li(1)-Li(2) increase from -0.88|e| to -0.93|e| and from 0.99|e| to 1.10|e|, respectively. On the contrary, the Mulliken charges of the Li(3) and Li(4) decrease from 0.77|e| to 0.75|e|. Furthermore, the O-Li(1)/Li(2) and O-Li(3)/Li(4) distances vary from 2.1713 Å and 1.9962 Å at ambient pressure to 1.8587 Å and 1.7763 Å at 70 GPa, respectively. This exhibits that the electrostatic interactions of O-Li(1)/Li(2) increase rather than the interactions of O-Li(3)/Li(4) with elevated pressure. Therefore, These suggest that pressure causes the change in the electrostatic interactions of the O-Li(1)/Li(2) and O-Li(3)/Li(4), leading to the variation of the Mulliken charges with increasing pressure. However, the charges transfer in the $P2_1$ and $P2_1/c$ structures were not found because

the Mulliken charges of the O and Li atoms are equal, but they vary from 0.90|e| at 75 GPa to 0.95|e| at 500 GPa. This implies that the oxidation state of the O atoms in the high-pressure phases approaches +1, which also confirms the stability of the O-O bonds in Li_2O_2 under pressure up to 500 GPa.

In addition, to visualize the chemical bonds in three phases of Li_2O_2, the electron density maps and the ELF plots of the $P6_3/mmc$, the $P2_1$, and the $P2_1/c$ structures at 0, 75, 150, and 500 GPa were plotted (Figure 26-27). The electron density maps show the O-O and Li-O bonds at different pressures. Likewise, the ELF plots exhibit that electrons are highly localized in the O-O bonds, which confirm that electrons mainly contribute in the p-states of O. Consequently, these confirm the existence of the O-O bonds under pressure up to 500 GPa.

Table 3: Mulliken charges of the Li and O atoms for the $P6_3/mmc$, the $P2_1$, and the $P2_1/c$ structures of Li_2O_2 at different pressures [67].

Pressure (GPa)	Structure	Mulliken charge (e)							
		Li(1)	Li(2)	Li(3)	Li(4)	O(1)	O(2)	O(3)	O(4)
0	$P6_3/mmc$	0.99	0.99	0.77	0.77	-0.88	-0.88	-0.88	-0.88
0[§]	$P6_3/mmc$[§]	0.99	0.99	0.77	0.77	-0.88	-0.88	-0.88	-0.88
4	$P6_3/mmc$	1.00	1.00	0.77	0.77	-0.88	-0.88	-0.88	-0.88
6	$P6_3/mmc$	1.00	1.00	0.77	0.77	-0.88	-0.88	-0.88	-0.88
8	$P6_3/mmc$	1.01	1.01	0.77	0.77	-0.89	-0.89	-0.89	-0.89
10	$P6_3/mmc$	1.01	1.01	0.77	0.77	-0.89	-0.89	-0.89	-0.89
11	$P6_3/mmc$	1.01	1.01	0.77	0.77	-0.89	-0.89	-0.89	-0.89
12	$P6_3/mmc$	1.02	1.02	0.77	0.77	-0.89	-0.89	-0.89	-0.89
15	$P6_3/mmc$	1.02	1.02	0.77	0.77	-0.89	-0.89	-0.89	-0.89
20	$P6_3/mmc$	1.03	1.03	0.77	0.77	-0.90	-0.90	-0.90	-0.90
25	$P6_3/mmc$	1.04	1.04	0.76	0.76	-0.90	-0.90	-0.90	-0.90
30	$P6_3/mmc$	1.05	1.05	0.76	0.76	-0.91	-0.91	-0.91	-0.91
35	$P6_3/mmc$	1.06	1.06	0.76	0.76	-0.91	-0.91	-0.91	-0.91
39	$P6_3/mmc$	1.06	1.06	0.76	0.76	-0.91	-0.91	-0.91	-0.91
40	$P6_3/mmc$	1.06	1.06	0.76	0.76	-0.91	-0.91	-0.91	-0.91
41	$P6_3/mmc$	1.07	1.07	0.76	0.76	-0.91	-0.91	-0.91	-0.91
45	$P6_3/mmc$	1.07	1.07	0.76	0.76	-0.92	-0.92	-0.92	-0.92
50	$P6_3/mmc$	1.08	1.08	0.76	0.76	-0.92	-0.92	-0.92	-0.92
55	$P6_3/mmc$	1.08	1.08	0.76	0.76	-0.92	-0.92	-0.92	-0.92
60	$P6_3/mmc$	1.09	1.09	0.76	0.76	-0.92	-0.92	-0.92	-0.92

Pressure (GPa)	Structure	Mulliken charge (e)							
		Li(1)	Li(2)	Li(3)	Li(4)	O(1)	O(2)	O(3)	O(4)
65	$P6_3/mmc$	1.10	1.10	0.76	0.76	-0.93	-0.93	-0.93	-0.93
70	$P6_3/mmc$	1.10	1.10	0.75	0.75	-0.93	-0.93	-0.93	-0.93
75	$P6_3/mmc$	1.11	1.11	0.75	0.75	-0.93	-0.93	-0.93	-0.93
75	$P2_1$	0.90	0.90	0.90	0.90	-0.90	-0.90	-0.90	-0.90
135	$P2_1$	0.92	0.92	0.92	0.92	-0.92	-0.92	-0.92	-0.92
136	$P2_1/c$	0.92	0.92	0.92	0.92	-0.92	-0.92	-0.92	-0.92
150	$P2_1/c$	0.92	0.92	0.92	0.92	-0.92	-0.92	-0.92	-0.92
300	$P2_1/c$	0.94	0.94	0.94	0.94	-0.94	-0.94	-0.94	-0.94
500	$P2_1/c$	0.95	0.95	0.95	0.95	-0.95	-0.95	-0.95	-0.95

§ Reference [16]
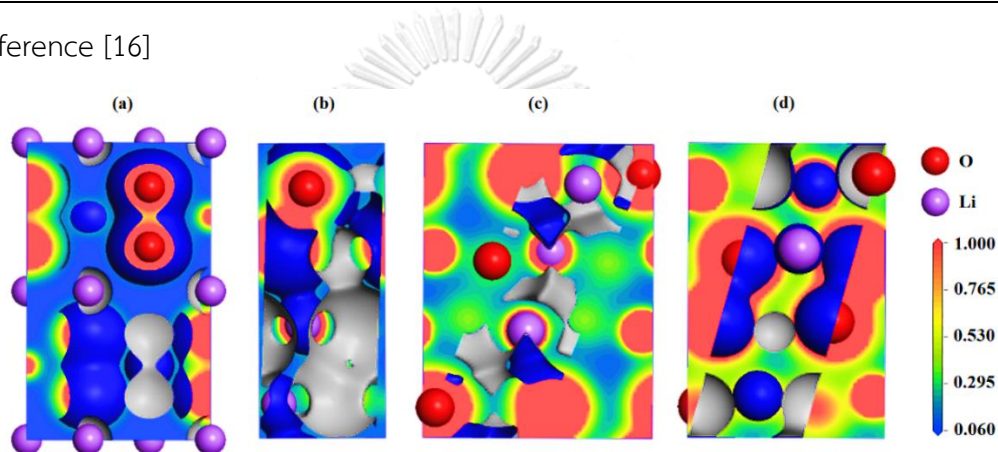
Figure 26: Electron density maps for three structures of Li$_2$O$_2$ projected onto (020) plane of: (a) the P6$_3$/mmc structure at 0 GPa, (b) the P2$_1$ structure at 75 GPa, (c)-(d) the P2$_1$/c structure at 150 and 500 GPa, respectively. The electron density isosurface values of 0.200 for (a, b, c) and 1.412 for (d) [67].
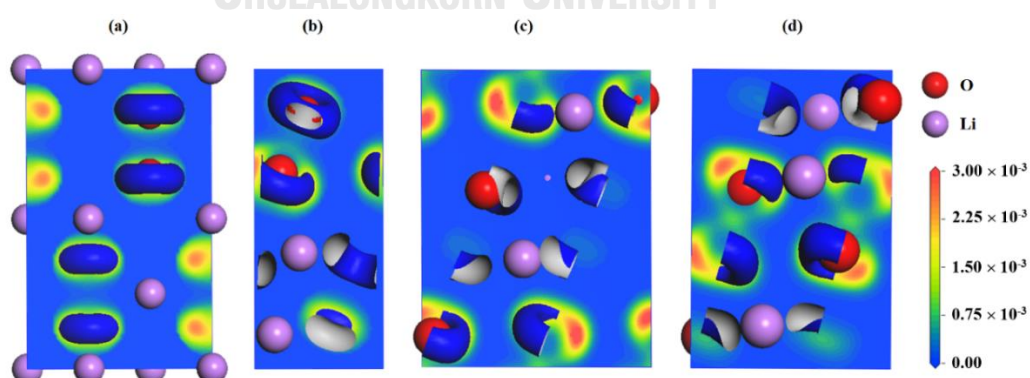
Figure 27: ELFs Plots for three structures of Li$_2$O$_2$ projected onto (020) plane of: (a) the P6$_3$/mmc structure at 0 GPa, (b) the P2$_1$ structure at 75 GPa, (c)-(d) the P2$_1$/c structure at 150 and 500 GPa, respectively. The ELF isosurface values of 0.001 for (a) and 0.002 for (b, c, d) [67].

4.2 The structural phase transitions, the elastic, the vibrational, and the electronic properties of Na_2O_2 under high pressure

4.2.1 The structural phase transitions and phase stabilities of Na_2O_2

4.2.1.1 The high-pressure structural phase transitions of Na_2O_2 at 0 K.
The AIRSS structure search results for Na_2O_2 revealed that the two stable structures at 0, 10, and 20 GPa are the hexagonal *P-62m* structure (3 f.u./cell) and the orthorhombic *Amm2* structure (6 f.u./cell) with a small enthalpy difference of 2 meV/f.u. [Figure 28(a),(b)]. Since the *P-62m* structure can be fully relaxed to be the *Amm2* structure, the *Amm2* structure is a slightly distorted structure of the *P-62m* structure, which is consistent with the slight difference between both simulated X-ray diffraction (XRD) patterns [Figure 29(a)]. Furthermore, the monoclinic $P2_1/c$ structure (2 f.u./cell) and the orthorhombic *Pbam* structure (2 f.u./cell) were also found at 30 GPa [Figure 28(c),(d)], which has a slight enthalpy difference. However, their XRD patterns are significantly different [Figure 29(b)]. Furthermore, the $P2_1/c$ structure is dynamically stable at 30 GPa but unstable at 40 GPa, whereas the *Pbam* structure is dynamically stable in the 30-300 GPa pressure range (Figure 30). The *Pbam* structure is similar to the structure proposed by Deng *et al*. [16], when the cell is shifted to (0, 0, 1/2).
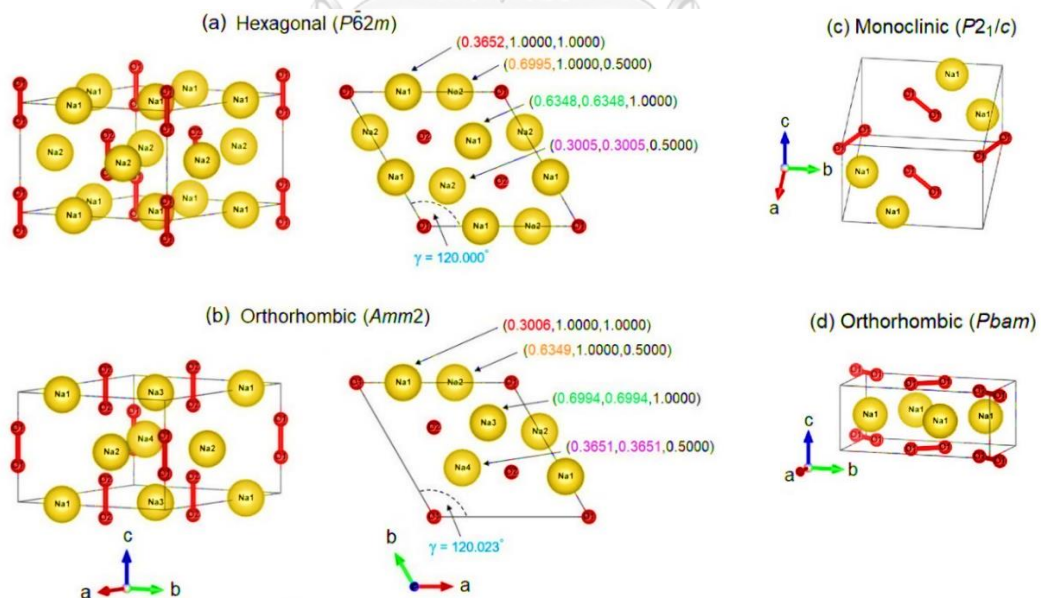
Figure 28: Four crystal structures: (a and b) the P-62m and the primitive Amm2 structures at ambient pressure viewed along two directions. The mapping of atomic positions for the Na atoms marked by the same color. (c) the $P2_1/c$ structure at 22 GPa, and (d) the Pbam structure at 28 GPa [76].
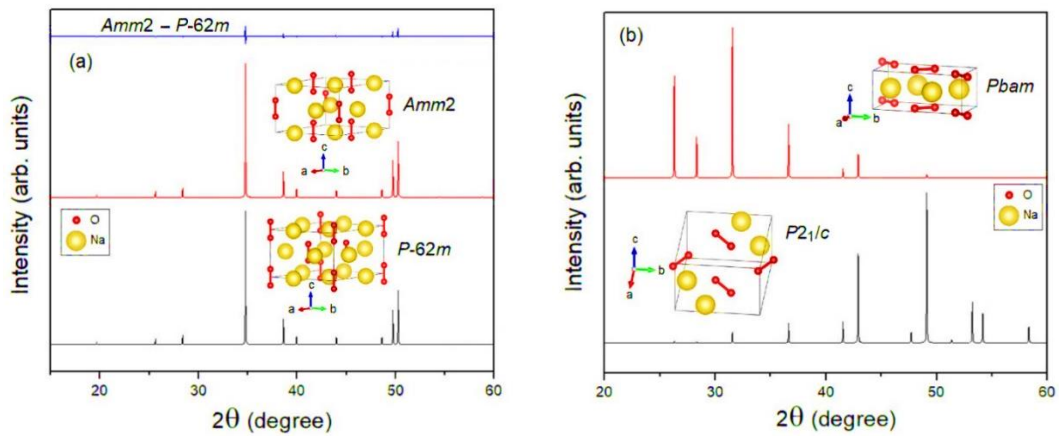
Figure 29: Simulated XRD patterns: (a) the Amm2 and P-62m structures at ambient pressure and their intensity difference, (b) the $P2_1/c$ and Pbam structures at 22 GPa [76].
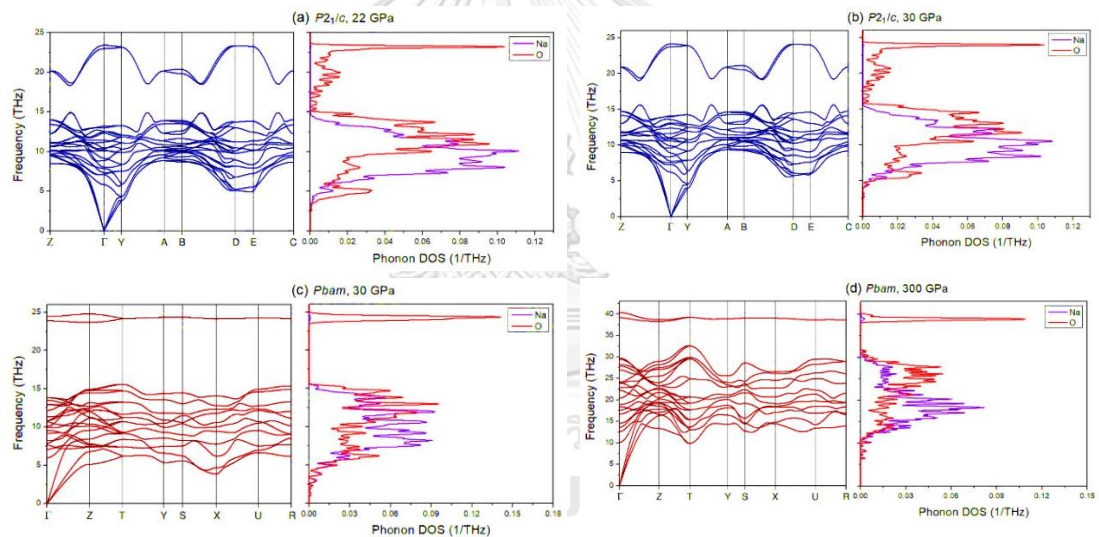
Figure 30: Phonon dispersion curves and their phonon density of states for: (a) the $P2_1/c$ structure at 22 GPa, (b) the $P2_1/c$ structure at 30 GPa, (c) the Pbam structure at 30 GPa, and (d) the Pbam structure at 300 GPa [76].

In addition, the AIRSS results at ambient pressure also revealed that the crystal structures that provide the simulated XRD patterns resemble the XRD patterns calculated from the experimental results of Tallman *et al*. [20]. That is, the *I*4/*mmm* structure is compared to the Na_2O_2-II at 550°C (Figure 31), and the other structures consisting of the *C*2/*m*, the *Pmmm*, and the *Immm* structures are similar to the Na_2O_2-Q at room temperature (Figure 32). Here, the enthalpy of the *I*4/*mmm* structure is

higher than the *P-62m* structure by 0.560 eV/f.u., whereas the enthalpy of the *C2/m*, the *Pmmm*, and the *Immm* structures are higher than the *P-62m* structure by 0.018, 0.019, and 0.021 eV/f.u., respectively. With elevated pressure at 0-22 GPa, the enthalpies of these structures increase with respect to the *P-62m* structure, and their trends of enthalpy in the 22-100 GPa pressure range also increase with respect to the $P2_1/c$ and the *Pbam* structures (Figure 33). This implies that these structures become more energetically unstable with increasing pressure. Thus, below the melting point of 948 K, the *I4/mmm* structure may be a candidate for the Na_2O_2-II phase, while the *C2/m*, the *Pmmm*, and the *Immm* structures may be candidates for the Na_2O_2-Q phase. Usually, the symmetry of the crystal structure is increased by increasing temperature. Therefore, the *Immm* structure likely becomes stable at high temperature because its symmetry is higher than the other structures.
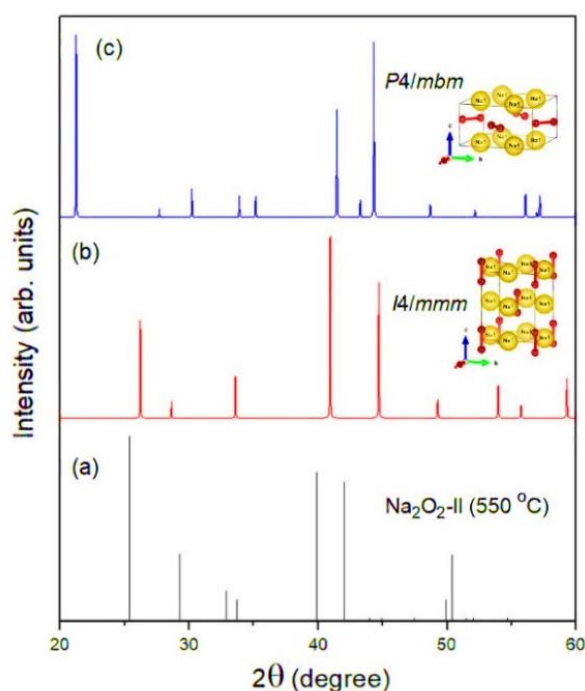
Figure 31: Simulated XRD patterns of the crystal structures: (a) Na₂O₂-II at 550 ℃ and ambient pressure calculated from the Tallman's experimental data [20], and (b)-(c) are the I4/mmm and the P4/mbm structures at 0 K and ambient pressure obtained from the AIRSS searches [76].
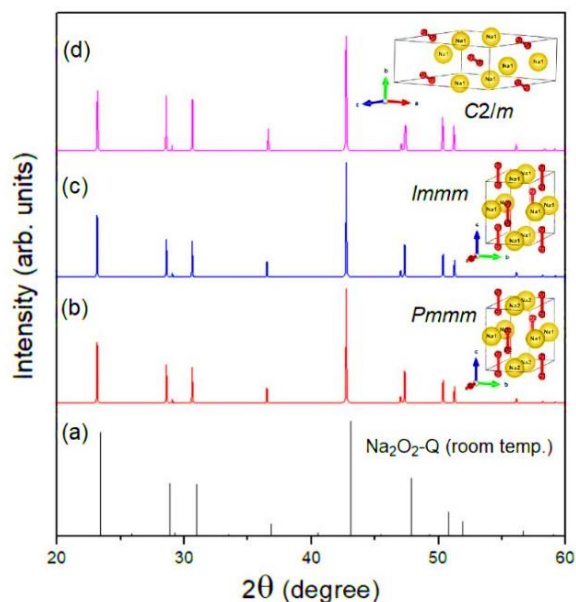
Figure 32: Simulated XRD patterns of the crystal structures: (a) Na_2O_2-Q at room temperature and ambient pressure calculated from the Tallman's experimental data [20], and (b)-(d) are the Pmmm, the Immm, and the C2/m structures at 0 K and ambient pressure obtained from the AIRSS searches, respectively [76].
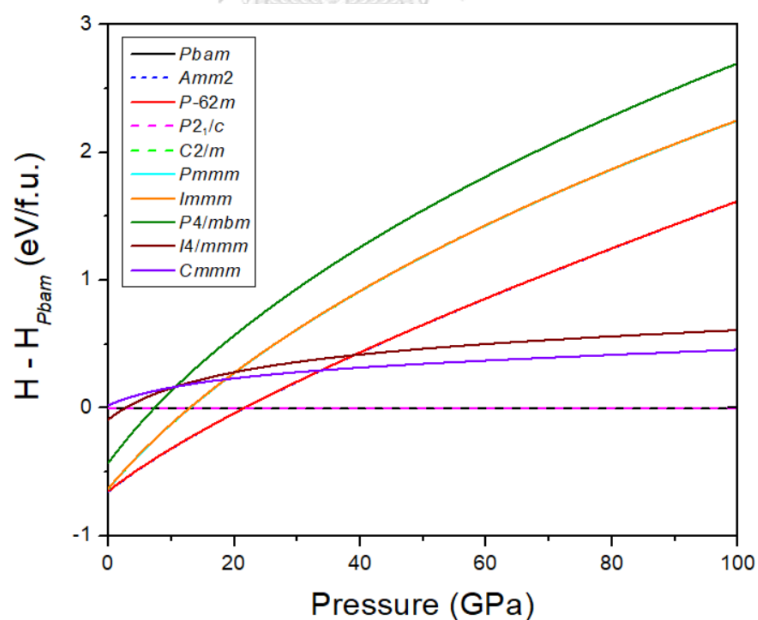
Figure 33: Relative enthalpies of the various structures that obtained from the AIRSS searches with respect to the Pbam structure in the 0-100 GPa pressure range were obtained from the E-V curves fitting using the third-order Birch-Murnaghan equations of states [76].

After geometry optimization, the results showed that the energy of the *Amm*2 structure at 0 GPa is lower than the *P-62m* structure by 2.1 and 0.4 meV/f.u., which is calculated by the GGA-PBE and LDA functionals, respectively. Even though these energies are very small differences, they are significant within the energy tolerance of the calculations. Here, the PBE functional was selected to identify the difference between the *Amm*2 and the *P-62m* structures. Moreover, the optimized lattice parameters of the *P-62m* structure correspond to the previous studies [8, 18]: a = b = 6.282 Å, c = 4.511 Å, and γ = 120.000°. The optimized lattice parameters of the primitive *Amm*2 structure were of a = b = 6.284 Å, c = 4.510 Å, and γ = 120.023°, which exhibits a small difference of the lattice parameters from the *P-62m* structure (Figure 28). These lattice parameters suggest that the *Amm*2 structure is distorted from the *P-62m* structure. Furthermore, by comparing the 2 × 2 × 2 supercell of the primitive *Amm*2 and the *P-62m* structures, there are angle differences in the same hexagonal Na layer. For the *P-62m* structure, the angles in the hexagonal Na layer of are 60.000°, 55.031°, 60.000°, 55.031°, 60.000°, and 69.938° marked by θ_1, θ_2, θ_3, θ_4, θ_5, and θ_6, respectively [Figure 34(a)]. These suggest that the *P-62m* structure has a distorted close-packed Na layer. Nevertheless, the angles are slightly different from that of the *Amm*2 structure. The angles (θ_1 - θ_6) of the *Amm*2 structure are 59.995°, 55.060°, 60.003°, 55.059°, 60.003°, and 69.881°, respectively [Figure 34(b)]. With increasing pressure, these angles have three trends of change consisting of an increase of θ_6, a decrease of θ_2 and θ_4, and an approximate constant of θ_1, θ_3, and θ_5. This implies that the primitive *Amm*2 structure is a more distorted close-packed Na layer than the *P-62m* structure, which is in agreement with a small difference between the *Amm*2 and the *P-62m* structures. Nevertheless, this difference leads to a significant difference in their phonon dispersions and their electronic band structures, which will be further discussed. Therefore, it is likely that the crystal structure of Na_2O_2 at very low temperature favors the lower symmetry (*Amm*2, No. 38) rather than the higher symmetry (*P-62m*, No. 189).

To verify the difference between the primitive *Amm*2 and the *P-62m* structures, the phonon dispersion and the partial phonon density of states were calculated at ambient pressure (Figure 35). At the Γ point, the phonon frequencies for the *Amm*2 structure are ~23.3 and ~23.5 THz, which are higher than that of the *P-62m* structure about 5

and 4 cm^{-1}, respectively, whereas the highest frequency for both structures is indifferent. Since these phonon frequencies relate to the O-O stretching modes, they imply that the O-O bonds in the *Amm*2 structure at ambient pressure are stronger than that of the *P-62m* structure.
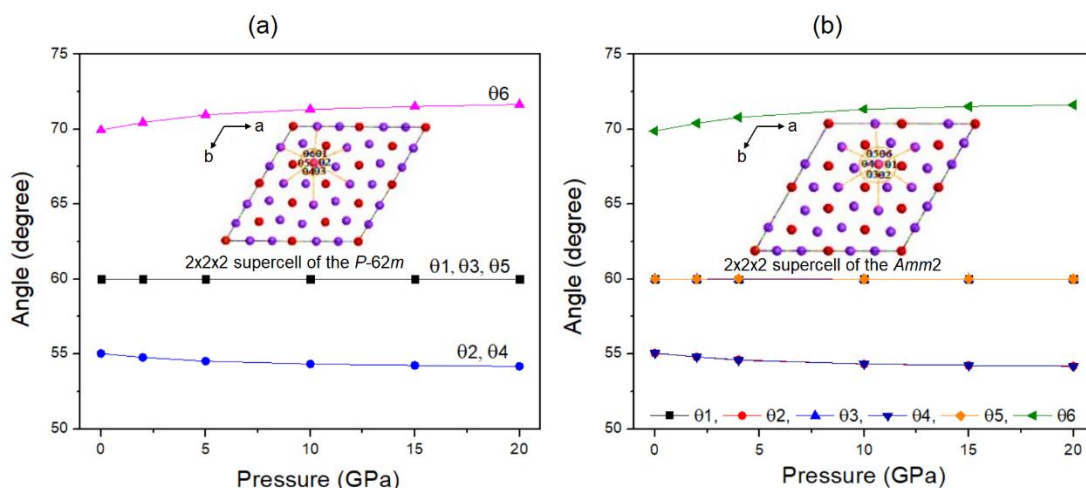
Figure 34: Plot of the angles in the same hexagonal Na layer of the 2×2×2 supercell versus pressure from 0 to 20 GPa for: (a) the P-62m structure and (b) the primitive Amm2 structure [76].
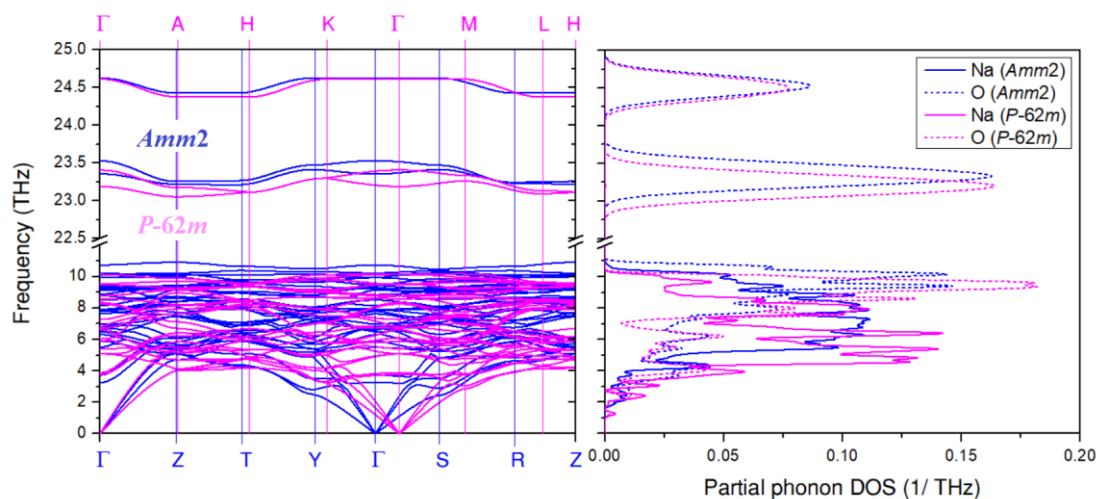
Figure 35: The overlay plot of the phonon dispersion curves for the primitive Amm2 and the P-62m structures and their overlay plot of the partial phonon density of states. The blue and magenta lines denote the primitive Amm2 and the P-62m structures, respectively [76].

In addition, the phonon frequencies of the *Amm*2 structure below 5 THz at the Γ, Y, and S points are lower than that of the *P*-62*m* structure at the Γ, K, and M points, respectively. However, both structures are dynamically stable because there is no imaginary phonon frequency. Since there are several different phonon frequencies between both structures, this may lead to the difference in Helmholtz free energies at elevated temperatures. Therefore, the thermodynamic stability of the *Amm*2 and the *P*-62*m* structures would be further verified to find the most stable structure under pressure and temperature.

To verify the phase stability of Na_2O_2 at high pressures, the formation enthalpies of Na_2O_2, Na_2O, and NaO_2 at 0, 10, 20, 30, and 50 GPa were calculated using the formula:

$$\Delta H_f = \left[H(Na_xO_y) - xH(Na) - y(H(O)] / (x+y) \right], \tag{4.1}$$

where $H(Na_xO_y)$ stands for the enthalpy of the selected compound, whereas $H(Na)$ and $H(O)$ denote the enthalpy of Na and solid O, respectively. The results revealed that Na_2O_2 is more stable than decomposition into Na and O_2 with increasing pressure [Figure 36(a)]. Likewise, the $Na_2O + O$, $NaO_2 + Na$, and $(2/3)Na_2O + (2/3)NaO_2$ are higher in enthalpies than Na_2O_2 at the same pressures, and they are more different with increasing pressure [Figure 36(b)]. These imply that Na_2O_2 is stable against decompositions.
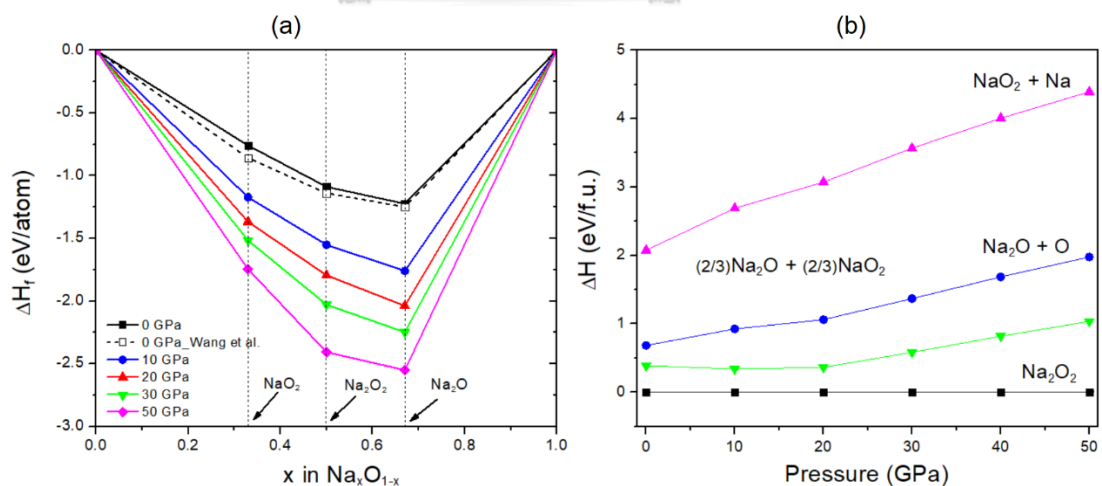
Figure 36: (a) Predicted formation enthalpies of Na₂O₂, Na₂O, and NaO₂ at different pressures compared with decomposition into Na and O₂. The data points are connected by the dashed and solid lines denote the convex hull. The opened square represents the results predicted by Wang et al. [77]. The structural data of Na₂O,

NaO₂, Na, and solid O₂ for the calculations were retrieved from the previous studies [78-82]. (b) Relative enthalpies of the decompositions compared with Na₂O₂ in the 0-50 GPa pressure range [76].

To determine the structural phase transitions in Na_2O_2 at high pressures, the relative enthalpy between the *Amm*2, the *P*2₁/*c*, the *P-62m*, and the *Pbam* structures *versus* pressure were plotted, as shown in Figure 37. The results exhibited that the *Amm*2 structure is lower in enthalpy than the *P-62m* structure by 2 meV/f.u. at 0 GPa and 1.6 meV/f.u. at 20 GPa. The *Amm*2 structure is higher in enthalpy than the *P*2₁/*c* structure at 22-28 GPa, whereas the *Pbam* structure has a lower enthalpy at 28 GPa (Figure 37). Furthermore, the *P*2₁/*c* structure at 22 GPa and the *Pbam* structure at 28 GPa are dynamically stable [Figure 30(a)-(c)]. Thus, the *Amm*2 structure likely transforms into the *P*2₁/*c* structure at 22 GPa, and the *P*2₁/*c* structure transforms to the *Pbam* structure at 28 GPa. Here, the structural phase transition at 28 GPa is the same as proposed by Deng *et al*. [16]. By considering the energy (Δ*E*), the enthalpy (Δ*H*), and the work done (Δ*PV*) of the *Amm*2 structure compared with the *P-62m* structure *versus* pressure (Figure 38), all Δ*E* and Δ*H* of the *Amm*2 structure are lower than that of the *P-62m* structure, while their Δ*PV* values are higher. This implies that the Δ*PV* is a driving force for the structural phase transition of the *Amm*2 structure.
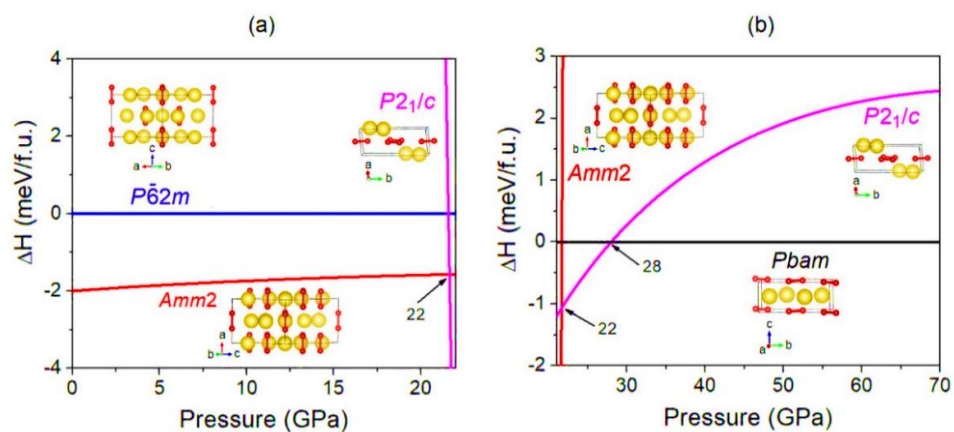
Figure 37: (a) Enthalpy differences (ΔH) for the Amm2 and the P2₁/c structures compared to the P-62m structure versus pressure at 0-22 GPa and (b) Enthalpy differences (ΔH) for the Amm2 and the P2₁/c structures compared to the Pbam structure versus pressure at 22-70 GPa. Large and small spheres in crystal structures denote the Na and O atoms, respectively [76].
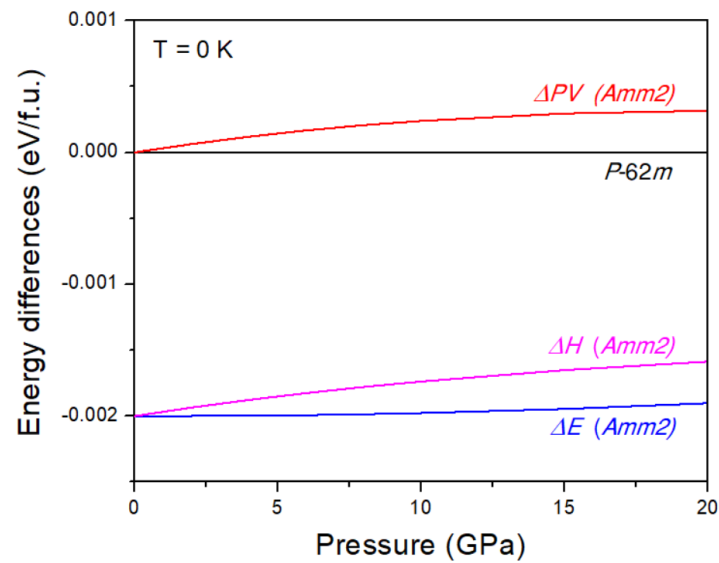
Figure 38: Plots of the differences in total energy (ΔE), enthalpy (ΔH), and work done (ΔPV) of the Amm2 structure compared to that of the P-62m structure versus pressure at 0-20 GPa [76].

To identify the driving force for the structural phase transitions, the changing of lattice constants and volume in the *Amm*2, the *P*2$_1$/*c*, and the *Pbam* structures at high pressures were analyzed (Figure 39). At the transition pressure of 22 GPa, the 'b' and 'c' lattice constants, and volume (*V*) of the *P*2$_1$/*c* structure were collapsed at γ = 141.583° by ~31.4, ~37.1, and ~10.0% compared to the *Amm*2 structure, respectively. However, the 'a' lattice constant was extended by ~11.8%, which suggests that the driving force at 22 GPa significantly affects the bc-plane. At the transition pressure of 28 GPa, the 'a', 'b', 'c' lattice constants in the *Pbam* structure were collapsed by ~21.8, ~0.0, and ~20.4% compared to the *P*2$_1$/*c* structure at γ = 141.483°, respectively. Since there was no collapse in the b-axis and volume, the a-axis was collapsed rather than the c-axis, resulting in the new alignment of the O-O bonds on the (001) plane of the *Pbam* structure [Figure 40(d)].
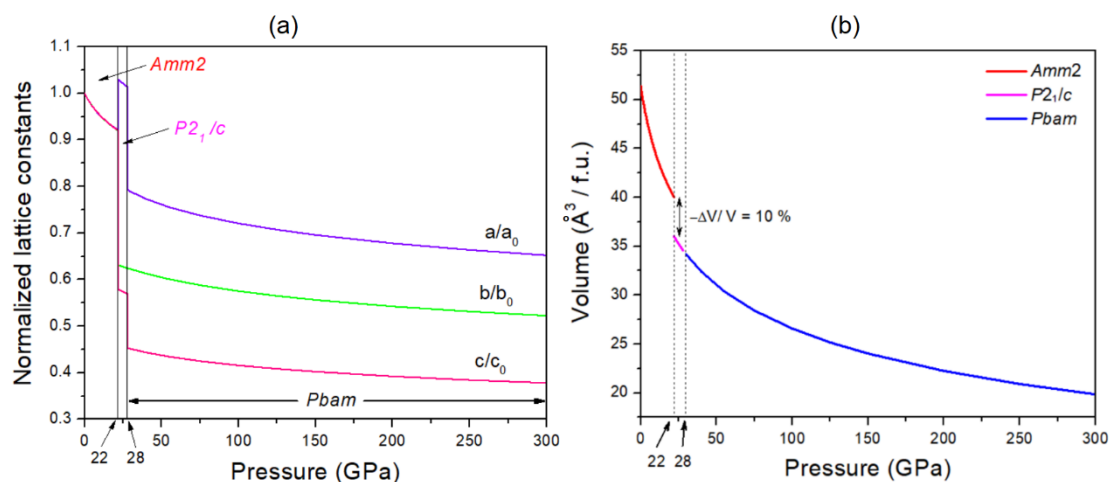
Figure 39: (a) Plots of the normalized lattice constants versus pressure at 0-300 GPa. The a_0, b_0, and c_0 stand for the lattice constants of the Amm2 structure at 0 GPa. (b) The volume change of three structures of Na_2O_2 at 0-300 GPa: the Amm2, the $P2_1/c$, and the Pbam structures [76].

By observing the alignment of the O-O bonds in four phases of Na_2O_2 at high pressures (Figure 40), the O-O bonds in the *Amm2* structure were aligned in parallel with the [100] direction, while they were aligned in parallel with the [001] direction of the *P-62m* structure. For the $P2_1/c$ structure at 22 GPa, the O-O bonds were tilted with an angle of ~24° compared to the ab-plane and deviated from the [100] direction by ~39°. For the *Pbam* structure at 28 GPa, the O-O bonds were aligned on the (001) plane but deviated from the [100] direction by ~52. Furthermore, the alignment of the O-O bonds at 300 GPa was indifferent from those at 28 GPa. Consequently, these suggest that the alignment of the O-O bonds in four phases of Na_2O_2 under high pressure are different, which may relate to their thermodynamic stability.
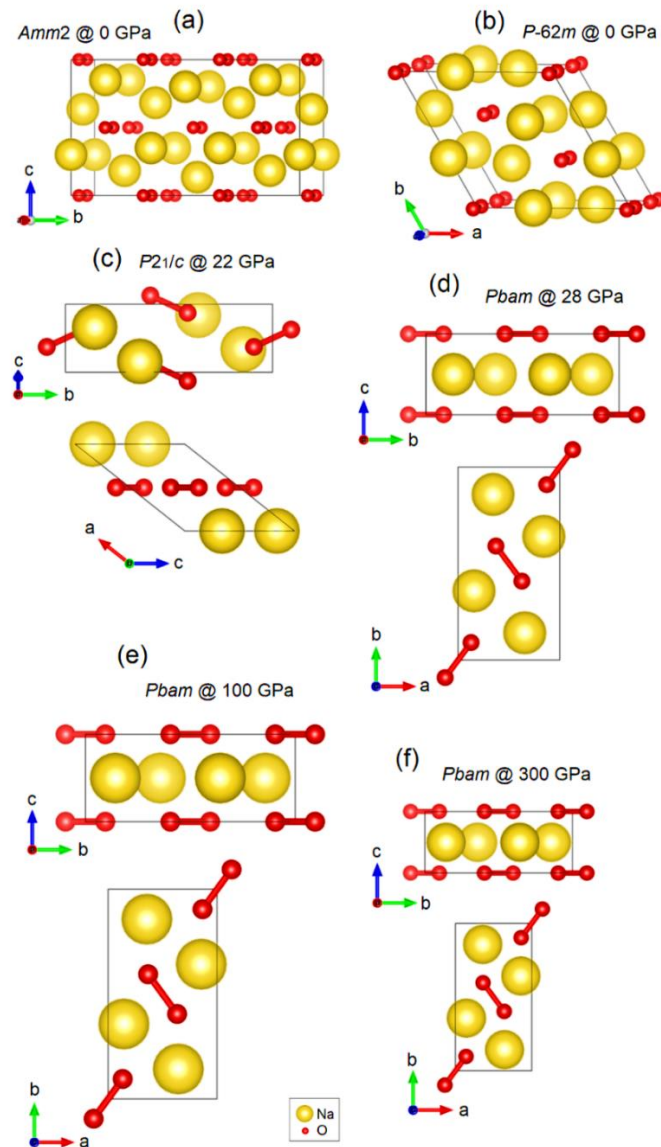
Figure 40: The alignment of the O-O bonds in 4 phases of Na₂O₂: (a) the Amm2 structure at 0 GPa, (b) the P-62m structure at 0 GPa, (c) the P2₁/c structure at 22 GPa, (d) the Pbam structure at 28 GPa, (e) the Pbam structure at 100 GPa, and (f) the Pbam structure at 300 GPa [76].

4.2.1.2 The phase stabilities of Na₂O₂ at high pressures and temperatures. To verify the thermodynamic stability for the *Amm*2, the *P*-62*m*, the *P*2₁/*c*, and the *Pbam* phases of Na₂O₂, their Gibbs free energies at elevated pressure up to 300 GPa and temperature up to 600 K were calculated based on the quasi-harmonic

approximation. The results revealed that the Gibbs free energies decrease with elevated temperature but increase with increasing pressure (Figure 41).
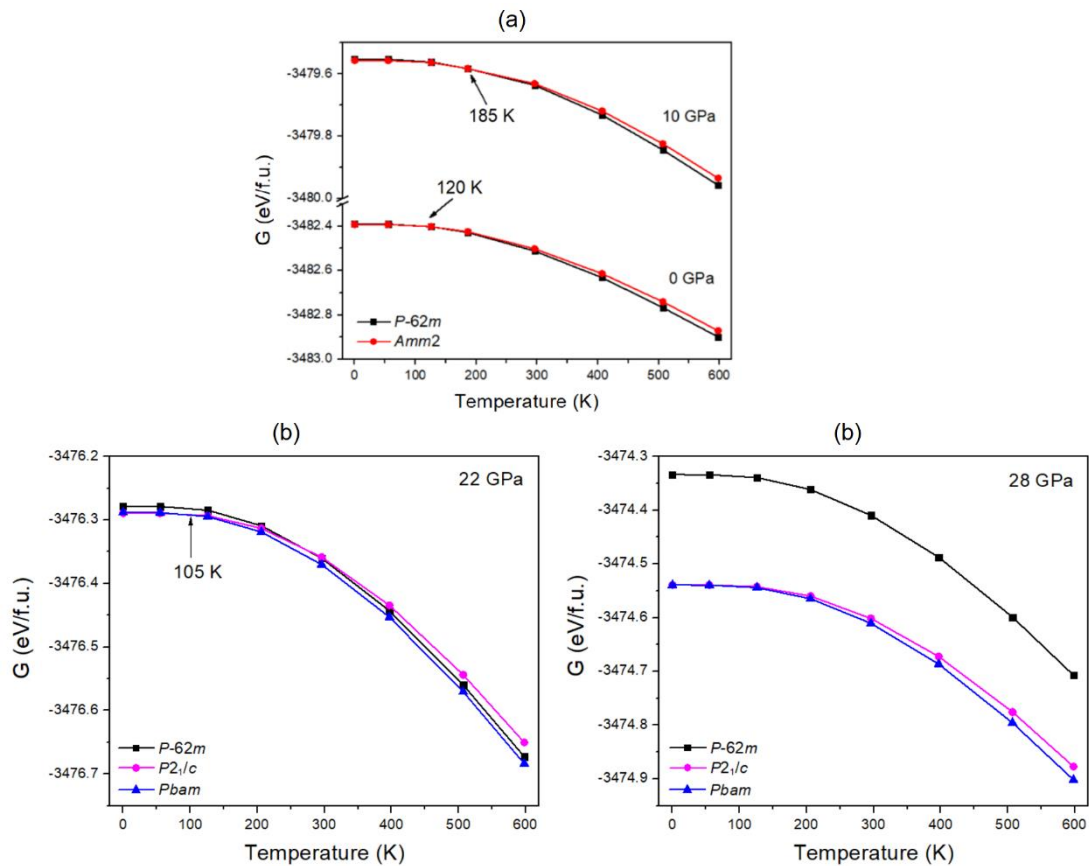
Figure 41: Plots of Gibbs free energy (G) versus temperature at 0-600 K for the predicted phases of Na$_2$O$_2$ at different pressures: (a) 0, 10 GPa, (b) 22 GPa, and (c) 28 GPa [76].

Furthermore, the Gibbs free energies of the *Amm*2 structure compared to the *P-62m* structure at 0, 5, 10, 15, and 20 GPa are higher than the *P-62m* structure at the transition temperatures around 120, 125, 185, 200, and 75 K, respectively [Figure 42(a)]. These suggest that the *P-62m* structure is more stable than the *Amm*2 structure above the transition temperatures. That is, the *P-62m* structure is thermodynamically stable at ambient conditions, but the *Amm*2 structure is not. In the same way, the free energy of the *P*2$_1$/*c* structure at 22 GPa and below 105 K is lower than the other structures, whereas the *Pbam* structure becomes the lowest free energy in the 105-600 K temperature range [Figure 41(b)]. Besides, the *Pbam* structure at 28 GPa is stable in the

0-600 K temperature range [Figure 41(c)]. Based on these results, the predicted P-T phase diagram of Na_2O_2 was generated, as shown in Figure 42(b).
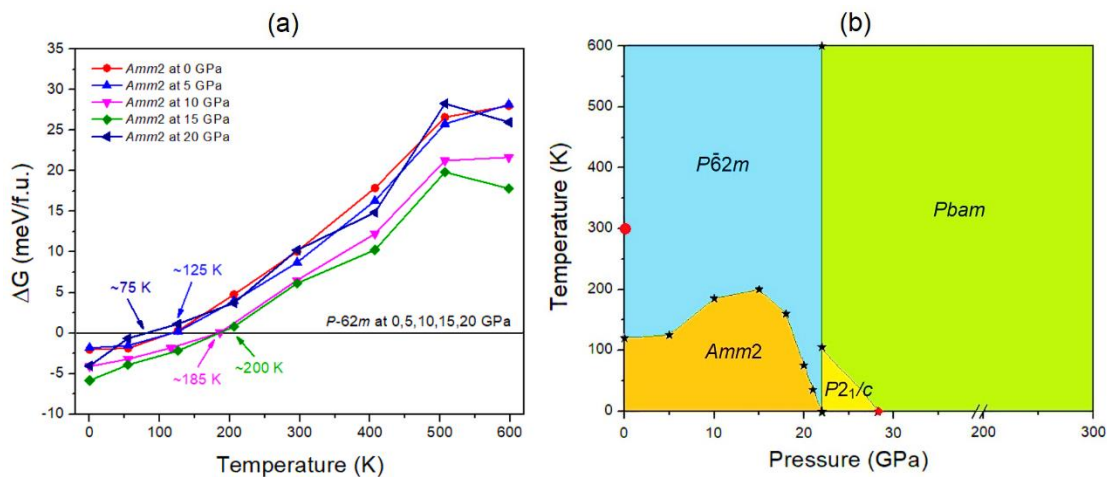
Figure 42: Gibbs free energy of the Amm2 structure compared with the P-62m structure at 0, 5, 10, 15, and 20 GPa and 0-600 K. (b) The predicted P-T phase diagram of Na_2O_2 at 0-300 GPa and with elevated temperatures up to 600 K [76]. The red circle represents the P-62m structure at ambient conditions established by Föppl [8] and Tallman et al. [18]. The red diamond denotes the Pbam structure predicted by Deng et al. [16].

Regarding the *P-62m* structure, Even though the *P-62m* structures that were obtained from the AIRSS searches and the relaxed Tallman's/Föppl's structures are consistent, there was a small sign about the atomic displacement of the Na1 and Na2 between Tallman's and Föppl's structures at room temperature (Figure 43). However, the difference in the atomic displacement was small, while it was revealed by comparing their XRD patterns. Especially, the intensity of the (100) peak for the Tallman's structure is higher than that of the Föppl's structure by ~2% (Figure 44). This implies that the Tallman's and the Föppl's structures that were observed at room temperature are slightly different, which may be significant at high temperatures.

WP		Atom	Atomic Displacements			
			u_x	u_y	u_z	$|u|$
3f	(x,0,0)	Na2	0.0020	0.0000	0.0000	0.0124	← no difference
2e	(0,0,z)	O1	0.0000	0.0000	0.0010	0.0045
3g	(x,0,1/2)	Na1	-0.0190	0.0000	0.0000	0.1182	← significant difference
4h	(1/3,2/3,z)	O2	0.0000	0.0000	-0.0010	0.0045

NOTE: u_x, u_y and u_z are given in relative units. $|u|$ is the absolute distance given in Å

Available from: http://www.cryst.ehu.es/cgi-bin/cryst/programs/nph-compstru

Figure 43: Comparison of the atomic displacement between the Tallman's and the Föppl's structures [76] using the COMPSTRU program [69].
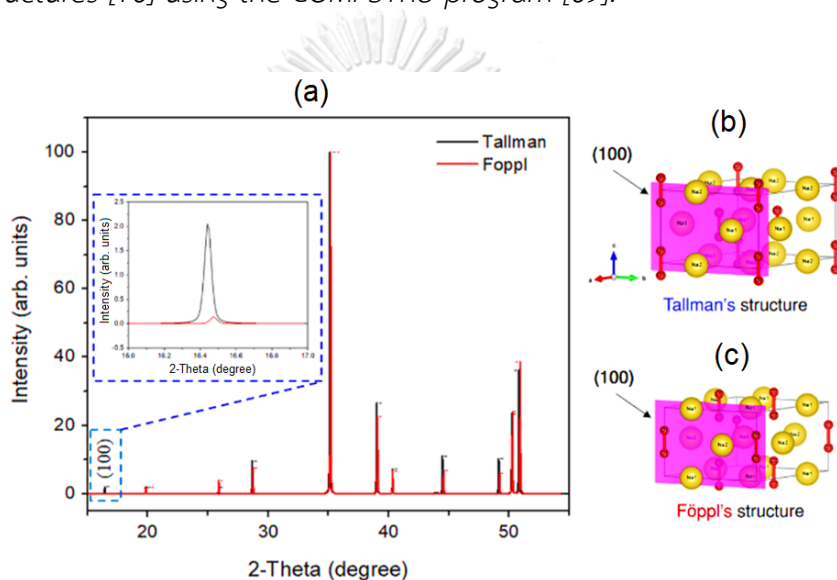
Figure 44: (a) The simulated XRD pattern for the Tallman's and the Föppl's structures, (b)-(c) the (100) plane of the Tallman's and Föppl's structures [76].

To identify the most stable *P-62m* structure at elevated temperatures, the Gibbs free energy for the relaxed Tallman's and Föppl's structures at ambient pressure were calculated as a function of temperature up to 600 K. The results revealed that the free energy of the Tallman's structure and the Föppl's structure is not different in the 0-45 K temperature range, while the Tallman's structure becomes lower in free energy than the Föppl's structure by ~1.7 meV/f.u. at 300 K and ~4 meV/f.u. at 550 K (Figure 45). This point of view suggests that the Tallman's structure favors temperature rather than the Föppl's structure. Nevertheless, the free energy differences are slight and are beyond experimental resolution. Thus, Tallman's and Föppl's structures could be considered to be similar.
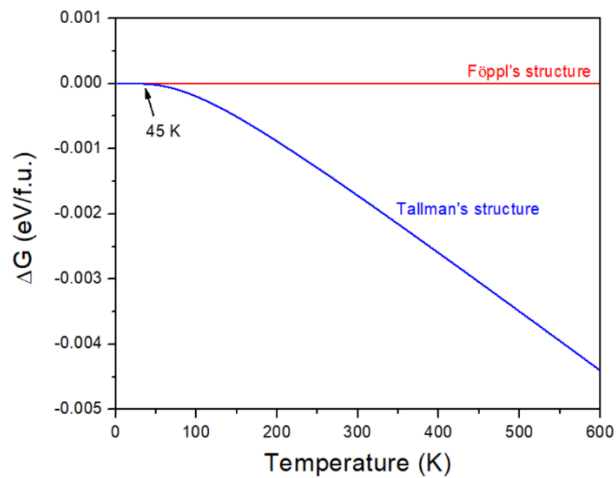
Figure 45: Gibbs free energy difference (ΔG) of the Tallman's structure with respect to the Föppl's structure as a function of temperature at ambient pressure [76].

4.2.2 The elastic behavior at high pressures

To verify the mechanical stability of the *Amm*2 and the *P*-62*m* structure and to analyze the difference in elastic properties of them at high pressures, the elastic constants, elastic moduli, and the elastic anisotropy of the *Amm*2 and the *P*-62*m* structures were calculated using the PBE functional [28]. The results showed that the elastic stiffness of the *Amm*2 and the *P*-62*m* structures satisfy their elastic stability conditions in Eq. (2.47) and Eq. (2.49). This suggests that the *Amm*2 and the *P*-62*m* structures are mechanically stable. Furthermore, their elastic stiffnesses revealed that there are slight differences between the *P*-62*m* and the *Amm*2 structures at 0-15 GPa (Figure 46). In general, the elastic stiffnesses increase with increasing pressure. However, B_{44} of the *Amm*2 structure and the $(B_{11}-B_{12})/2$ term of the *P*-62*m* structure have decreasing trends with increasing pressure. This results in the elastic instability in the *P*-62*m* structure when B_{12} surpasses B_{11}, the so-called tetragonal shear instability [83]. Similarly, the *Amm*2 structure has shear instability if B_{44} is equal to zero. Based on a linear approximation, the elastic instability of both structures was found at around 35 GPa, which is higher than the predicted transition pressure at 22 GPa. Nonetheless, the occurring of elastic instability at a higher pressure than the predicted transition pressure was also found in other ionic compounds such as MgO and CaO [83]. It was interpreted that the presence of the activation barrier along the phase transformation path results in the inconsistent transition pressure. Dramatically, B_{11} of the *Amm*2 structure and B_{33}

of the *P-62m* structure unusually stiffen at 2 GPa and then soften at 3 GPa, which are consistent with the discontinuous decrease of the interatomic distances of O1-O1 and O2-O2 at 3 GPa [Figure 47(a)]. In addition, B_{22}, B_{23}, and B_{44} of the *Amm*2 structure at 9 GPa slightly soften like B_{12} and B_{33} of the *P-62m* structure. This implies that the *Amm*2 structure is more elastic deformation than the *P-62m* structure, which results in thermodynamic instability at elevated temperatures.
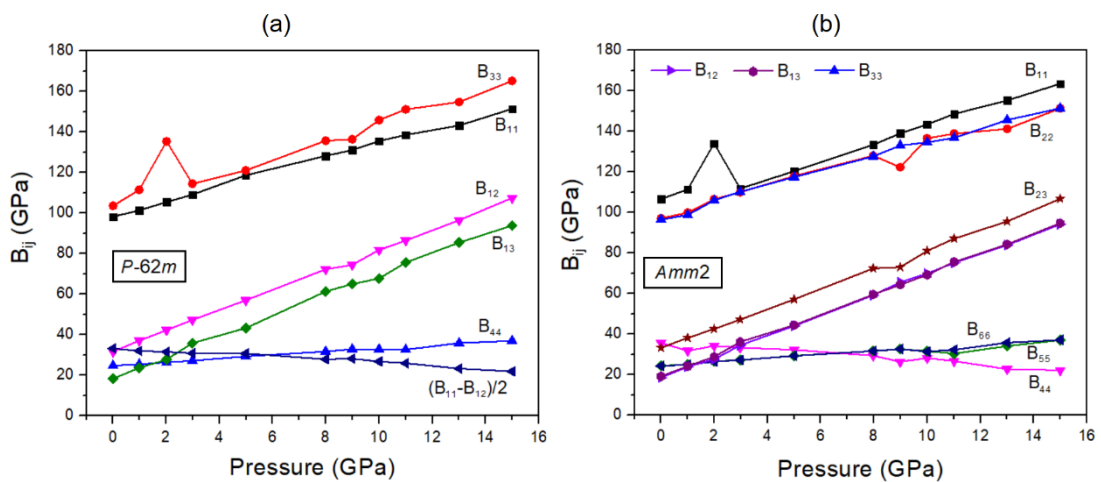
Figure 46: The elastic stiffnesses (B_{ij}) of two crystal structures at 0-15 GPa: (a) the P-62m structure and (b) the Amm2 structure [76].

To quantify the elastic anisotropy of the *Amm*2 and the *P-62m* structures under high pressure, the universal elastic anisotropy index (A^U) of both structures was calculated using Eq. (3.1). The results revealed that A^U of the *Amm*2 and the *P-62m* structures at ambient pressure are 0.28 and 0.24 (Figure 47), which are slightly different. Here, A^U of 0.22 of the *P-62m* structure is the same as the previous work proposed by Jong et al. [84]. With elevated pressure, A^U of both structures decreases until 8 GPa and then increases at ~9 GPa. Furthermore, A^U significantly increases at 2 GPa yet strongly decreases at 3 GPa, which corresponds to the change in the elastic stiffnesses at 2 and 3 GPa. Usually, a higher value of A^U indicates the increase in the elastic anisotropy, so the structure is a locally isotropic crystal when A^U is equal to zero [53]. Therefore, the results suggest that pressure induces the change of elastic anisotropy in the *Amm*2 and the *P-62m* structures of Na_2O_2, and their A^U values are likely a locally isotropic

crystal with A^U of 0.03 at 9 GPa. This is similar to other hexagonal crystals (e.g., Ru, a-Hf, and a-Gd) [53].
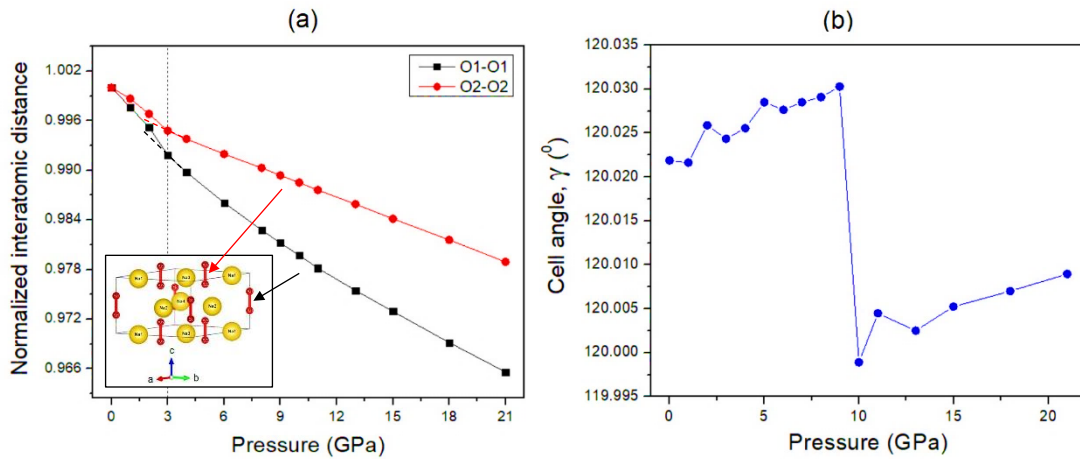
Figure 47: (a) Plots of the normalized interatomic distances of O-O in the Amm2 structure versus pressure. (b) Plot of the cell angle (γ) in the primitive Amm2 structure versus pressure at 0-21 GPa [76].

The calculated bulk and shear moduli for the *Amm*2 and the *P*-62*m* structures at ambient pressure are shown in Table 4. Their bulk and shear moduli at ambient pressure are slightly different. Usually, the elastic moduli calculated by the LDA functional overestimate, while they calculated by the GGA functional underestimate [85]. For this reason, the results suggest that the measured bulk (*K*) and shear moduli (*G*) at ambient pressure should be: *K* = 49.15-64.55 GPa and *G* = 30.49-39.29 GPa for the *Amm*2 structure, and *K* = 48.95-64.73 GPa and *G* = 29.01-37.88 GPa for the *P*-62*m* structure. By Comparing the bulk moduli (B_0) obtained from the third-order Birch-Murnaghan equations of states, B_0 of the *Amm*2 and the *P*-62*m* structures are 49.25 and 49.26 GPa, respectively. Besides, the B_0 of 49 GPa is in agreement with the previous studies [84] obtained from the elastic constants calculations and 56.40 GPa [86] obtained from the third-order Birch-Murnaghan equations of states.
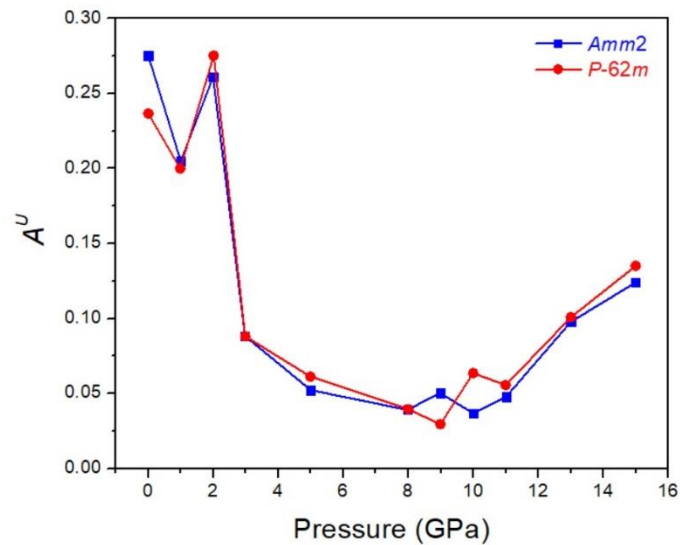
Figure 48: Plot of the universal elastic anisotropy index (A^U) for the P-62m and the Amm2 structures versus pressure at 0-15 GPa [76].

Using the PBE functional with a single-point energy calculation, the results revealed that the calculated bulk and shear moduli are 55.82 GPa and 31.14 GPa for the *P-62m* structure proposed by Tallman *et al*. [18], and 57.16 GPa and 32.11 GPa for the *P-62m* structure proposed by Föppl [8] respectively. This suggests the small difference within the upper and lower bounds on the bulk and shear moduli for the *P-62m* structure. Consequently, the elastic properties of the Tallman's and Föppl's structures at room temperature are slightly different.

Table 4: The calculated bulk and shear moduli of the Amm2 and the P-62m structures at ambient pressure [76].

Structure	Condition	Bulk modulus (GPa)		Shear modulus (GPa)	
		GGA-PBE	LDA	GGA-PBE	LDA
Amm2		49.16	64.53	31.33	38.98
P-62m		48.95	64.72	29.88	37.59
P-62m [85]	0 GPa, 0 K	56.40	-	-	-
P-62m [83]		49	-	29	-
P-62m ¶		55.82	40.19	31.14	27.92
P-62m §	ambient	57.16	41.37	32.11	29.08

¶ using the structural data proposed by Tallman *et al*. [18]

§ using the structural data proposed by Föppl [8]

4.2.3 The vibrational properties of Na_2O_2 at high pressures

Even though the *Amm*2 and *P*-62*m* structures were slightly different, there was a small difference in their vibrational properties as introduced before. Using the group theory analysis of eigenvectors, the results showed that the vibrational modes of the *Amm*2 structure at the Γ point are B_1, B_2, A_1, and A_2 modes with 36 frequencies. The phonon acoustic modes are $\Gamma_{act} = B_1 + B_2 + A_1$, whereas the phonon optical modes are $\Gamma_{opt} = 9B_1 + 8B_2 + 10A_1 + 6A_2$. As for the *P*-62*m* structure, the vibrational modes are A_2'', E', A_1'', A_1', A_2', and E'' modes with 36 frequencies as well. The phonon acoustic modes are $\Gamma_{act} = A_2'' + 2E'$, while the phonon optical modes are $\Gamma_{opt} = 3A_2'' + 12E' + A_1'' + 4A_1' + 3A_2' + 10E''$. Moreover, there were the differences in phonon frequencies in each mode and activity in the IR and Raman spectra between the *Amm*2 and the *P*-62*m* structures at ambient pressure, as are shown in Table 5. The results revealed that all phonon frequencies in the optical modes of the *Amm*2 structure at the Γ point are Raman active, whereas some of the phonon frequencies in the optical modes of the *P*-62*m* structure are Raman active, consisting of E', A_1', and E'' modes. Likewise, the optical modes of A_2'' and E' for the *P*-62*m* structure are IR active, while all phonon frequencies in the optical modes for the *Amm*2 structure are almost IR active, except the A_2 mode. Thus, these suggest that it is possible to observe the *Amm*2 structure using IR and Raman spectroscopies at temperatures below 120 K. Moreover, Table 5 also provides the phonon frequencies in each vibrational mode, IR and Raman active modes for the *P*2$_1$/*c* structure at 22 GPa and the *Pbam* structure at 30 GPa, which may be useful for experimental identifying the structural phase transitions in Na_2O_2 at those pressures.

To analyze the consequence of the elastic stiffness stiffening at 2 GPa and softening at 3 and 9 GPa on phonon frequencies of the *Amm*2 structure, the phonon dispersion curves and their phonon DOSs at 1, 2, 3, and 4 GPa and at 8, 9, 10, and 11 GPa were calculated (Figure 49). Furthermore, the phonon frequencies shifts from those of 0 GPa *versus* pressure at the Γ and Y points in the 0-15 GPa pressure range, were also plotted (Figure 50).

Table 5: The vibrational modes, activities in the IR and Raman spectra for the P-62m and the Amm2 structures at 0 GPa, the P2₁/c structure at 22 GPa, and the Pbam structure at 30 GPa [76].

Structure	Vibrational mode	Frequency (cm^{-1})	Activity	Structure	Vibrational mode	Frequency (cm^{-1})	Activity
P-62m at 0 GPa	A″$_2$	129.3, 195.0, 292.3	IR	Amm2 at 0 GPa	B$_1$	223.4, 232.7, 260.4, 263.6, 271.8, 305.1, 314.5, 340.8, 779.1	IR / Raman
	E′	169.6, 203.4, 224.9, 286.4, 316.3, 338.0	IR / Raman		B$_2$	124.4, 183.2, 216.3, 219.7, 283.8, 294.0, 331.3, 337.2	IR / Raman
	A″$_1$	125.5	-		A$_1$	225.0, 227.9, 254.8, 261.4, 295.3, 310.9, 317.7, 331.4, 784.9, 821.5	IR / Raman
	A′$_1$	169.6, 278.8, 780.8, 821.0	Raman		A$_2$	108.2, 196.7, 210.9, 262.2, 307.5, 358.0	Raman
	A′$_2$	180.8, 275.5, 773.5	-		B$_{1u}$	405.9	IR
	E″	221.8, 226.5, 242.5, 293.2, 318.4	Raman		B$_{2u}$	262.5, 318.7, 449.9	IR
					B$_{3u}$	305.9, 332.1, 432.6	IR
					A$_u$	199.3, 359.7	-
P2₁/c at 22 GPa	A$_u$	194.9, 237.2, 295.1, 341.9, 418.5	IR	Pbam at 30 GPa	B$_{2g}$	236.2, 361.1	Raman
					B$_{3g}$	255.8, 336.8	Raman
	B$_u$	262.3, 305.3, 380.5, 415.3	IR		A$_g$	274.1, 378.0, 461.3, 815.3	Raman
	A$_g$	237.2, 268.2, 345.8, 372.8, 433.3, 780.8	Raman		B$_{1g}$	357.6, 431.6, 461.9, 797.2	Raman
	B$_g$	244.4, 337.4, 348.7, 412.6, 440.0, 766.6	Raman				

Usually, the phonon frequencies in a crystal structure increase with elevated pressure because of the stiffening of chemical bonds. Nevertheless, the results revealed that three phonon frequencies (ω_1, ω_2, and ω_3) of the acoustic modes below 4 THz clearly decrease at 3 GPa around the Y and S points [Figure 49(a),(b)]. The softening of these frequencies also appears in their phonon DOSs below 4 THz. In the same way, the two lowest of the optical phonon frequencies (ω_4 and ω_5) around 4 THz at the Γ point obviously decrease at 3 GPa [Figure 49(a), 50(a)]. Nonetheless, Even though there was no unusual change in the three highest phonon frequencies (ω_{34}, ω_{35}, and ω_{36}) of the optical modes at those pressures, the increase of frequency from 2 to 3 GPa was more than that from 1 to 2 GPa and 3 to 4 GPa, and similar to the increasing of frequency from 9 to 10 GPa. In addition, there was an unusual decreasing in the interatomic distances of the O1-O1 and the O2-O2 at 3 GPa [Figure 47(a)]. The phonon DOSs of the ω_{34} and/or the ω_{35} significantly decrease at 2 GPa [Figure 49(a)].
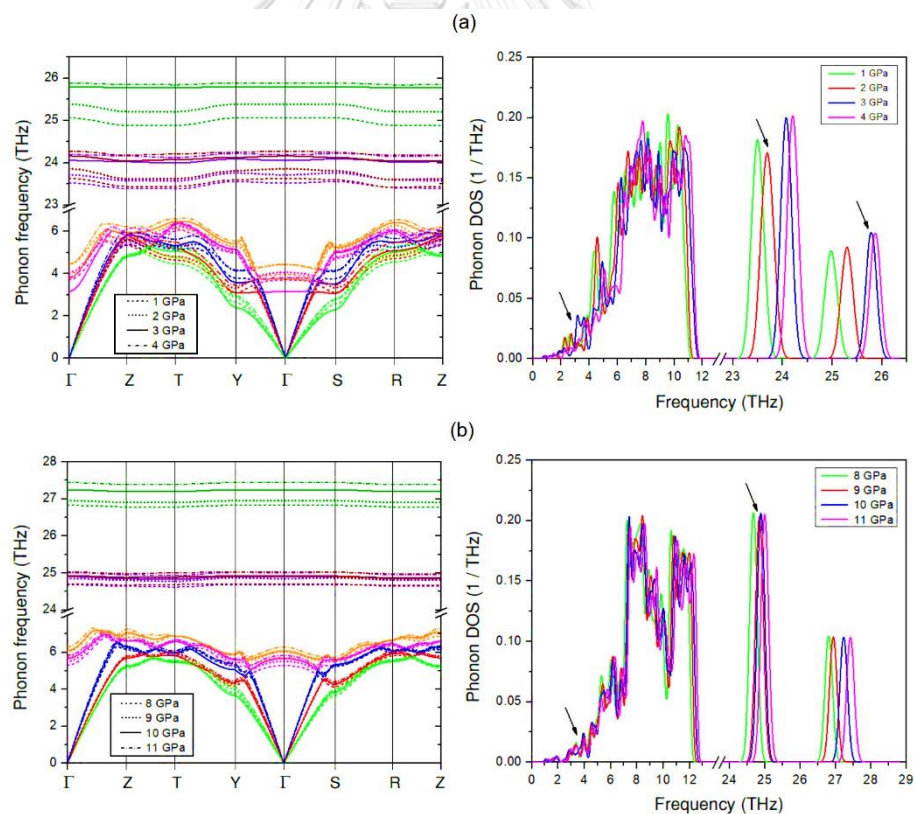
Figure 49: Phonon dispersion curves and their phonon DOSs of the Amm2 structure at different pressures: (a) at 1, 2, 3, and 4 GPa and (b) at 8, 9, 10, and 11 GPa. The phonon frequency modes in the phonon dispersion curves were distinguished by different colors [76].

This relates to the increase of the elastic stiffness B_{11} at 2 GPa. Similarly, the ω_1 and ω_3 below 5 THz at 10 GPa decrease around the Y point [Figure 49(b), 50(b)]. Moreover, the phonons softening at 3 and 10 GPa significantly result in the decreasing of the phonon free energies as well (Figure 51). The results revealed that this effect decreases with increasing temperature. Thus, it is now possible to note that pressure induces the decreasing of the elastic stiffnesses and the phonons softening, leading to the decreasing of phonon free energies at 3 and 10 GPa.
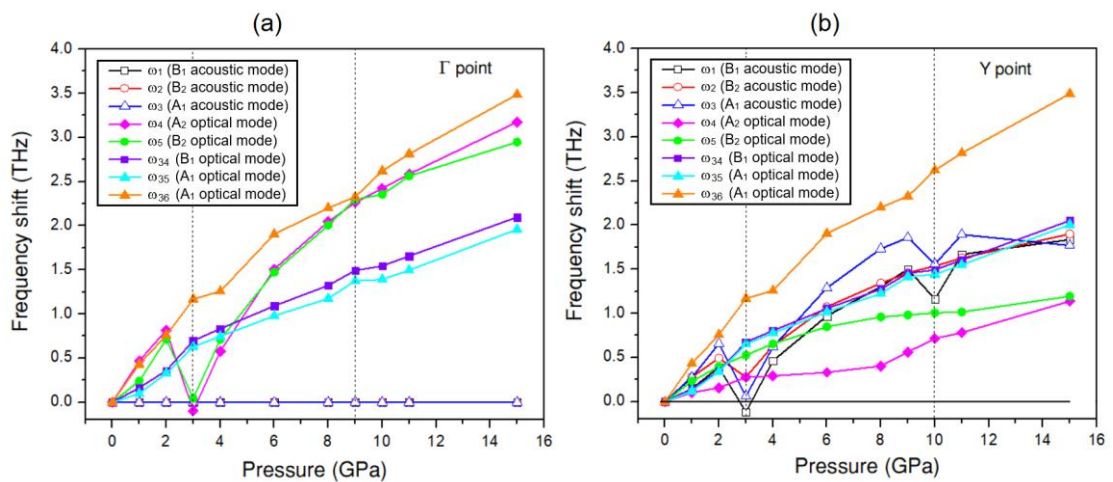
Figure 50: The selected phonon frequencies shifts versus pressure at 0-15 GPa for three frequencies of the acoustic modes and five frequencies of the optical modes at different k-points of the Amm2 structure: (a) at the Γ point and (b) at the Y points [76].
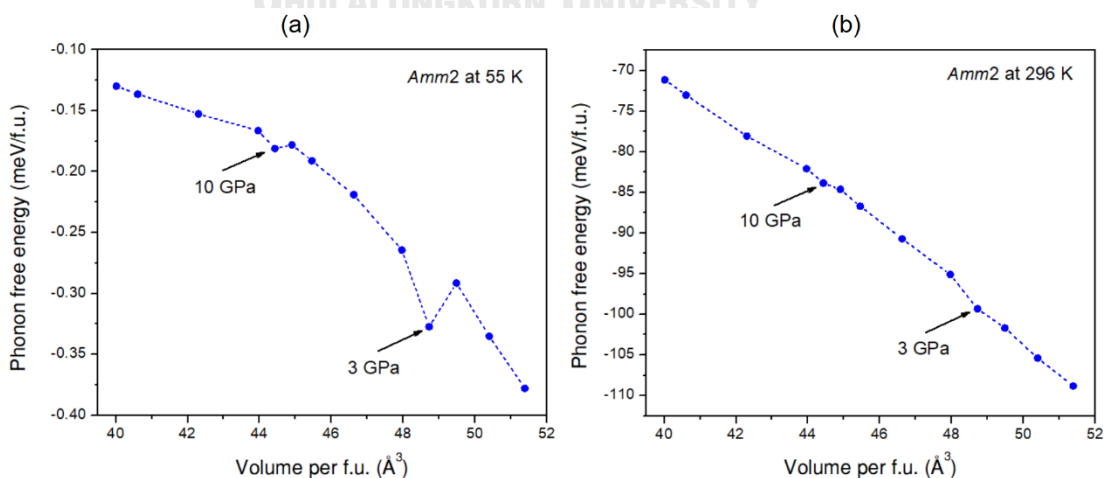
Figure 51: Plot of the phonon free energy versus volume for the Amm2 structure at the different temperatures: (a) 55 K and (b) 296 K [76].

4.2.4 The electronic properties and the chemical bonds of Na_2O_2 at high pressures

To determine the electronic properties of Na_2O_2 at high pressures, the electronic band structures and the partial density of states (PDOSs) for the *Amm2,* the *P-62m,* the *P2$_1$/c,* and the *Pbam* structures were calculated using the PBE and HSE06 functionals (Figure 52). The results showed that the difference in the band structures between the *Amm2* and the *P-62m* structures appears at the T/H points around -0.5 and -3.5 eV, at the Y/K points around -0.7 and -4.5 eV, and at the Z/H point around -0.4, -1.0, -3.3, and -4.0 eV (*Amm2/P-62m*). Moreover, the results revealed that the *Amm2* and the *P-62m* structures are indirect bandgaps with the same value of 1.79 eV, whereas the *P2$_1$/c* and the *Pbam* structures are direct bandgaps. Nevertheless, the HSE06 functional, which yields a more reliable bandgap than the PBE functional predicted, that the bandgap of the *Amm2* structure is slightly higher than that of the *P-62m* structure by 2 meV. Furthermore, the PBE band gap of the *P-62m* structure corresponds to the previous work with a value of 1.76 eV [87]. With increasing pressure, the PBE and HSE06 band gaps of all structures increase with the same trends (Figure 53). Nevertheless, the HSE06 band gap of the *P2$_1$/c* structure at 22 GPa is higher than the *Pbam* structure by ~13 meV, which identifies a difference between both structures.

Regarding the PDOSs of Na and O in the *Amm2,* the *P-62m,* the *P2$_1$/c,* and the *Pbam* structures (Figure 52), they exhibited that all valence and conduction bands mainly contribute form the p-states of O and slightly contribute from the p-states of Na, the s-states of Na, and the s-states of O. In addition, the overlap of orbitals support the presence of the σ-bonds in these phases of Na_2O_2.
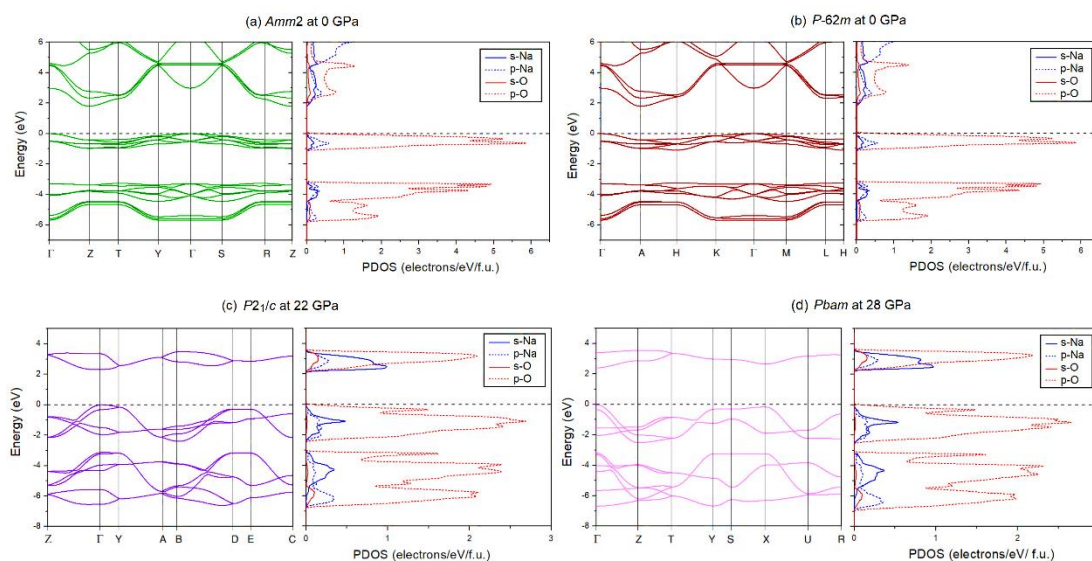
Figure 52: The electronic band structures and their PDOSs at different pressures for: (a) the Amm2 structure at 0 GPa, (b) the P-62m structure at 0 GPa, (c) the P2$_1$/c structure at 22 GPa, and (d) the Pbam structure at 28 GPa [76].
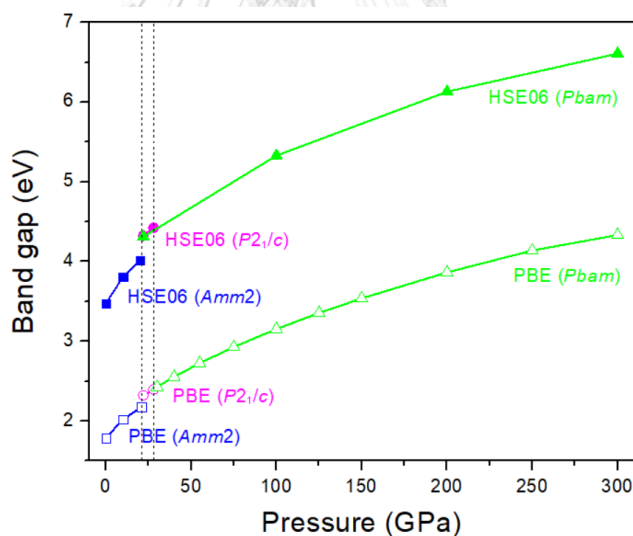
Figure 53: The PBE and HSE06 band gaps versus pressure at 0-300 GPa for the Amm2, the P2$_1$/c, and the Pbam structures [76].

To analyze the behavior of the O-O bonds in the *Amm*2 structure of Na$_2$O$_2$ under high pressure, their ELF values in the 0-21 GPa pressure range were calculated (Figure 54). The results revealed that the ELF value decreases with increasing pressure, which represents the decreasing of shared electrons in the O-O bonds. Unusually,

nonetheless, the ELF value turns to an increase in the 2-3 GPa and 9-10 GPa pressure ranges. The increasing of ELF value at 2-3 GPa is consistent with the softening of elastic stiffness B_{11} and the softening of phonon frequencies of the acoustic modes at the Y point and the two-lowest frequencies of the optical modes at the Γ point at the same pressures as discussed before. In the same way, the increasing of ELF value at 9-10 GPa significantly corresponds to the softening of phonon frequencies of the two acoustic modes at the Y point. Unfortunately, the stiffening of elastic stiffness B_{22} at 9-10 GPa is inconsistent with the unusual increasing of the ELF value at 9-10 GPa. However, these provide that the significant increasing of ELF value at 3 and 10 GPa correspond to the softening of the phonon frequencies of the acoustic modes and/or the optical modes at 3 and 10 GPa. Furthermore, this also results in the stiffening of the O1-O1 and the O2-O2 bonds at 3 GPa. Even though the unusual change in the O-O bond length at 10 GPa was not found, but there was significant decreasing of the γ angle in the primitive *Amm*2 structure at 10 GPa [Figure 47(b)]. Moreover, the unusual change of ELF value in the $P6_3/mmc$ structure of Li_2O_2 was also predicted at 11 and 40 GPa [67], which related to a few of charge transfer between the O and Li atoms at those pressures. Probably, the charge transfer may also occur in the *Amm*2 structure of Na_2O_2, but the significant change of the partial DOSs of the Na and O was not found in this work.
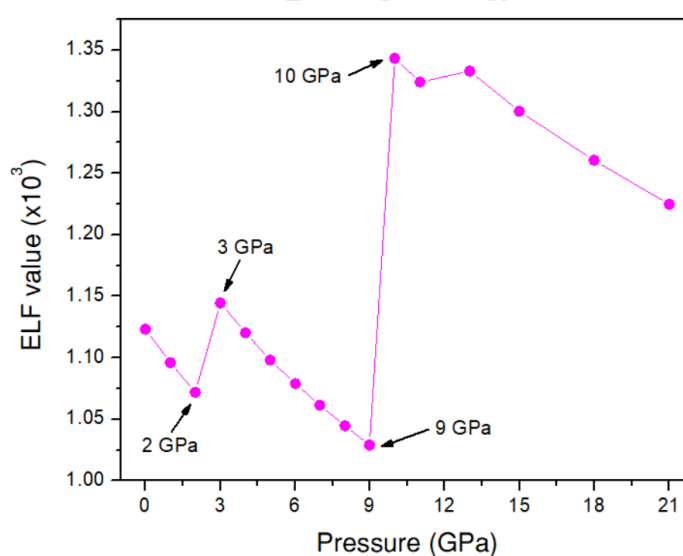
Figure 54: Electron localization function (ELF) value of the Amm2 structure in the 0-21 GPa pressure range [76].

To visualize the O-O bonds in the predicted phases of Na_2O_2 at high pressures, the two-dimensional ELF for the *Amm2* structure at 0 GPa projected onto the (110) plane, the $P2_1/c$ structure at 22 GPa projected onto the (200) plane, and the *Pbam* structure at 28 and 300 GPa projected onto the (001) plane were plotted, as shown in Figure 55. The results exhibited the shared electrons in the O-O bonds and the p-orbital shape of the O-O, which implies that the O-O single bonds in these structures are maintained up to 300 GPa.
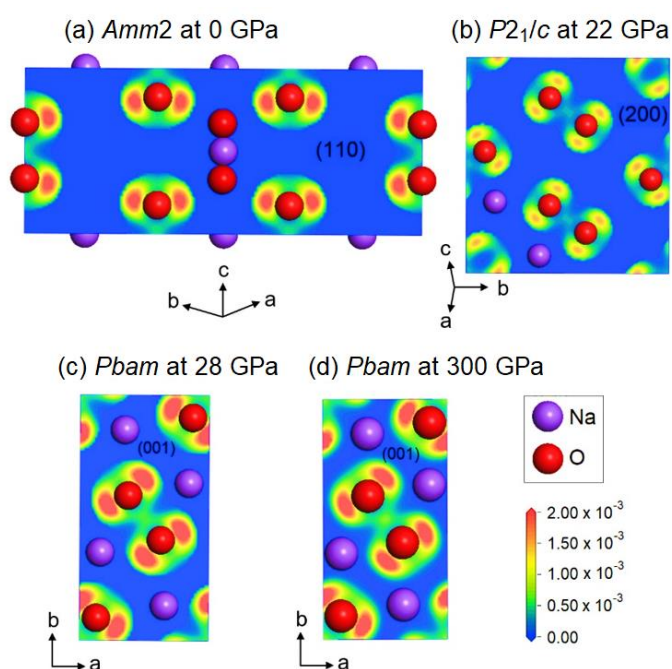
Figure 55: Two-dimensional ELF value of the predicted structures of Na_2O_2 at different pressures for: (a) the Amm2 structure at 0 GPa projected onto the (110) plane, (b) the $P2_1/c$ structure at 22 GPa projected onto the (200) plane, and (c and d) the Pbam structure at 28 and 300 GPa projected onto the (001) plane [76].

4.3 The Gibbs free energy changes of the CO_2 capture reactions by Li_2O_2 and Na_2O_2

To investigate the pressure effect on the CO_2 capture reactions by Li_2O_2 and Na_2O_2, the phonon dispersion and phonon density of states (PDOS) for the Li_2O_2, Li_2CO_3, CO_2, and O_2 at 8, 16, and 25 GPa and for the Na_2O_2, Na_2CO_3, CO_2, and O_2 at 8, 15, and 30 GPa were calculated using the supercell and finite displacement methods [49]. Their phonon dispersion curves and PDOSs are shown in appendix A. The Gibbs free energies

of them were calculated using Eq. (2.58) within the quasi-harmonic approximation, and then the Gibbs free energy changes of the reactions (ΔG) were obtained from using Eq. (2.64) and Eq. (2.65) for the CO_2 capture reactions by Li_2O_2 and Na_2O_2. The findings showed that the Gibbs free energies of the products [Li_2CO_3 + (1/2)O_2] and the reactants [Li_2O_2 + CO_2] significantly increase with increasing pressure, but they slightly decrease with the elevated temperature at 250-350 K (Figure 56). Importantly, the products at 8, 26, and 25 GPa are lower in Gibbs free energy than the reactants, which imply that the states of the products are more stable than the reactants. In other words, the CO_2 capture reaction by Li_2O_2 can spontaneously occur in the forward direction at the conditions of pressure (8, 16, 25 GPa) and temperature (250-350 K). However, the reaction rate is unknown but usually depends on the activation energy of reaction, which is not determined in this work.
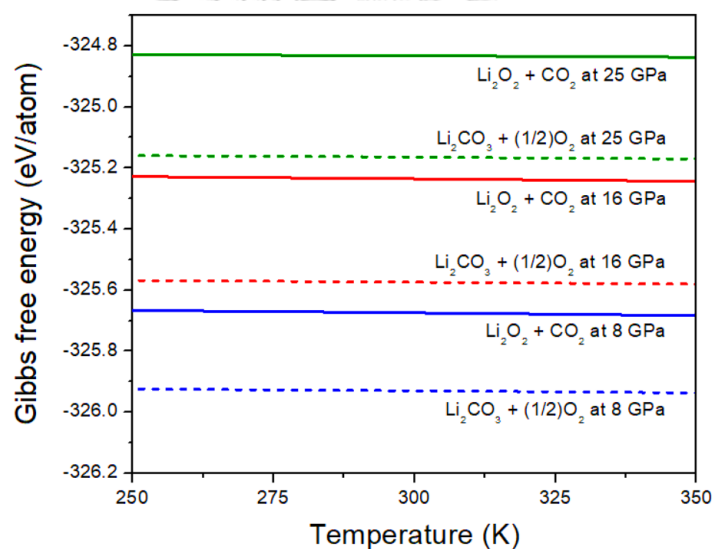
Figure 56: Plot of the Gibbs free energies for the reactants and products of the CO_2 capture reaction by Li_2O_2.

Moreover, plots of ΔG *versus* temperature revealed that with elevated temperature, the |ΔG| decreases at 8 and 16 GPa but increases at 25 GPa (Figure 57). However, |ΔG| at 16 GPa is larger than that of 25 and 8 GPa, respectively. This implies that the reaction at 16 GPa releases more energy than the reactions at 8 and 25 GPa.

As for the CO_2 capture reaction by Na_2O_2 at 8, 15, and 30 GPa, the findings exhibited that the Gibbs free energies of the products [Na_2CO_3 + (1/2)O_2] and the reactants

[Na$_2$O$_2$+CO$_2$] significantly also increase with increasing pressure but slightly decrease with elevated temperature at 250-350 K (Figure 58).

Figure 57: The Gibbs free energy changes of the CO$_2$ capture reaction by Li$_2$O$_2$ at 8, 16, and 25 GPa versus temperature at 250-350 K.

Moreover, the Gibbs free energies of the products at 8, 15, and 30 GPa are lower than that of the reactants, which suggests that the states of the products are more stable than the reactants. That is, the CO$_2$ capture reaction by Na$_2$O$_2$ can spontaneously occur in the forward direction at the conditions of pressure (8, 15, 30 GPa) and temperature (250-350 K). Nonetheless, the activation energy of the reaction that assigns the reaction rate is also unknown.

Besides, plots of ΔG *versus* temperature in Figure 59 showed that with increasing temperature, |ΔG| increases at 8 GPa but decreases at 15 GPa and holds at 30 GPa. Nevertheless, |ΔG| at 15 GPa is larger than that of 30 and 8 GPa, respectively. This also implies that the reaction at 16 GPa releases more energy than the reactions at 8 and 25 GPa.
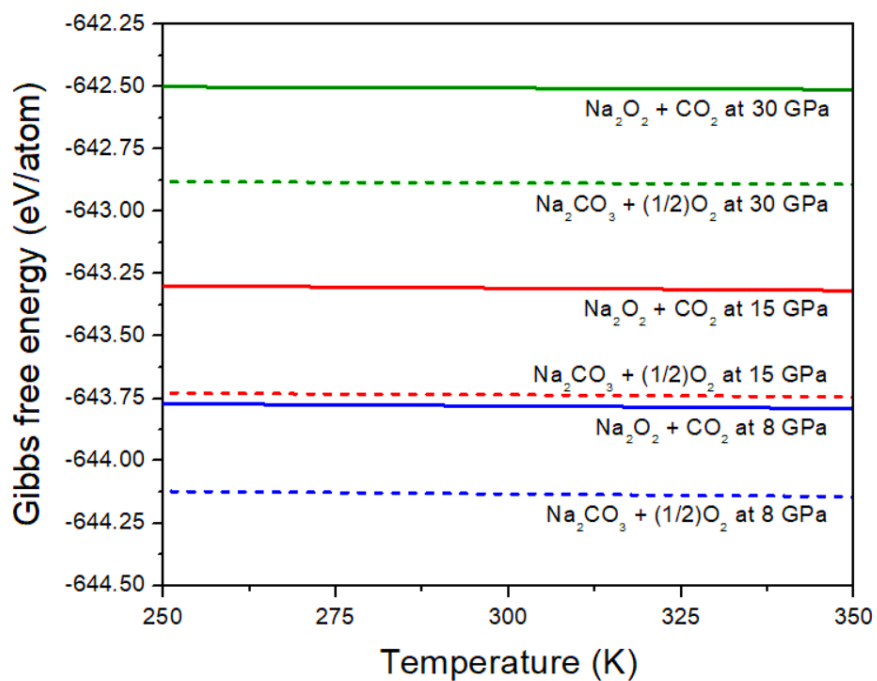
Figure 58: Plot of the Gibbs free energy of reactants and products of the CO_2 capture reaction by Na_2O_2.

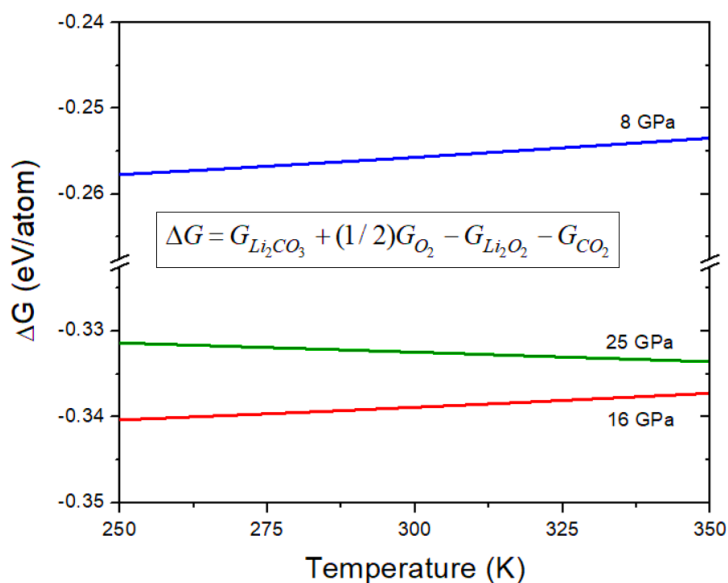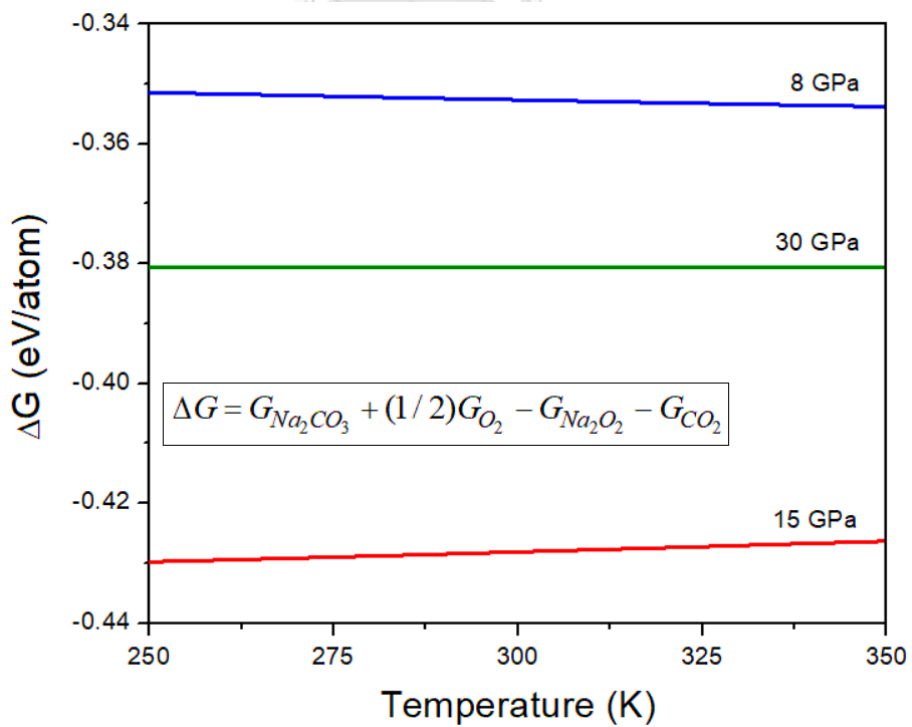$$\Delta G = G_{Na_2CO_3} + (1/2)G_{O_2} - G_{Na_2O_2} - G_{CO_2}$$

Figure 59: The Gibbs free energy change of the CO2 capture reaction by Na_2O_2 at 8, 15, and 30 GPa versus temperature at 250-350 K.

4.4 The Raman spectra of Na$_2$O$_2$ at high pressures: evidence for structural phase transitions

To identify the high-pressure structural phase transition in Na$_2$O$_2$, the Raman spectra of Na$_2$O$_2$ were measured at high pressures up to 25 GPa using the Raman spectroscopy, as discussed before.

At ambient conditions, the Raman spectrum of Na$_2$O$_2$ showed the Raman frequencies for the ambient phase of Na$_2$O$_2$ or the hexagonal *P-62m* structure. They consist of the frequencies of the lattice modes: 185 (ω_1), 192 (ω_2), 225 (ω_3), and 286 (ω_4) cm^{-1} and two frequencies of the O-O stretching modes: 737 (ω_5) and 792 (ω_6) cm^{-1}. These frequencies are in excellent agreement with the previous measurement proposed by Eysel *et al*. [88]. They reported the frequencies at 57, 79, 100, 121, 184, 193, 225, 286, 736, and 791 cm^{-1}. However, the frequencies at 57, 79, 100, and 121 cm^{-1} were not observed in the present work because their intensities were very weak. The intensity of two O-O stretching frequencies dominate in the spectrum, as shown in Figure 60, which result in the O-O stretching vibrations (out-of-plane) of the O1-O1 at 792 cm^{-1} and the O2-O2 at 737 cm^{-1}. The O1-O1 has only one bond per cell, but the O2-O2 have two bonds per cell. This suggests that the intensity peak at 737 cm^{-1} is about twice the intensity peak 792 cm^{-1}. Thus, these represent characteristics of the ambient phase of Na$_2$O$_2$.
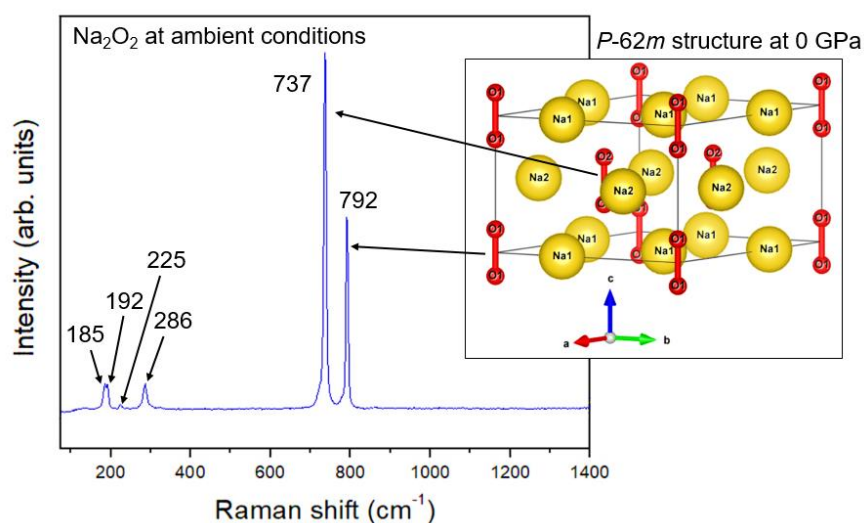

Figure 60: The Raman spectrum of Na$_2$O$_2$ measured at ambient conditions corresponding to the hexagonal P-62m structure.

By considering the Raman spectrum at 0.4 GPa, there were two unknown peaks at ~107 and 3,623 cm^{-1}, as shown in Figure 61 and Figure 62. However, by comparing with the Raman spectra of NaOH under high pressure proposed by Krobok *et al.* [89], the peaks were identified to be NaOH contamination. This contamination was obtained from the reaction between Na_2O_2 and H_2O, generating NaOH and H_2O_2. When H_2O_2 was degraded by light or heat, it produces H_2O and O_2 which were observed in a bottle containing Na_2O_2 powder in silicone oil. However, the Raman frequencies of H_2O and O_2 were not found in the Raman spectra of Na_2O_2. Therefore, it is likely to have only small contamination of NaOH in the sample chamber of the DAC.

With increasing pressure, Figure 61 showed that these frequencies (ω_1 - ω_6) increase along trend lines, suggesting the decreasing of the bond lengths. Interestingly, at 8.6 GPa, three new Raman peaks appear at ~820 (ω_7), ~847 (ω_8), and ~1,018 (ω_9) cm^{-1}. Furthermore, the frequencies of ω_7 and ω_8 increase with elevated pressure, yet the frequency of ω_9 decreases. Usually, the blueshift and redshift in Raman spectra represent the decreasing and increasing of chemical bond lengths of molecules. Thus, the bonds corresponding to the frequencies of ω_7 and ω_8 become stiffen with elevated pressure, but that of ω_9 becomes soften resulting in the bond dissociation.

As for the intensity peaks, overall, they have increasing trends with elevated pressure. However, the intensity of ω_9 decreases at 21.5 GPa, and it disappears at 24.8 GPa. Likewise, the intensities of ω_1 - ω_6 gradually decrease with elevated pressure and fade out beyond 15.8 GPa. With decreasing pressure, the Raman peaks of ω_1 - ω_9 appear at 9.1 GPa same at 8.6 GPa, but the Raman peaks of ω_7 - ω_9 disappear at 0.04 GPa. This implies that the ambient phase and the unknown phase at 8.6-21.5 GPa are reversible with decreasing pressure.

In addition, by comparing between the measured and calculated Raman spectra at 24.8 and 30 GPa, as shown in Figure 63, it revealed that their Raman intensities of the internal modes are consistent, but the frequencies and the intensities of the lattice modes are different because of the difference in temperature and the limitation of the *ab-initio* lattice dynamics calculations.
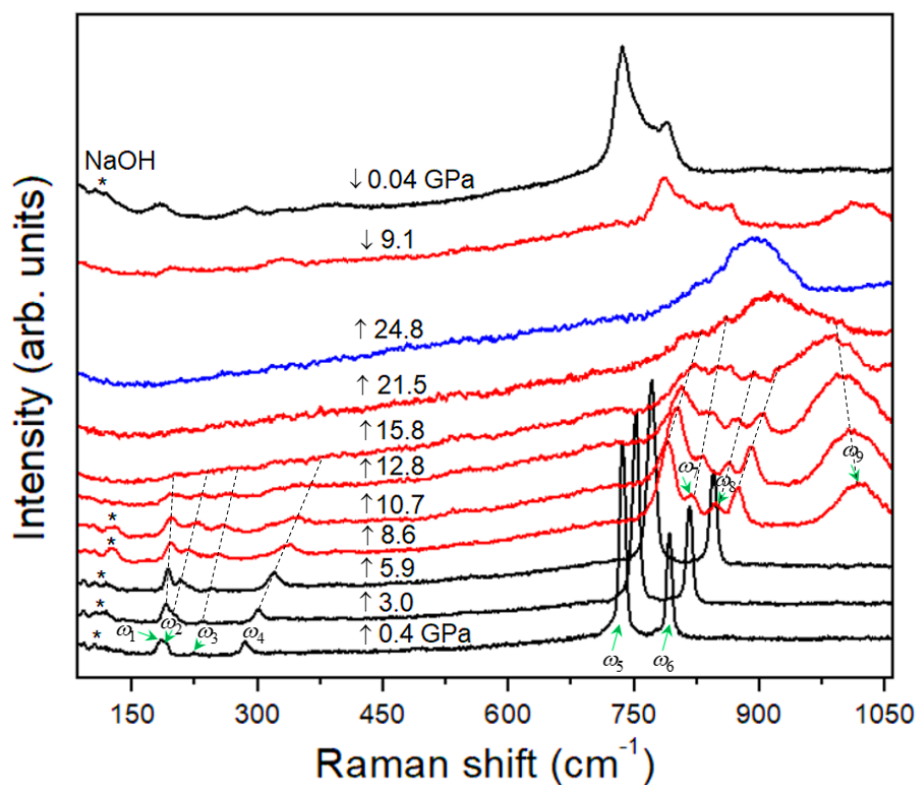
Figure 61: The Raman spectra of Na₂O₂ at different pressures. Raman peak positions are labelled by ω_1 to ω_9. The symbols, (↑) and (↓) represent increasing and decreasing pressures, respectively.
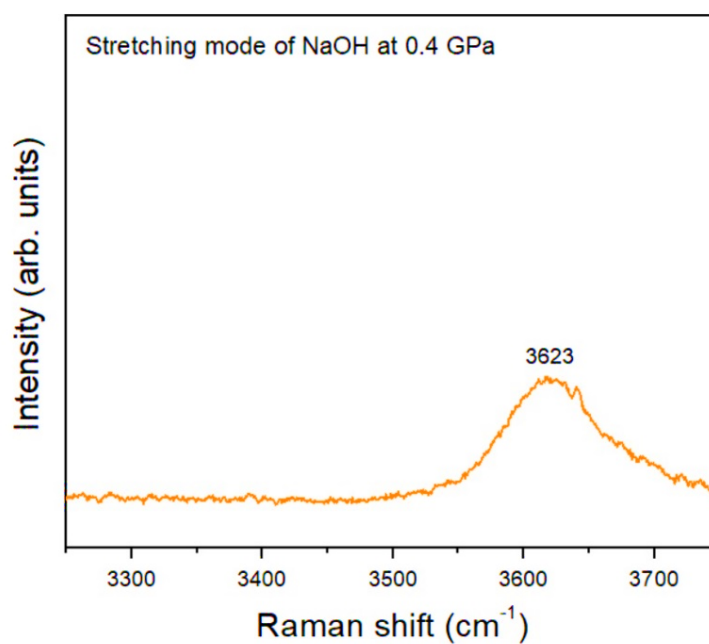

Figure 62: The Raman spectrum of the O-H stretching mode in NaOH at 0.4 GPa.

These suggest that the first structural phase transition in Na_2O_2 may occur at 8.6 GPa because the new Raman peaks appear, indicating the new chemical bonding or structural change. Similarly, the second structural phase transition may occur at 24.8 GPa, since the Raman peaks of ω_5, ω_6, and ω_9 are terminated. However, the structural phase transition has been predicted at 22 and 28 GPa by Jimlim *et al.* [76] and by Deng *et al*. [16]. That is, the hexagonal *P-62m* structure transforms to the orthorhombic *Pbam* structure. Therefore, it is possible to note that the structural phase transition in Na_2O_2 occurs at around 24.8 GPa, and the intermediate phase occurs in the 8.6-24.8 GPa pressure range. However, these require the XRD measurements for identifying those crystal structures.

The other point of view, using the structural data proposed by Struzhkin et al. [90] to calculate the Raman active modes of NaH_3 at 10 GPa, the results showed that there is the Raman active mode at around ~1,000 cm^{-1}, which is close to the Raman frequency of ω_9. Thus, the Raman frequency of ω_9 may represent a novel compound of Na_2O_2 (e.g., $Na_2H_xO_2$). However, this requires further investigations for verification.
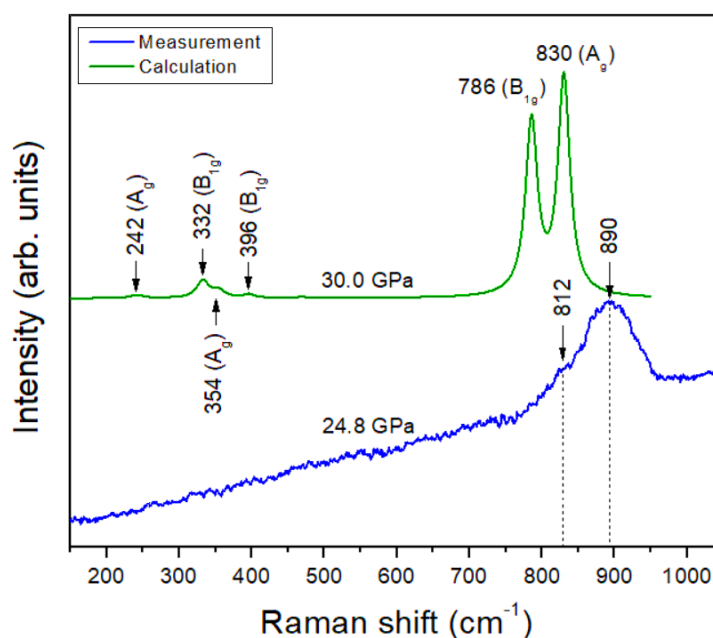

Figure 63: Comparison of the measured and the calculated Raman spectra of Na_2O_2 at 24.8 and 30.0 GPa.

Chapter 5

Conclusions

In summary, the structural phase transition and the electronic properties of Li_2O_2 at pressures up to 500 GPa were investigated using first-principles calculations. Two new structural phase transitions of Li_2O_2 were predicted at pressures around 75 and 136 GPa. That is, the hexagonal $P6_3/mmc$ structure was transformed to the monoclinic $P2_1$ structure at ~75 GPa, and the $P2_1$ structure was transformed to the monoclinic $P2_1/c$ structure at ~136 GPa. It was suggested that the driving force for the phase transformations is also assigned by the alignment of the Li atoms in their structures. The new phases were dynamically stable, and the presence of the O-O bonds in Li_2O_2 at high pressures up to 500 GPa were verified by the ELF values. Furthermore, the pressure evolution of the O-O bond length, the O-O stretching frequency, band gap, and charge transfer in Li_2O_2 were also calculated. It was predicted that the O-O bond length decreases with elevated pressure, while the O-O stretching frequency and the band gap increase. Remarkably, the band gap of the $P6_3/mmc$ structure was significantly decreased by pressure at 11 and 40 GPa, whereas the O-O bond length was increased. Moreover, the ELF value immediately was also increased at 8-11 GPa and 39-40 GPa. This implied that pressure induces increasing of the electron localization, resulting in the softening of the O-O bonds and the decreasing of the band gaps in the 10-11 and 39-40 GPa pressure ranges. Furthermore, the ELF plots revealed that electrons are highly localized in the O-O bonds, which confirm the presence of the O-O bonds under pressure up to 500 GPa. In addition, the charges transfer between the O and Li in the $P6_3/mmc$ structure were also analyzed using the PDOSs of the O and Li. Since the increasing and decreasing of the DOSs in the valence bands of Li and O at the same energy level in the 8-11 GPa and 39-40 GPa pressure ranges were consistent, this suggested the electrons transfer between the states of Li and O. Furthermore, the DOS of O for some energies of the conduction band (σ_p^*) increases at 8-11 and 39-40 GPa. This implied that the σ_p^* antibonding state of the O-O bonds is strengthened, resulting in the softening of the O-O bonds at 11 and 40 GPa. In addition, the study revealed that the structural distortions in Li_2O_2 arise from the

atomic displacements, which is a mechanism for maintaining the O-O bonds under high pressure up to 500 GPa.

The structural phase stability of Na_2O_2 under high pressure and temperature were investigated using first-principles calculations and the QHA to predict the phase stabilities of Na_2O_2 at high pressure up to 300 GPa and temperatures up to 600 K. The AIRSS searches were employed to search the lowest enthalpy structure at 0 K, and the dynamical and thermodynamic stabilities of the predicted structures were identified using the phonon dispersion and Gibbs free energy calculations, respectively. It was predicted that the *Amm*2 (distorted *P-62m*) structure is dynamically and thermodynamically stable in the 0-22 GPa pressure range at low temperature. Nevertheless, the *P-62m* structure becomes more thermodynamically stable than the *Amm*2 structure at elevated temperature. Moreover, it was analyzed that Tallman's structure is likely to favor at a higher temperature more than Föppl's structure. Furthermore, the *P2₁/c* structure was predicted that it is dynamically and thermodynamically stable in the 22-28 GPa pressure range at extremely low temperatures. However, the *Pbam* structure becomes a more favored structure than the *P2₁/c* structure at elevated temperatures. The AIRSS searches also discovered the candidates of high-temperature phases, Na_2O_2-II and Na_2O_2-Q, that is the *I4/mmm* and the *Immm* structures, respectively. Remarkably, the elastic stiffness was predicted that the elastic stiffnesses of B_{11} at 3 GPa and B_{22}, B_{44}, and B_{23} at 9 GPa soften, and the universal elastic anisotropy index at 3 GPa decreases. At the Y point, three phonon acoustic modes soften at 3 GPa and two of them soften at 10 GPa. Likewise, at the Γ point, the two-lowest frequencies of the optical modes at 3 GPa also soften. This results in the phonon free energies decreasing and the ELF increasing at 3 and 10 GPa. Even though the O-O bond length abnormally decreases at 3 GPa, the abnormal change of the O-O bond length is not found at 10 GPa, whereas an obvious decrease of the cell angle (γ) in the primitive *Amm*2 structure also appears. These revealed the mechanism for controlling the stability of Na_2O_2 at high pressures. Furthermore, it was predicted that the PBE and HSE06 band gaps for the three predicted phases of Na_2O_2 increase with increasing pressure, while the change in the band gaps is normal. This suggested that the elastic stiffnesses softening and the phonon frequencies softening

in the *Amm*2 structure are not significant effect on the band gap. In addition, the ELF values revealed the presence of the O-O bonds in Na_2O_2 under high pressure up to 300 GPa.

Furthermore, the high-pressure Raman study on structural phase transition in Na_2O_2 provided the evidence and the discussion for the structural phase transitions in Na_2O_2 under high pressure up to 25 GPa. It was suggested that the structural phase transition in Na_2O_2 might initially occur at 8.6 GPa, since the new Raman peaks appear, resulting in the new chemical bonding or structural change. The other structural phase transition may occur at 24.8 GPa because the Raman peaks of ω_5, ω_6, and ω_9 are terminated. Nevertheless, these require the experimental technique (e.g. XRD) for identifying the crystal structures at those pressures.

In addition, the Gibbs free energy changes of the CO_2 capture reactions by Li_2O_2 and Na_2O_2 revealed that it is possible to spontaneously occur the forward reactions at high pressures because their products $[M_2CO_3 + (1/2)O_2]$ are lower in free energy than the reactants $[M_2O_2+CO_2]$, where M represents Li, Na.

Therefore, this work provided the predicted structural phase transition in Li_2O_2 and Na_2O_2 at high pressures, their related properties (e.g., elastic, vibrational, and electronic properties), and the possibility for occurring the CO_2 capture reactions by Li_2O_2 and Na_2O_2. These may be useful for further investigations and CO_2 capture applications.

Appendices

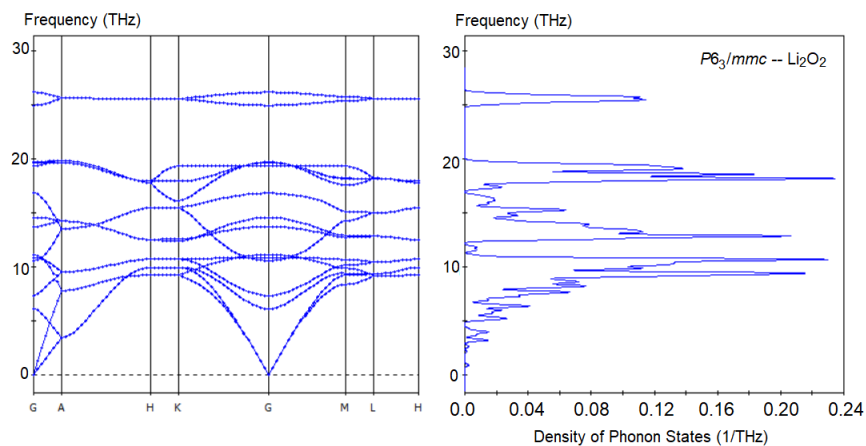## Appendix A: The phonon dispersion curves and phonon density of states

Figure 64: Phonon dispersion and PDOS for the $P6_3/mmc$–Li_2O_2 structure at 25 GPa.

Figure 65: Phonon dispersion and PDOS for the Pa-3–CO_2 structure at 8 GPa.

Figure 66: Phonon dispersion and PDOS for the $Cmca$–CO_2 structure at 16 GPa.

Figure 67: Phonon dispersion and PDOS of the I-42d–CO_2 structure at 30 GPa.
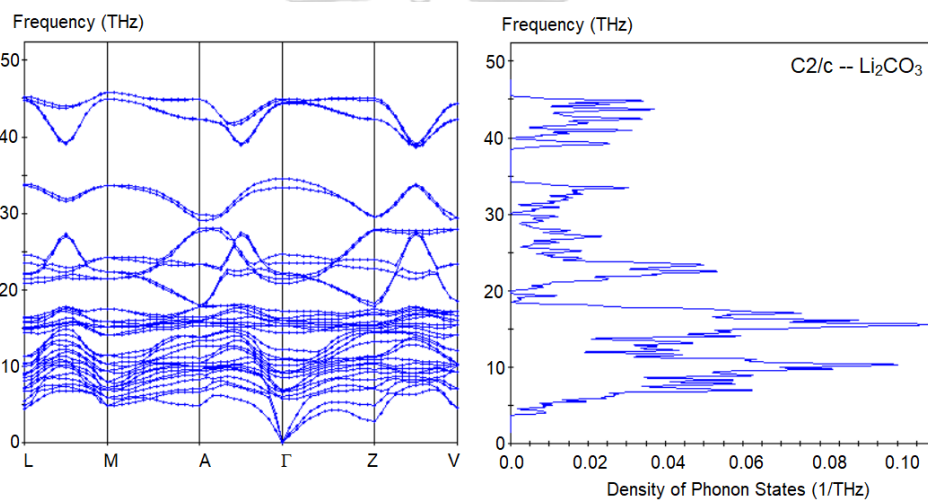
Figure 68: Phonon dispersion and PDOS for the C2/c–Li_2CO_3 structure at 8 GPa.
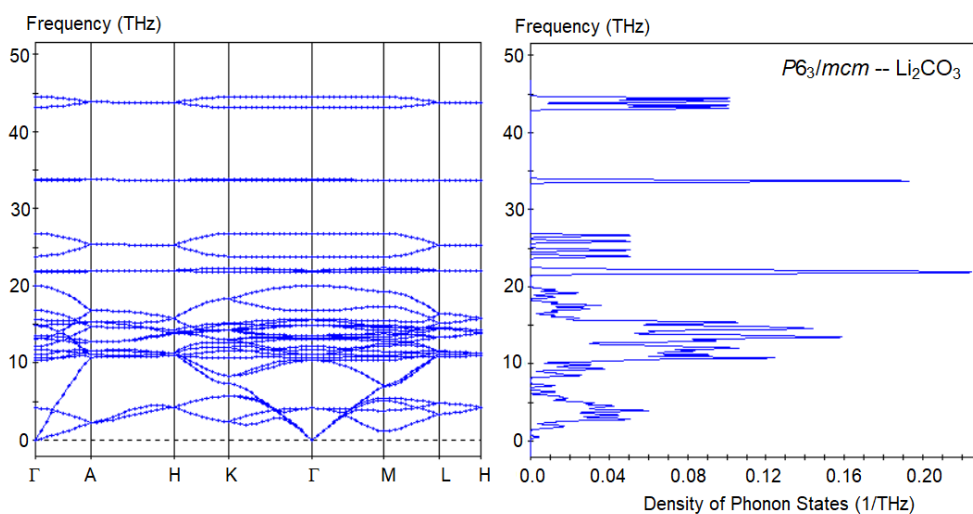
Figure 69: Phonon dispersion and PDOS for the $P6_3/mcm$–Li_2CO_3 structure at 25 GPa.
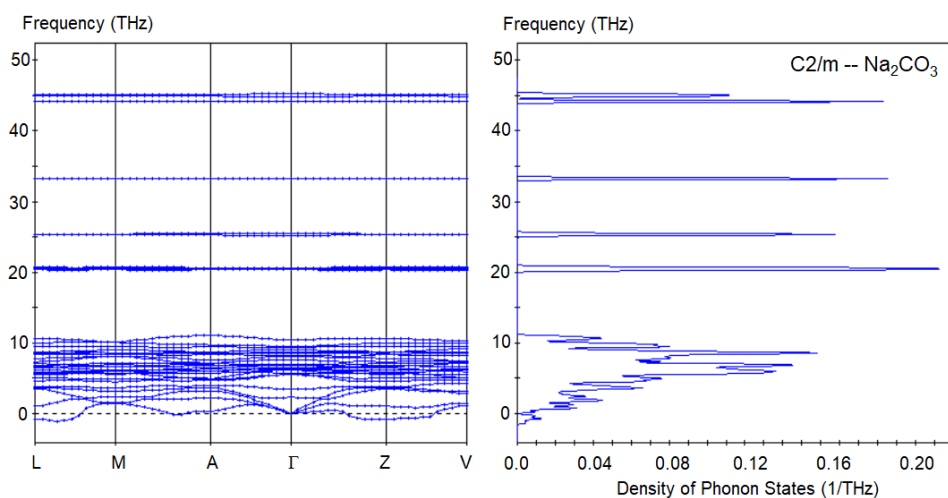
Figure 70: Phonon dispersion and PDOS for the C2/m–Na₂CO₃ structure at 8 GPa.
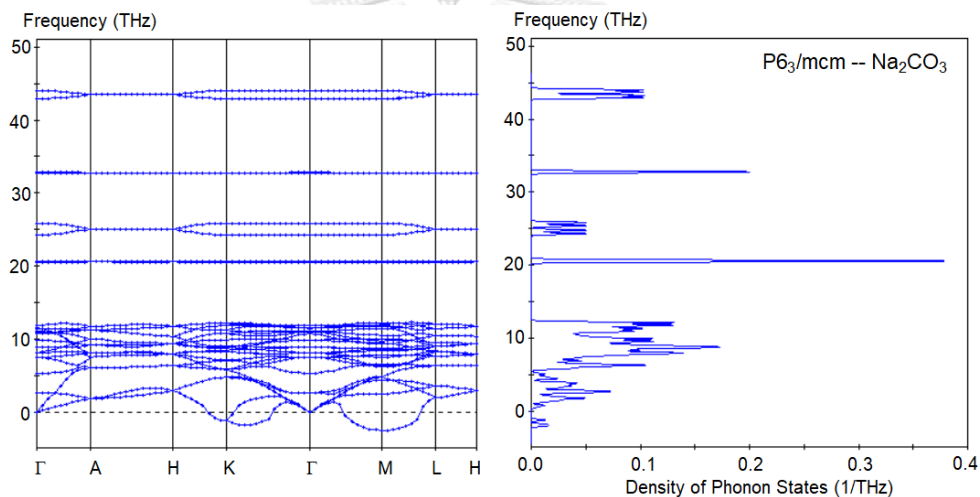
Figure 71: Phonon dispersion and PDOS for the P6₃/mcm–Na₂CO₃ structure at 15GPa.
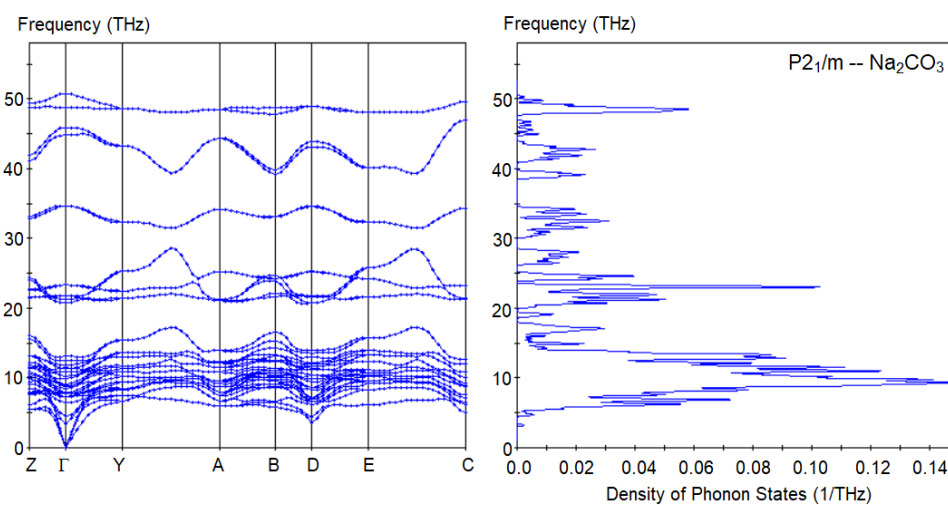
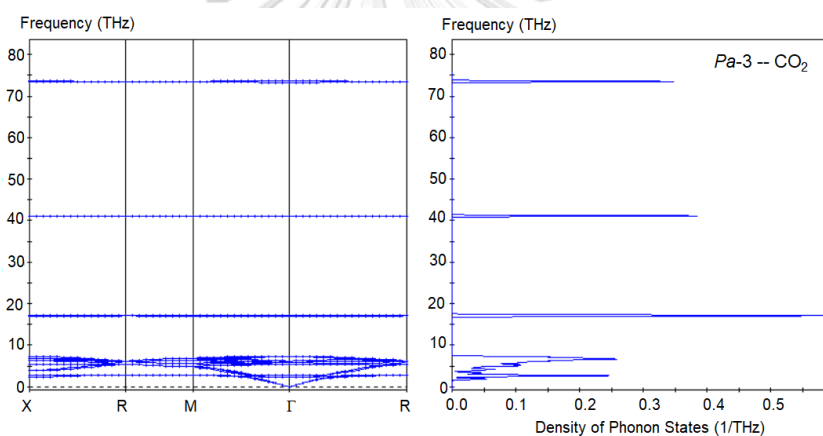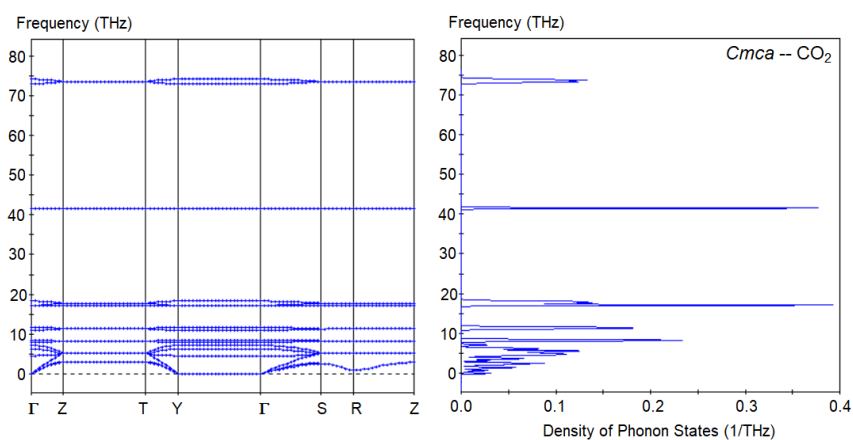*Figure 72: Phonon dispersion and PDOS for the P2₁/m–Na₂CO₃ structure at 30 GPa.*
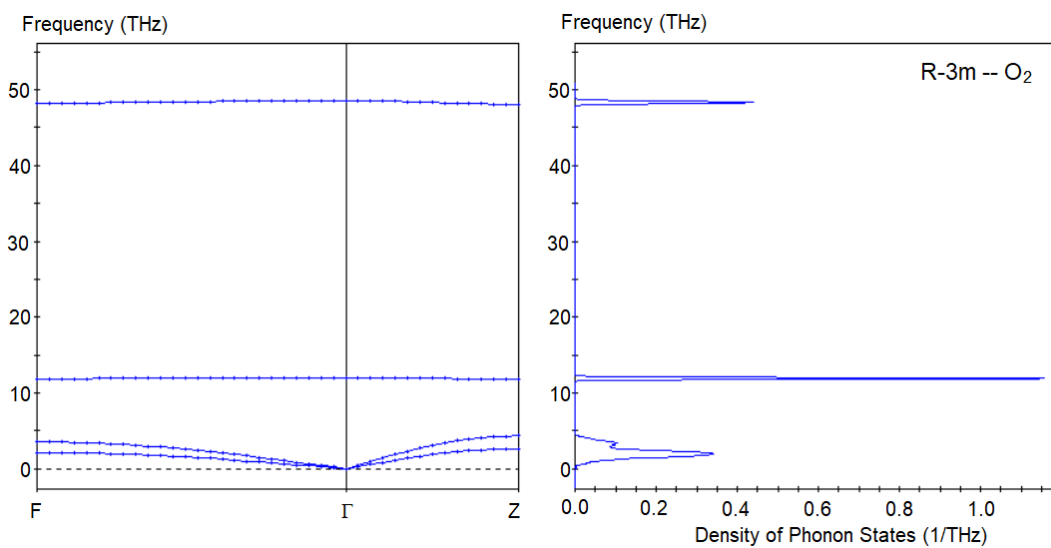
Figure 73: Phonon dispersion and PDOS for the R-3m–O$_2$ structure at 8 GPa.

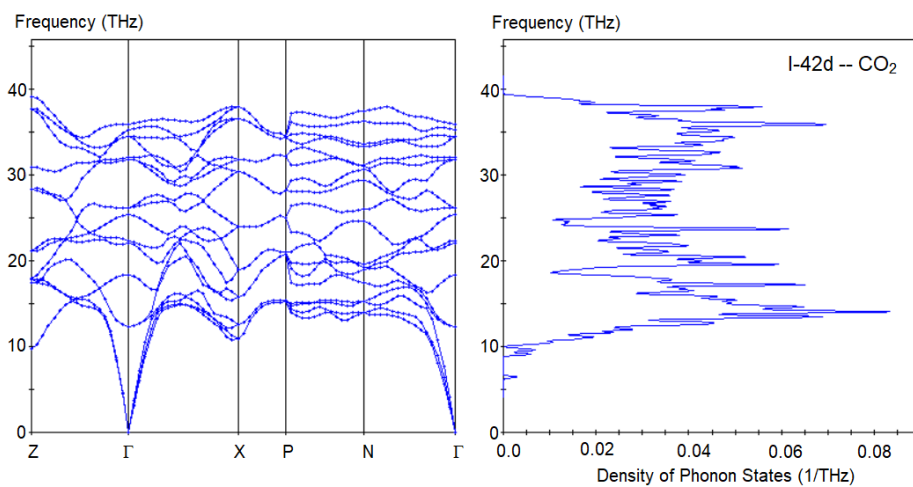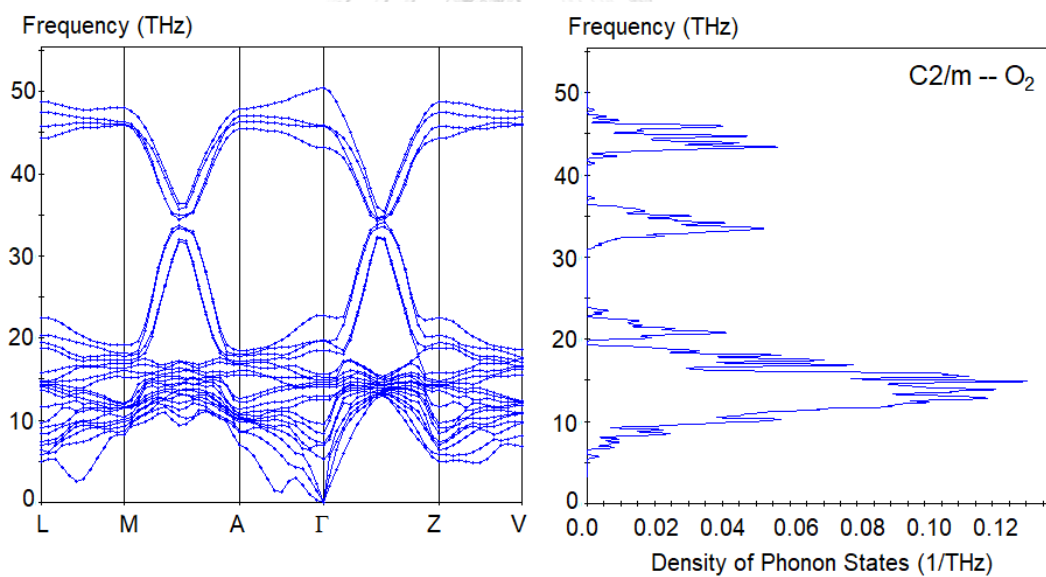*Figure 74: Phonon dispersion and PDOS for the C2/m–O$_2$ structure at 25 GPa.*

Appendix B: The Raman spectrum of Na$_2$O$_2$ at ambient conditions
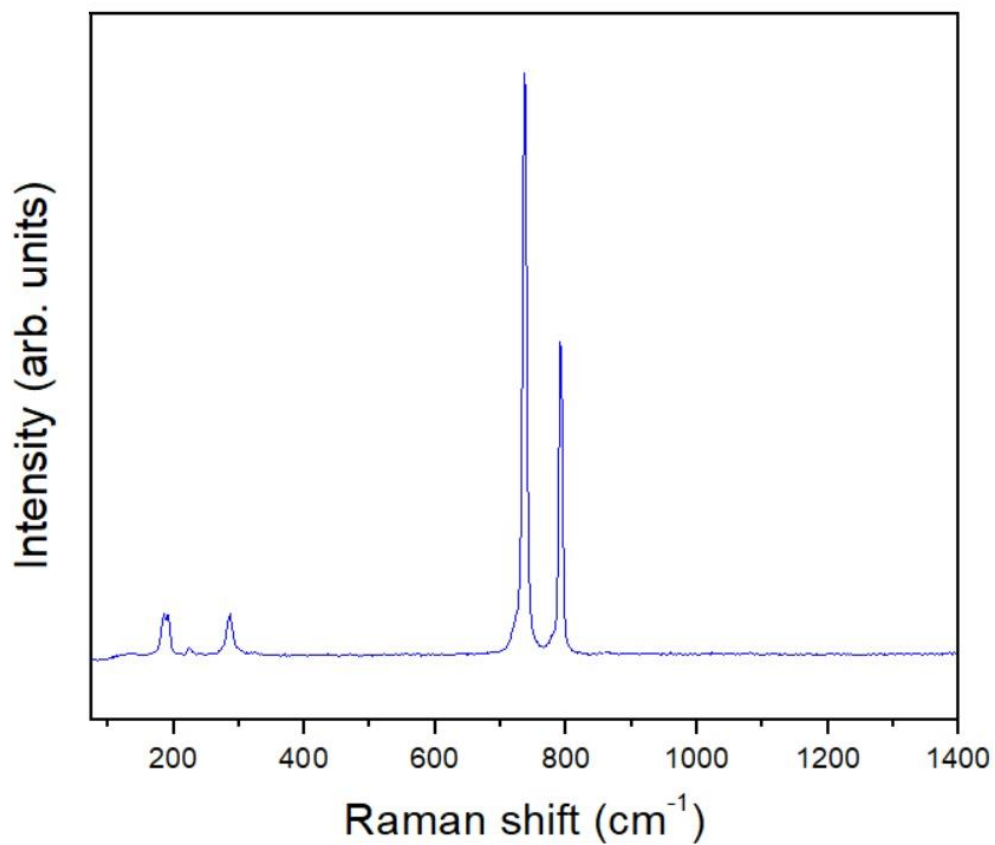
Figure 75: The Raman spectrum of granular Na$_2$O$_2$ at ambient conditions measured at Thailand's National Electronics and Computer Technology Center (NECTEC).

Appendix C: Pictures for the experimental apparatus
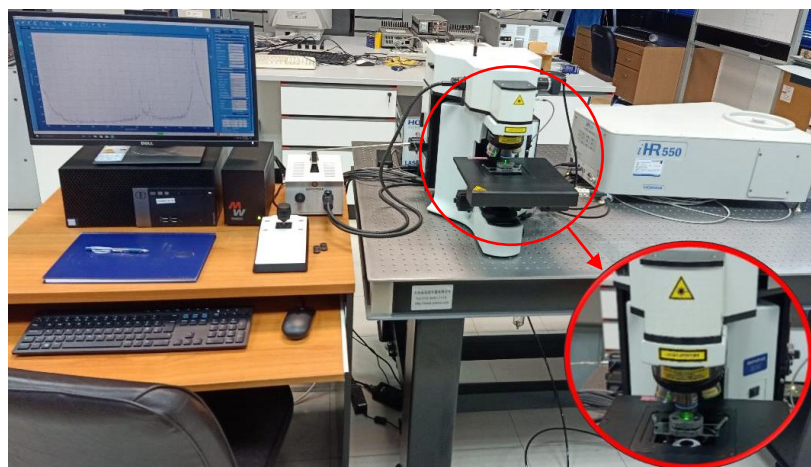
Figure 76: A Raman microscope for measuring the Raman spectra of samples.
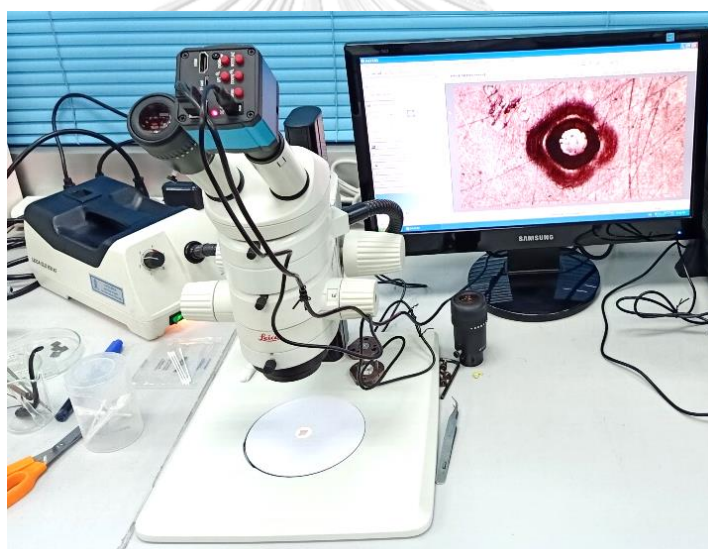
Figure 77: An optical microscope for sample loading.
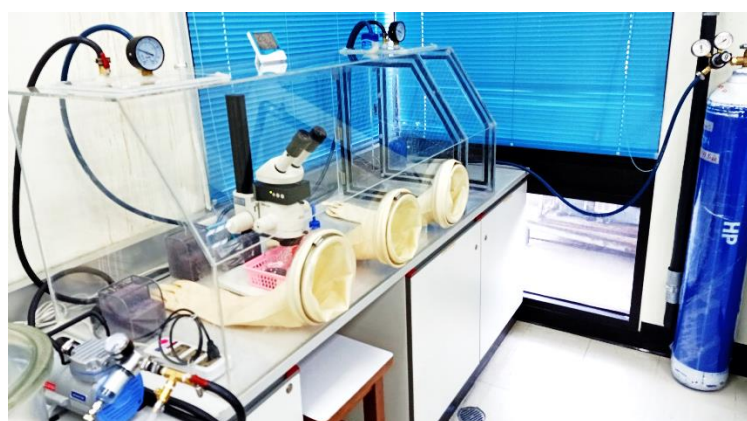
Figure 78: The invented glove box for isolating sample from ambient air.
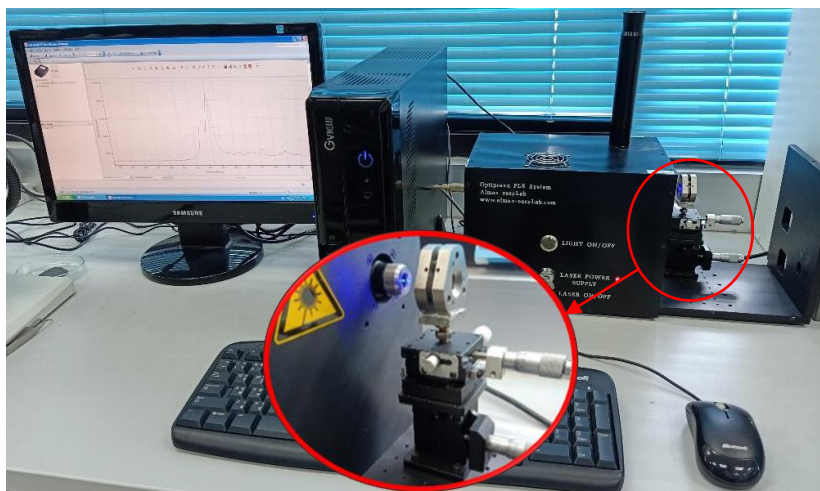
Figure 79: A Ruby fluorescence system for measuring the pressure in the DAC.
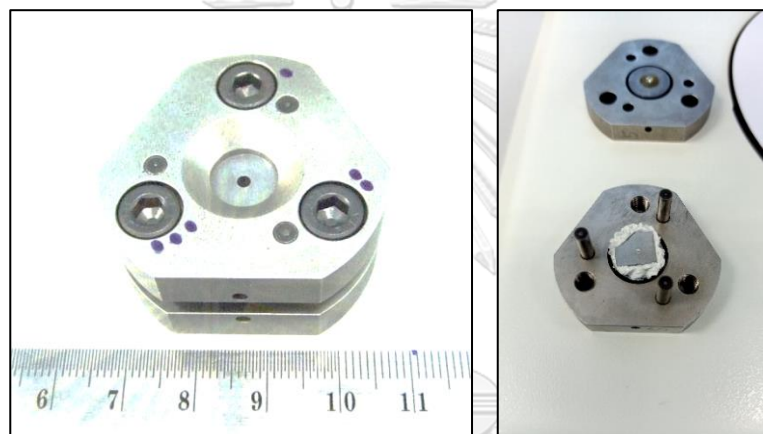
Figure 80: A Merrill-Bassett diamond anvil cell (DAC) for sample loading.

Figure 81: An electric discharge machine (EDM) for drilling the gasket.

REFERENCES

1. Ma, Y., et al., *Transparent dense sodium.* Nature, 2009. **458**(7235): p. 182-185.

2. Dias, R.P. and I.F. Silvera, *Observation of the Wigner-Huntington transition to metallic hydrogen.* Science, 2017. **355**(6326): p. 715-718.

3. Zhang, W., et al., *Unexpected Stable Stoichiometries of Sodium Chlorides.* Science, 2013. **342**(6165): p. 1502-1505.

4. Greenwood, N.N. and A. Earnshaw, *Chemistry of the Elements.* 2 ed. 1997, Oxford: Butterworth-Heinemann. 1600.

5. Wietelmann, U. and M. Steinbild, *Lithium and Lithium Compounds*, in *ULLMANN's Encyclopedia of Industrial Chemistry*. 2014. p. 1-38.

6. Markowitz, M.M., D.A. Boryta, and H. Stewart, *Concurrent carbon dioxide absorption and oxygen evolution by lithium peroxide.* Journal of Inorganic and Nuclear Chemistry, 1964. **26**(11): p. 2028-2033.

7. Selezneva, K.I., *Interaction of Lithium Peroxide with Water Vapor and Carbon Dioxide.* Russian Journal of Inorganic Chemistry, 1960. **5**(4-6): p. 820-823.

8. Föppl, H., *Die Kristallstrukturen der Alkaliperoxyde.* Zeitschrift für anorganische und allgemeine Chemie, 1957. **291**(1-4): p. 12-50.

9. Zhang, S., et al., *Pressure-Induced Stable Beryllium Peroxide.* Inorganic Chemistry, 2017. **56**(9): p. 5233-5238.

10. Song, K., et al., *High–Energy–Density Metal–Oxygen Batteries: Lithium–Oxygen Batteries vs Sodium–Oxygen Batteries.* Advanced Materials, 2017. **29**(48): p. 1606572.

11. Lau, K.C. and L.A. Curtiss, *Density Functional Investigation of the Thermodynamic Stability of Lithium Oxide Bulk Crystalline Structures as a Function of Oxygen Pressure.* The Journal of Physical Chemistry C, 2011. **115**(47): p. 23625-23633.

12. Yang, W., et al., *Oxygen-Rich Lithium Oxide Phases Formed at High Pressure for Potential Lithium–Air Battery Electrode.* Advanced Science, 2017. **4**(9): p. 1600453.

13. Fehér, F., I.V. Wilucki, and G. Dost, *Beiträge zur Kenntnis des Wasserstoffperoxyds und seiner Derivate, VII. Mitteil. : Über die Kristallstruktur des Lithiumperoxyds, Li$_2$O$_2$.* Chemische Berichte, 1953. **86**(11): p. 1429-1437.

14. Cota, L.G. and P. de la Mora, *On the structure of lithium peroxide, Li$_2$O$_2$.* Acta Crystallographica Section B, 2005. **61**(2): p. 133-136.

15. Chan, M.K.Y., et al., *Structure of Lithium Peroxide.* The Journal of Physical Chemistry Letters, 2011. **2**(19): p. 2483-2486.

16. Deng, N., et al., *Structural and electronic properties of alkali metal peroxides at high pressures.* RSC Advances, 2015. **5**(126): p. 104337-104342.

17. Dunuwille, M., M. Kim, and C.S. Yoo, *Pressure-induced phase and chemical transformations of lithium peroxide (Li$_2$O$_2$).* The Journal of Chemical Physics, 2016. **145**(132): p. 084701-084705.

18. Tallman, R.L., J.L. Margrave, and S.W. Bailey, *The Crystal Structure of Sodium Peroxide.* Journal of the American Chemical Society, 1957. **79**(11): p. 2979-2980.

19. Dunst, A., M. Sternad, and M. Wilkening, *Overall conductivity and NCL-type relaxation behavior in nanocrystalline sodium peroxide Na$_2$O$_2$–Consequences for Na-oxygen batteries.* Materials Science and Engineering B, 2016. **211**: p. 85-93.

20. Tallman, R.L. and J.L. Margrave, *Evidence for two new crystalline forms of sodium peroxide.* Journal of Inorganic and Nuclear Chemistry, 1961. **21**(1-2): p. 40-44.

21. Dunuwille, M., *Pressure-induced physical and chemical changes of non-conventional energetic materials: Nitrate, perchlorate and peroxide chemistries at high pressures and high temperatures*, in *Department of Chemistry*. 2015, Washington State University. p. 136.

22. Fiolhais, C., F. Nogueira, and M. Marques, *A Primer in Density Functional Theory*. 2003, Berlin Heidelberg: Springer-Verlag. 256.

23. Sholl, D.S. and J.A. Steckel, *Density Functional Theory: A Practical Introduction*. 2009, New Jersey: John Wiley & Sons. 238.

24. Hohenberg, P. and W. Kohn, *Inhomogeneous Electron Gas.* Physical Review, 1964. **136**(3B): p. B864-B871.

25. Kohn, W. and L.J. Sham, *Self-consistent equations including exchange and correlation effects.* Physical Review, 1965. **140**(4A): p. A1133.

26. Perdew, J.P. and Y. Wang, *Accurate and simple analytic representation of the electron-gas correlation energy.* Physical Review B, 1992. **45**(23): p. 13244.

27. Harrison, N.M., *An Introduction to Density Functional Theory*. 2003, IOS Press: Berlin. p. 187.

28. Perdew, J.P., K. Burke, and M. Ernzerhof, *Generalized Gradient Approximation Made Simple.* Physical Review Letters, 1996. **77**(18): p. 3865-3868.

29. Perdew, J.P., M. Ernzerhof, and K. Burke, *Rationale for mixing exact exchange with density functional approximations.* The Journal of Chemical Physics, 1996. **105**(22): p. 9982-9985.

30. Heyd, J., G.E. Scuseria, and M. Ernzerhof, *Hybrid functionals based on a screened Coulomb potential.* The Journal of Chemical Physics, 2003. **118**(18): p. 8207-8215.

31. Accelrys Software, I., *Materials Studio Release Notes, Release 6.1*. 2012, Accelrys Software Inc.: San Diego.

32. Vanderbilt, D., *Soft self-consistent pseudopotentials in a generalized eigenvalue formalism.* Physical Review B, 1990. **41**(11): p. 7892-7895.

33. Wikimedia Foundation, I. *Pseudopotential*. 2019 [cited 2019 December 8]; Available from: https://en.wikipedia.org/wiki/Pseudopotential.

34. Pfrommer, B.G., et al., *Relaxation of Crystals with the Quasi-Newton Method.* Journal of Computational Physics, 1997. **131**(1): p. 233-240.

35. Head, J.D. and M.C. Zerner, *A Broyden–Fletcher–Goldfarb–Shanno optimization procedure for molecular geometries.* Chemical physics letters, 1985. **122**(3): p. 264-270.

36. Refson, K. *Introduction to phonon and spectroscopy calculations in CASTEP*. 2012 [cited 2019 October 28]; Available from: http://ftp.nd.rl.ac.uk/KeithRefson/Accelrys/Intro_to_Phonons.pdf.

37. Mouhat, F. and F.-X. Coudert, *Necessary and Sufficient Elastic Stability Conditions in Various Crystal Systems.* Physical Review B, 2014. **90**(22): p. 224104.

38. Pickard, C.J. and R.J. Needs, *Ab initio random structure searching.* Journal of Physics: Condensed Matter, 2011. **23**(5): p. 053201.

39. Zurek, E. and W. Grochala, *Predicting crystal structures and properties of matter under extreme conditions via quantum mechanics: the pressure is on.* Physical Chemistry Chemical Physics, 2015. **17**(5): p. 2887-3922.

40. Glass, C.W., A.R. Oganov, and N. Hansen, *USPEX–Evolutionary crystal structure prediction.* Computer Physics Communications, 2006. **175**(11-12): p. 713-720.

41. Grima, J.N. *Properties of the Gibbs free energy*. 2007 [cited 2019 October 23]; Available from: http://staff.um.edu.mt/jgri1/teaching/che2372/notes/04/g_props/g_props.html.

42. Khan Academy, I. *Free energy*. 2015 [cited 2019 October 23]; Available from: https://www.khanacademy.org/science/biology/energy-and-enzymes/free-energy-tutorial/a/gibbs-free-energy.

43. Sirenko, A. *Raman Scattering*. 2007 [cited 2019 October 23]; Available from: https://web.njit.edu/~sirenko/Phys-774/Lecture11-2007.pdf.

44. Oganov, A.R. and C.W. Glass, *Crystal structure prediction using ab initio evolutionary techniques: Principles and applications.* The Journal of Chemical Physics, 2006. **124**(24): p. 244704.

45. Kresse, G. and J. Furthmüller, *Efficient iterative schemes for ab initio total-energy calculations using a plane-wave basis set.* Physical Review B, 1996. **54**(16): p. 11169-11186.

46. Kresse, G. and J. Furthmüller, *Efficiency of ab-initio total energy calculations for metals and semiconductors using a plane-wave basis set.* Computational Materials Science, 1996. **6**(1): p. 15-50.

47. Clark, S.J., et al., *First principles methods using CASTEP.* Zeitschrift für Kristallographie, 2005. **220**(5-6): p. 567-570.

48. Birch, F., *Finite Elastic Strain of Cubic Crystals.* Physical Review, 1947. **71**(11): p. 809-824.

49. Togo, A. and I. Tanaka, *First principles phonon calculations in materials science.* Scripta Materialia, 2015. **108**: p. 1-5.

50.   Momma, K. and F. Izumi, *VESTA 3 for three-dimensional visualization of crystal, volumetric and morphology data.* Journal of Applied Crystallography, 2011. **44**(6): p. 1272-1276.

51.   Savin, A., et al., *Electron Localization in Solid‐State Structures of the Elements: the Diamond Structure.* Angewandte Chemie International Edition in English, 1992. **31**(2): p. 187-188.

52.   Frank, W., C. Elsässer, and M. Fähnle, *Ab initio Force-Constant Method for Phonon Dispersions in Alkali Metals.* Physical Review Letters, 1995. **74**(10): p. 1791-1794.

53.   Ranganathan, S.I. and M. Ostoja-Starzewski, *Universal Elastic Anisotropy Index.* Physical Review Letters, 2008. **101**(5): p. 055504.

54.   Hill, R., *The Elastic Behaviour of a Crystalline Aggregate.* Proceedings of the Physical Society. Section A, 1952. **65**(5): p. 349-354.

55.   Idemoto, Y., et al., *Crystal structure of $(Li_xK_{1-x})_2CO_3$ (x = 0, 0.43, 0.5, 0.62, 1) by neutron powder diffraction analysis.* Journal of Physics and Chemistry of Solids, 1998. **59**(3): p. 363-376.

56.   Grzechnik, A., P. Bouvier, and L. Farina, *High-pressure structure of Li_2CO_3.* Journal of Solid State Chemistry, 2003. **173**(1): p. 13-19.

57.   Gavryushkin, P.N., et al., *High-Pressure Phase Diagrams of Na_2CO_3 and K_2CO_3.* Minerals, 2019. **9**(10): p. 599.

58.   Han, Y., et al., *Predicting the phase diagram of solid carbon dioxide at high pressure from first principles.* npj Quantum Materials, 2019. **4**(10): p. 1-7.

59.   Lu, C., M. Miao, and Y. Ma, *Structural Evolution of Carbon Dioxide under High Pressure.* Journal of the American Chemical Society, 2013. **135**(38): p. 14167-14171.

60.   Schiferl, D., D.T. Cromer, and R.L. Mills, *Structure of O_2 at 5.5 GPa and 299 K.* Acta Crystallographica Section B, 1981. **B37**: p. 1329-1332.

61.   Fujihisa, H., et al., *O_8 Cluster Structure of the Epsilon Phase of Solid Oxygen.* Physical Review Letters, 2006. **97**(8): p. 085503.

62.   Song, Y., *Novel Pressure-Induced Molecular Transformations Probed by In Situ Vibrational Spectroscopy*. 2015, IntechOpen Limited: Online. p. 163-187.

63.   Shen, Y., et al., *Characteristics of silicone fluid as a pressure transmitting medium in diamond anvil cells.* Review of Scientific Instruments, 2004. **75**(11): p. 4450-4454.

64.   Mao, H.K., J. Xu, and P.M. Bell, *Calibration of the ruby pressure gauge to 800 kbar under quasi‐hydrostatic conditions.* Journal of Geophysical Research, 1986. **91**(B5): p. 4673-4676.

65.   Eremets, M.I., *High pressure experimental method*. 1996, New York: Oxford University Press. 390.

66.   Goncharov, A.F., *Raman Spectroscopy at High Pressures.* International Journal of Spectroscopy, 2011. **2012**(617528): p. 1-16.

67.   Jimlim, P., et al., *Theoretical aspects in structural distortion and the electronic properties of lithium peroxide under high pressure.* Physical Chemistry Chemical Physics, 2018. **20**(14): p. 9488-9497.

68.   Wu, H., et al., *Ab initio calculations of structural, elastic and electronic properties of Li_2O_2.* Philosophical Magazine, 2007. **87**(23): p. 3373-3383.

69.   Flor, G.d.l., et al., *Comparison of structures applying the tools available at the Bilbao Crystallographic Server.* Journal of Applied Crystallography, 2016. **49**(2): p. 653-664.

70.   Lau, K.C., et al., *Theoretical Exploration of Various Lithium Peroxide Crystal Structures in a Li-Air Battery.* Energies, 2015. **8**(1): p. 529-548.

71.   Radin, M.D., F. Tian, and D.J. Siegel, *Electronic structure of Li_2O_2 {0001} surfaces.* Journal of Materials Science, 2012. **47**(21): p. 7564-7570.

72.   Garcia-Lastra, J.M., J.D. Bass, and K.S. Thygesen, *Communication: Strong excitonic and vibronic effects determine the optical properties of Li_2O_2.* The Journal of Chemical Physics, 2011. **135**(12): p. 121101.

73.   Kang, J., et al., *Implications of the formation of small polarons in Li_2O_2 for Li-air batteries.* Physical Review B, 2012. **85**(3): p. 035210.

74.   Segall, M.D., et al., *Population analysis in plane wave electronic structure calculations.* Molecular Physics, 1996. **89**(2): p. 571-577.

75.   Segall, M.D., et al., *Population analysis of plane-wave electronic structure calculations of bulk materials.* Physical Review B, 1996. **54**(23): p. 16317.

76.   Jimlim, P., et al., *Theoretical predictions for low-temperature phases, softening of phonons and elastic stiffnesses, and electronic properties of sodium peroxide under high pressure.* RSC Advances, 2019. **9**(53): p. 30964-30975.

77.   Wang, B., et al., *Electrolyte-controlled discharge product distribution of Na–O_2 batteries: a combined computational and experimental study.* Physical Chemistry Chemical Physics, 2017. **19**(4): p. 2940–2949.

78.   Jain, A., et al., *Commentary: The Materials Project: A materials genome approach to accelerating materials innovation.* APL Materials, 2013. **1**(1): p. 011002.

79.   Deng, N., et al., *Structural transitions and electronic properties of sodium superoxide at high pressures.* RSC Advances, 2016. **6**(72): p. 67910-67915.

80.   Wyckoff, R.W.G., *Hexagonal closest packed, hcp, structure.* Crystal Structures, 1963. **1**(1): p. 7-83.

81.   Barrett, C.S., L. Meyer, and J. Wasserman, *Antiferromagnetic and Crystal Structures of Alpha-Oxygen.* The Journal of Chemical Physics, 1967. **47**(2): p. 592-597.

82.   Lundegaard, L.F., et al., *Observation of an O_8 molecular lattice in the epsilon phase of solid oxygen.* Nature, 2006. **443**(7108): p. 201-204.

83.   Karki, B.B., G.J. Ackland, and J. Crain, *Elastic instabilities in crystals from ab initio stress - strain relations.* Journal of Physics: Condensed Matter, 1997. **9**(41): p. 8579-8589.

84.   de Jong, M., et al., *Charting the complete elastic properties of inorganic crystalline compounds.* Scientific Data, 2015. **2**(150009): p. 1-13.

85.   Csonka, G.I., et al., *Assessing the performance of recent density functionals for bulk solids.* Physical Review B, 2009. **79**(15): p. 155107.

86. Aleinikova, M.V., Y.N. Zhuravlev, and D.V. Korabelnikov, *Ab-initio investigation of the effect of pressure on the structure and electronic properties of alkali metal oxides and peroxides.* Russian Physics Journal, 2012. **55**(5): p. 495-500.

87. Yang, S. and D.J. Siegel, *Intrinsic Conductivity in Sodium–Air Battery Discharge Phases: Sodium Superoxide vs Sodium Peroxide.* Chemistry of Materials, 2015. **27**(11): p. 3852-3860.

88. Eysel, H.H. and S. Thym, *RAMAN Spectra of Peroxides.* Zeitschrift für anorganische und allgemeine Chemie, 1975. **411**(2): p. 97-102.

89. Krobok, M.P., P.G. Johannsen, and W.B. Holzapfel, *Raman and ITIR study of NaOH and NaOD under pressure.* Journal of Physics: Condensed Matter, 1992. **4**(41): p. 8141-8150.

90. Struzhkin, V.V., et al., *Synthesis of sodium polyhydrides at high pressures.* Nature Communications, 2016. **7**(12267): p. 1-8.
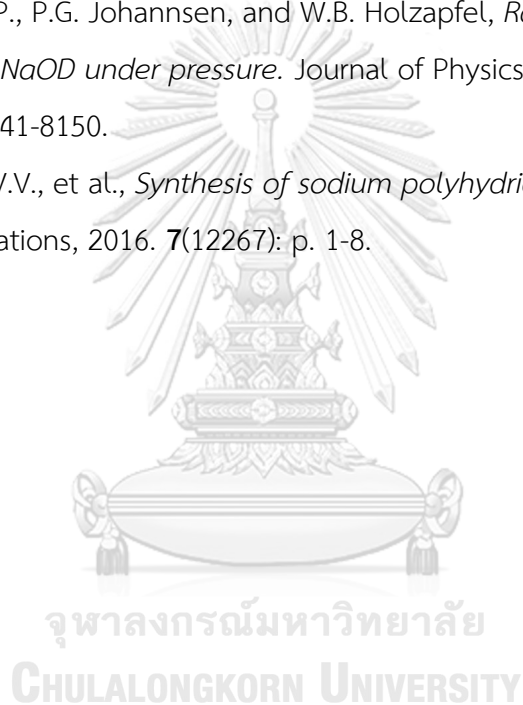
VITA

NAME	Pornmongkol Jimlim
DATE OF BIRTH	1 December 1977
PLACE OF BIRTH	Thayang hospital, Petchaburi
INSTITUTIONS ATTENDED	Mahidol Wittayanusorn School
	364 Moo 5 Salaya, Phutthamonthon, Nakhon Pathom 73170
HOME ADDRESS	13/1 Moo 4, Wangyen, Bangpae, Ratchaburi 70160.

PUBLICATION

1. Jimlim, P., Kotmool, K., Pinsook, U., Assabumrungrat, S., Ahuja, R. and Bovornratanaraks, T., Theoretical aspects in structural distortion and the electronic properties of lithium peroxide under high pressure. Physical Chemistry Chemical Physics, 2018. 20(14): p. 9488-9497.
Impact factor (2017): 3.906

2. Jimlim, P., Tsuppayakorn-aek, P., Pakornchote, T., Ektarawong, A., Pinsook, U., and Bovornratanaraks, T., Theoretical predictions for low-temperature phases, softening of phonons and elastic stiffnesses, and electronic properties of sodium peroxide under high pressure. RSC Advances, 2019. 9(53): p. 30964-30975.
Impact factor (2018): 3.049

3. Jimlim, P. and Bovornratanaraks, T., High-pressure apparatus for the CO_2 capture by powder sorbent at room temperature. Invention patent. submitted on Sep. 26, 2018, No. of the patent application: 1801005881.

AWARD RECEIVED　-